# Titanium Dioxide Nanoparticles for Photodynamic Therapy

A thesis submitted to the University of Manchester for the degree of

**Doctor of Philosophy**

in the Faculty of Medical and Human Sciences

**Christopher J. Cadman**

School of Pharmacy and Pharmaceutical Sciences

**2013**

# Contents

**Word count: 48,600**

# List of Figures

# List of Equations

## List of Schemes

## List of Tables

# Abstract

In the present thesis we propose the development of hybrid polymer titanium dioxide ($TiO_2$) nanoparticles for use in biomedical applications. $TiO_2$ exhibits high biocompatibility in the dark however, upon illumination in aqueous media with near UV light it produces an array of reactive oxygen species (ROS) which have the capability to induce death in neighbouring cells. The process of inducing cell death using a photosensitive material which produces ROS is known as photodynamic therapy (PDT) and is used to treat a wide range of maladies from psoriasis to cancer.

We have demonstrated the ability to produce anatase nanoparticles with high control over their resulting size through a novel water mediated sol-gel synthetic method in benzyl alcohol, using either $Ti(OnPr)_4$, $Ti(OnBu)_4$ or $Ti(O^iPr)_4$ as the metal precursor. Through dynamic light scattering (DLS) analysis we have shown that the mechanism of nanoparticle growth appears to proceed through the agglomeration of primary nanoparticles formed instantly upon adding the reagents together. After synthesis the nanoparticles could be easily redispersed in aqueous media at pH2 with any further agglomeration being controlled by the parent alkoxide.

After synthesis the nanoparticles were coated with PEG, conjugated to either a catechol or phosphate as ligand, in order to stabilise the nanoparticles at neutral pH. Uncoated nanoparticles exhibited good photoactive capability in the photooxidation of methylene blue. However, on coating with catechols the photoactivity of the nanoparticles was abolished. Coating with phosph(on)ates on the other hand preserved or even enhanced the photoactivity which makes this system promising for *in vivo* applications.

At the same time this thesis also reports preliminary investigations on the use of $TiO_2$ embedded into the walls of model drug loaded poly electrolyte multilayer microspheres for UV triggered delivery applications.

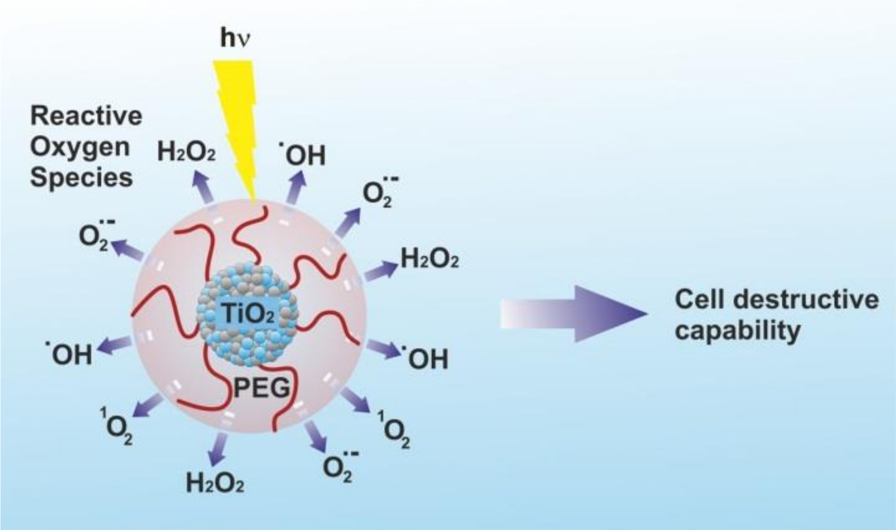

# Declaration and Copyright Statement

No portion of the work referred to in the thesis has been submitted in support of an application for another degree or qualification of this or any other university or other institute of learning.

Note on copyright and the ownership of intellectual property right:

i. The author of this thesis (including any appendices and/or schedules to this thesis) owns certain copyright or related rights in it (the "Copyright") and he has given The University of Manchester certain rights to use such Copyright, including for administrative purposes.

ii. Copies of this thesis, either in full or in extracts and whether in hard or electronic copy, may be made only in accordance with the Copyright, Designs and Patents Act 1988 (as amended) and regulations issued under it or, where appropriate, in accordance with licensing agreements which the University has from time to time. This page must form part of any such copies made.

iii. The ownership of certain Copyright, patents, designs, trademarks and other intellectual property (the "Intellectual Property") and any reproductions of copyright works in the thesis, for example graphs and tables ("Reproductions"), which may be described in this thesis, may not be owned by the author and may be owned by third parties. Such Intellectual Property and Reproductions cannot and must not be made available for use without the prior written permission of the owner(s) of the relevant Intellectual Property and/or Reproductions.

iv. Further information on the conditions under which disclosure, publication and commercialisation of this thesis, the Copyright and any Intellectual Property and/or Reproductions described in it may take place is available in the University IP Policy (see http://documents.manchester.ac.uk/DocuInfo.aspx?DocID=487), in any relevant Thesis restriction declarations deposited in the University Library, The University Library's regulations (see http://www.manchester.ac.uk/library/aboutus/regulations) and in The University's policy on Presentation of Theses.

# Dedication

## *For Mum*

*May the road rise to meet you.*
*May the wind be always at your back.*
*May the sun shine warm upon your face,*
*and rains fall soft upon your fields.*
*And until we meet again,*
*may God hold you in the palm of His hand.*

***An old Irish blessing – Anon.***

# Acknowledgements

I would like to express my gratitude towards Prof. Nicola Tirelli and Dr. Francesco Cellesi for offering me this PhD position and for the unending help and guidance they have offered throughout my time here. I would also like to thank Prof. Tirelli for not only imparting his wisdom on all things Chemistry, but also for sharing his insights into other aspects of the world from Latin to The Hitchhiker's Guide to the Galaxy. Also I would like to acknowledge the EPSRC for the award of a studentship to fund this PhD.

I would like to thank to everyone in the Laboratory of Polymers and Biomaterials. Specifically I would like to thank Dr. Sihem Ouasti for all her help with the biology data gathered for this thesis, and a thank you is in order for Mr. Roberto Donno for his help with AFM matters. To the rest of the group thank you for giving me the opportunity to hone my skills and become the greatest table football player in the world, and to team Cannondale/Raleigh (Dr. Nicholas Rattray, Mr. Aled Williams, Mr. Damien Jeanmaire and Dr. Enrique Lallana-Ozores) thank you for sharing in my delusion that I have any chance of becoming a professional cyclist.

Last but not least I would like to thank my family and Gigi (or to give her her full title Dr. Ghislaine Robert-Nicoud) for their love and support during my entire PhD, especially to Gigi for putting up with me these last few months.

# List of Abbreviations

| | |
|---|---|
| Å | Angstrom ($10^{-10}$ meter) |
| AFM | Atomic Force Microscopy |
| ATR-IR | Attenuated Total Reflection Infrared |
| BCA | Bicinchoninic Acid Assay |
| BQ | *p*-BenzoQuinone |
| CA | California |
| CA | 3,4-dihydrohydroxyCinnamic Acid |
| CCD | Charge Coupled Device |
| DA | DopAmine |
| DCM | DiChloroMethane |
| DEXS | Dextran |
| $D_f$ | Fractal Dimension |
| DLS | Dynamic Light Scattering |
| DMEM | Dulbecco's modified eagle's medium |
| DMF | DiMethyl Formamide |
| DMSO | DiMethyl SulfOxide |
| DMT | Derjaguin-Muller-Toporov |
| EDTA | EthyleneDiamineTetraacetic Acid |
| ee | Encapsulation Efficiency |
| EELS | Electron Energy Loss Spectroscopy |
| eV | Electron Volt |
| FBS | Fetal Bovine Serum |
| FDA | Food and Drug Administration |
| FWHM | Full Width Half Maximum |
| GPC | Gel Permeation Chromatography |
| HPLC | High Performance Liquid Chromatography |
| Hz | Hertz |
| IR | Infrared |
| JKR | Johson-Kendall-Roberts |
| kHz | KiloHertz ($10^3$ Hertz) |
| kPa | KiloPascal ($10^3$ Pascal) |

| | |
|---|---|
| kV | Kilovolts ($10^3$ volts) |
| LbL | Layer by Layer |
| m | Meter |
| MB | Methylene Blue |
| MeOH | Methanol |
| MFP-3D | Molecular Force Probe 3D AFM |
| mL | Millilitre ($10^{-3}$ liter) |
| mm | Millimeter ($10^{-3}$ meter) |
| mmol | Millmole ($10^{-3}$ mole) |
| mPEG-DA | Methoxy-PEG-DopAmine |
| mPEG-PEA | Methoxy-PEG-*O*-PhosphorylEthanolAmine |
| MPS | Mononuclear Phagocyte System |
| MRI | Magnetic Resonance Imaging |
| mW | milli Watt ($10^{-3}$ Watt) |
| MWCO | Molecular Weight Cut-Off |
| N | Newton |
| NIR | Near InfraRed |
| nm | Nanometer ($10^{-9}$ meter) |
| NMR | Nuclear Magnetic Resonance |
| PAH | Poly(allylamine) |
| PBS | Phosphate Buffered Saline |
| PDI | Poly Dispersity Index |
| PDMS | Poly(dimethyl siloxane) |
| PDT | PhotoDynamic Therapy |
| PEA | *O*-PhosphorylEthanolAmine |
| PEG | Poly(ethylene glycol) |
| PEM | PolyElectrolyte Multilayer |
| PFA | ParaFormAldehyde |
| PGMMA | Poly(glycerolmonomethacrylate) |
| pN | PicoNewton ($10^{-12}$N) |
| PNP | 4-Nitrophenyl chloroformate |

| | |
|---|---|
| PPA | 3-PhosphonoPropionic Acid |
| PPS | Poly(propylene sulfide) |
| PPS-PGMMA | Poly(propylene sulfide)-poly(glycerol monomethacrylate |
| PS | PhotoSensitizer |
| PSS | Poly(sodium 4-styrene sulfonate) |
| PVDF | PolyVinyliDene Fluoride |
| $R_g$ | Radius of Gyration |
| ROS | Reactive Oxygen Species |
| $R_p$ | Radius of primary particles |
| rpm | Revolutions Per Minute |
| SilGMMA | Poly(glycerolmonomethacrylate)-poly(dimethylsiloxane)-poly(glycerolmonomethacrylate) |
| SLS | Static Light Scattering |
| TBA | TetraButylAmmonium hydroxide |
| TEA | TriEthylAmine |
| TEM | Transmission Electron Microscopy |
| $T_g$ | Glass transition temperature |
| TGA | Thermogravimetric analysis |
| $TiO_2$ | Titanium Dioxide |
| UK | United Kingdom |
| UV | Ultraviolet |
| XRD | X-Ray Diffraction |
| µm | Micrometer ($10^{-6}$ meter) |

# 1 Introduction

The search for new ways to combat disease and illness is an ever growing field. The onset of drug resistance is a major obstacle for the treatment of many diseases and has led to the development of stronger drugs to combat them[1]. However, because the majority of drugs are non-specific, they are highly toxic to non-target cells and often cause side effects which can be more debilitating than the disease at that set moment[2]. Now it seems that new avenues need to be explored and the use of traditional drugs alone to combat disease needs to be reviewed.

Through the need for the development of new therapies a lot of interest is now being directed towards utilising nanoparticles, particles billionths of meters in diameter, for biomedical applications[3-5]. The reasons as to why nanoparticles are an interesting prospect will be described in more detail later in Chapter 1.1.3. However briefly, nanoparticles are on a scale that can interact on a subcellular level[6] and their composition can be finely tuned to give them unique properties[7]. Also nanoparticles may be used as an active agent themselves or as scaffolds for delivering active agents more efficiently to target areas.

This thesis is based on the development of titanium dioxide ($TiO_2$) nanoparticles for biomedical applications. $TiO_2$ is an attractive material to use medically due to the photoactivity it exhibits under illumination in the near ultraviolet (UV) range[8]. Utilised in the body the photoactivity of $TiO_2$ could allow the development of unique applications as $TiO_2$ is highly biocompatible in the dark[9], however upon illumination in bodily tissue it releases highly reactive oxygen species (ROS) which are cytotoxic and can induce apoptosis in neighbouring cells[10]. There is a lot of interest in using nanoparticles which are activated by external stimuli as without a stimulus they are harmless and do not cause any adverse side effects. Also there is the possibility to give a stealth character to the nanoparticles giving them a polymer coating, see Chapter 1.4.2. Therefore the nanoparticles can remain undetected in the body and are only activated when they have reached the desired target site, rather like a Trojan horse on a cellular level[11-13].

## 1.1 Nanoparticles

Michael Faraday is heralded as the father of nanoscience due to his work, reported in 1847, in the change of the optical properties of nanoparticles compared to their bulk metal counterparts[14]. Richard Feynman is also credited as being one of the first people who really began to contemplate the concepts of nanotechnology. Feynman's talk at the California Institute of Technology in 1959 titled "There's Plenty of Room at the Bottom" described a variety of ways in which it would be possible to manipulate a material on an atomic scale; nowadays a number of these methods have been realised such as in atomic force microscopy (AFM) and scanning tunnelling microscopy (STM)[15]. However, it was the development of scanning tunnelling microscopy by Binnig and Rohrer in 1982[16] and the discovery of buckminsterfullerene by Smalley in 1985[17] that dawned the new era of nanotechnology which opened up a whole new world for materials science.

### *1.1.1 What is nano?*

Nanomaterials have the potential to be used in almost all aspects of modern technology such as cosmetics[18], food packaging[19], energy production[20], medicine[21], the list is practically endless. As the use of nanomaterials in everyday applications is relatively new, there is growing apprehension as to the potential consequences of their widespread use[22, 23]. The main uncertainty rests with how the nanomaterials will affect the environment and human health, as it will be practically impossible to control their distribution once they are being used widely[24]. Due to these uncertainties the definition of what constitutes as a nano material is a widely debated topic[25, 26].

Up until October 2011 there wasn't actually any official definition for what can be called "nano". However, with the ever increasing use of nanomaterials the European Commission published a report with the first official definition of what they are, the definition is as follows; "*A natural, incidental or manufactured material containing particles, in an unbound state or as an aggregate or as an agglomerate and where,* *for 50 % or more of the particles in the number size distribution, one or more external dimensions is in the size range 1 nm - 100 nm*"[27].

As a derivation of the above statement, 2-dimensional materials, such as graphene and silicene flakes with only one dimension below 100 nm may be classed as nanosheets[28]. Structures with 2 dimensions less than 100 nm in diameter are typically called nanofibres[29]. Finally when all 3 dimensions of the material are in the sub 100 nm range then the material is defined as a nanoparticle[30].

There is still a lot of debate as to whether this definition is the be all and end all for what constitutes as a nanomaterial. For example, it can be argued that the 100 nm limit should be lowered to at least 60 nm as this is the range where quantum confinement (see Chapter 1.1.2) typically begins to control and provide the unique properties of a nanomaterial[31]. Also the term "50% or more" seems a little ambiguous as surely a nanomaterial should be completely 100% in the nanoregime? It seems likely that as a result of the enormous diversity of nanomaterials available there will never be a single definition that fits all, and perhaps the nanomaterial class may have to be subdivided in the future. However on saying that, is there any real reason as to why they have to be classified and have unique regulations in the first place? There are already a multitude of regulations in place for the development of new products, especially for biomedical use, therefore why would the process of regulation be any different for nanomaterials?

### *1.1.2 The unique properties of nanoparticles*

Materials with all three dimensions in the micron or higher range typically exhibit the same fundamental characteristics regardless of their size. However if you reduce the size of the material into the nano regime then some of their characteristics begin to change as discussed below[32]. There are a number of reasons for these changes.

In the macro range the atoms constituting the surface of the material are so few, relative to the bulk of the material, that they practically have no influence on the properties of the material. However, as the size of the material reduces to the nano regime, the overall surface area to volume ratio is drastically increased[31]. This increase in surface area is particularly important for the reactivity of the material. For example the reactivity of catalysts can be increased by many magnitudes by simply using their nanoparticle counterparts and increasing the surface area to volume ratio[33]. The potential of nanoparticles as high performance catalysts was fully realised by Haruta *et. al.* who were the first to use transition metal doped gold nanoparticles to catalyse the oxidation of carbon monoxide at a temperature of -70 °C[34].

As you move into the nano scale the properties of many nanoparticles are governed by the afore mentioned quantum confinement effect[35]. Quantum confinement is particularly important when using nano sized (5-10 nm) semi-conductors also known as quantum dots. Quantum dots are typically constituted of calcogenides (containing sulphur, selenium etc.) of metals such as cadmium and zinc producing, for example, CdSe[36] or ZnS[37]. A semi-conductor typically has a small band gap, this is the energy required to promote an electron from the ground state (valence band) to a singlet excited state (conduction band) Figure 1.1.2-1. By exciting the semi-conductor a free electron and a positive hole (h+) are created, which are often referred to as an exciton pair. The distance between the electron hole pair is called the exciton Bohr radius. The excited electron can then either relax back down to the ground state from the singlet state emitting a photon of light, this is known as fluorescence. Otherwise, the electron can undergo intersystem crossing to a much longer lived triplet state, and from here relax back to the ground state emitting a photon of light with lower energy than that of fluorescence, this is known as phosphorescence[38]. When the size of the semi-conductor crystal decreases below the exciton Bohr radius the band gap of the crystal increases. Therefore, as the band gap changes this gives rise to the potential to finely tune the optical and electronic properties of a quantum dot simply by controlling its size.

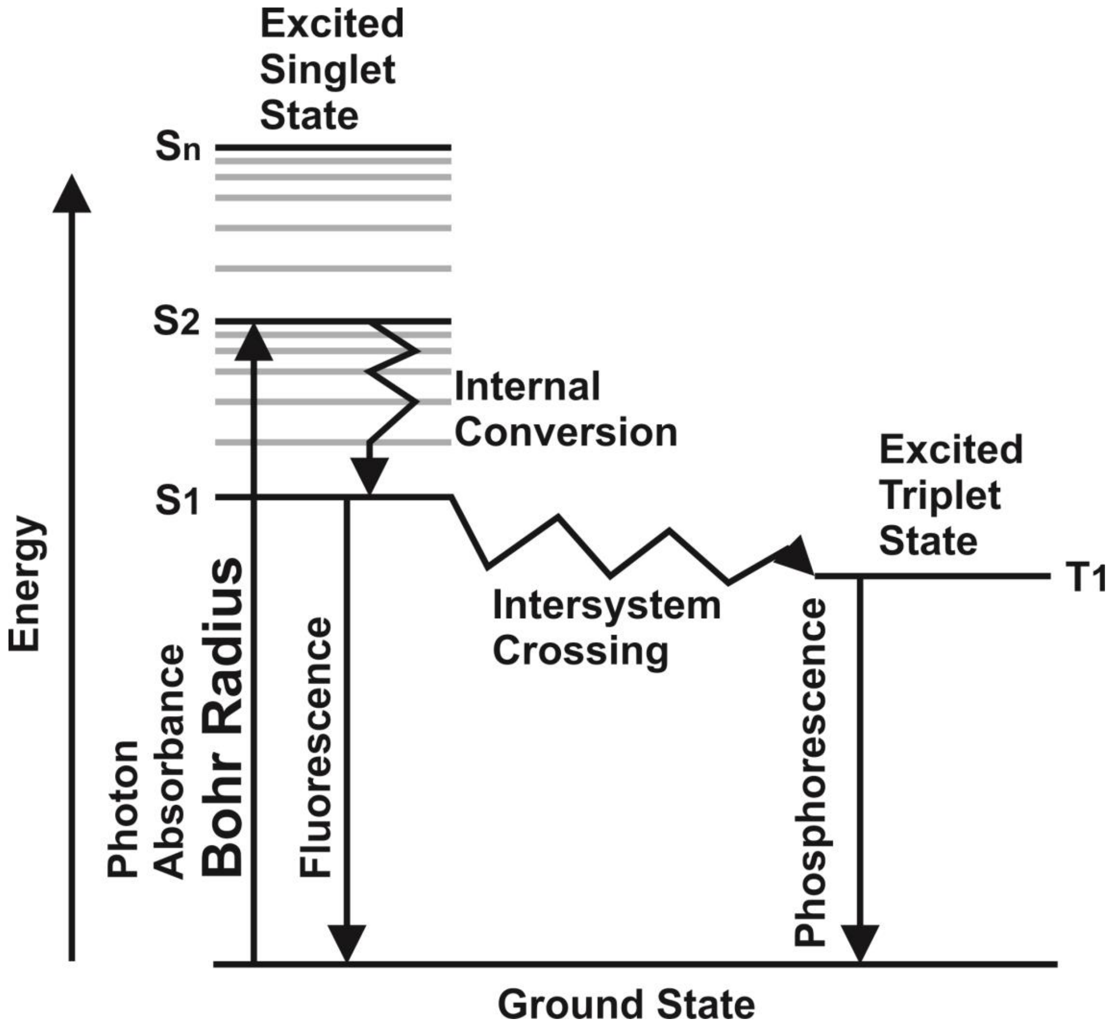

**Figure 1.1.2-1** A Jablonski diagram showing the changes in energy an electron undergoes after absorbing a photon of light promoting it from the electronic ground state to a higher energy singlet state.

Figure 1.1.2-2 illustrates the dependence of luminescence on the size of CdSE/ZnS quantum dots, where the smaller, 2.3 nm, nanocrystals emit blue light but as size increases to 5.5 nm the emission shifts towards the red region (reproduced from reference 37)[39].

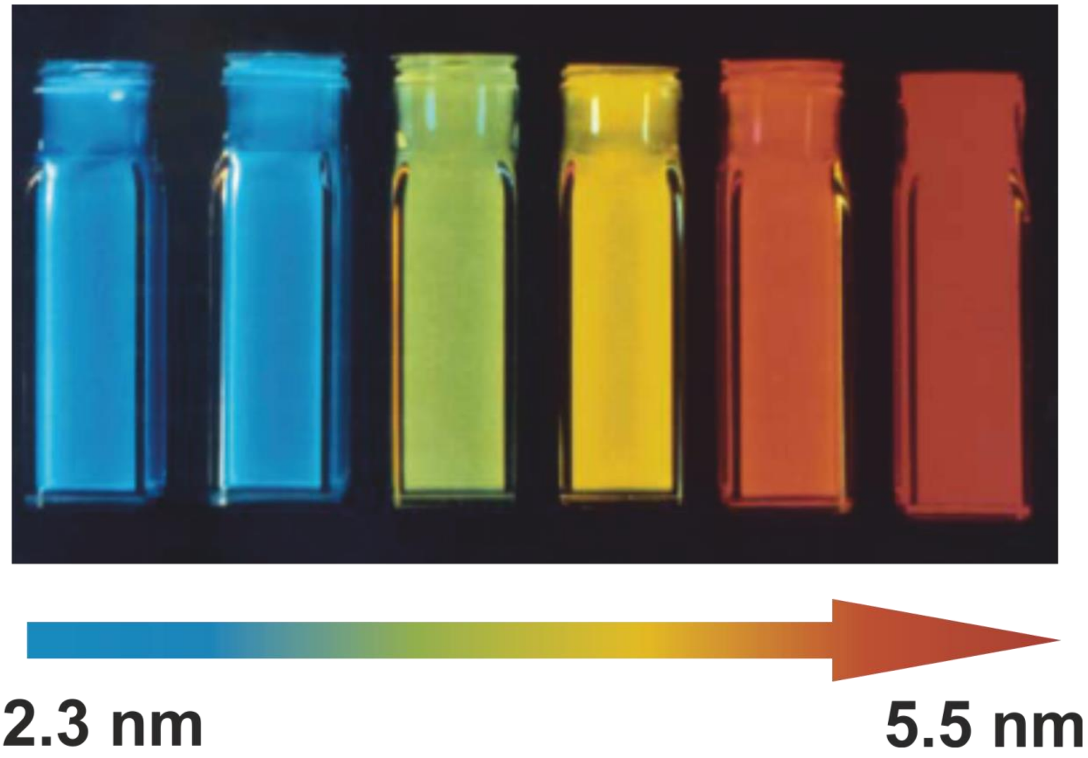

**Figure 1.1.2-2** The emission of CdSe/ZnS quantum dots is highly dependent on their size[39].

Unlike molecular fluorophores, quantum dots are extremely resistant to photobleaching providing them with a much longer lifetime; this gives them particular advantages for applications in biology and medicine as immunostaining markers and as diagnostic tools (see Chapter 1.1.3).

### *1.1.3 The drive for stimulus responsive nanoparticles in biomedical applications*

The use of nanoparticles for medical applications has gained a lot of interest recently as there are many potential uses for them depending on their characteristics. The primary focus of this thesis is on preparing UV responsive titanium dioxide (specifically anatase) nanoparticles for photodynamic therapy (PDT) (see chapter 1.3.2). Using stimulus responsive nanoparticles for biomedical applications is gaining a considerable amount of attention recently, especially in the field of drug delivery and therapeutics. The main interest lies in the fact that a relatively inert material can be administered into the body and only when it is triggered do they become “active” i.e. release encapsulated drugs, produce cytotoxic substances etc. Therefore, by using such accurate systems, normal healthy cells and tissues can remained unharmed by the therapeutics thus leading to a drop in the number of side effects and an increase in efficacy of the active agents.

In general most research has been focused on the design of systems which are responsive to one of three internal stimuli. The first of these stimuli is changes in pH as when cells ingest extracellular material they are transported in lysosomes which have a local pH of 5 compared to the physiological pH 7.4. A lot of attention has been directed at producing drug carriers, typically constructed of polymeric constituents, that are stable at physiological pH but undergo structural changes in the lysosomes and release their payload[40-42]. By labelling the drug carriers with antigens there is the possibility to target them towards specific cells in the body[43].

In cancer therapeutics it has been noted that tumours exhibit microenvironments which are under mild hyperthermia where the local temperature is 1-2 °C above that of healthy tissue[44]. Once again polymeric drug delivery systems, which are sensitive to changes in temperature, may be used to deliver drugs to these sites. However, for both pH and thermo responsive systems, the changes are sometimes so slight that it can be difficult to design systems which are stable under normal physiological conditions and “active” under the slightly different conditions of the targeted site.

Sites of inflammation often have a high local concentration of ROS and attention is being directed towards preparing delivery systems that undergo chemical changes upon contact with ROS. These systems are typically based on poly(propylene sulphide) (PPS). Various constructs can be created with PPS such as cross linked nanoparticles or micelles, which are formed by the self-assembly of block copolymers of PPS, which is hydrophobic and a hydrophilic polymer such as poly(glycerolmonomethacrylate) PGMMA[45]. Upon contact with ROS, PPS is oxidised to sulfoxides and further to sulfones which are hydrophilic[46]. By incorporating an anti-inflammatory drug within the core of the PPS constructs it can be transported around the body and only released in areas of high ROS concentration i.e. sites of inflammation.

Using external, i.e. out of body, stimuli to trigger a response in previously administered materials is one direction in which the field of responsive therapeutics is highly promising. This technique relies on a highly stable system which is introduced to the body and allowed to accumulate in the desired region. The material can then be activated by an external trigger without need to rely on *in vivo* stimuli. For example, using magnetic responsive therapeutics has high prospects as a magnetic field can pass through the entire body and reach any tissue[47, 48]. For example Bridot *et. al.* have shown that $Gd_2O_3$ nanoparticles greatly enhance contrast during magnetic resonance imaging (MRI) compared to currently used contrast agents[49]. It was also shown that as the nanoparticle size decreased the contrast increased due to longer relaxation times of the nanoparticles. However, the reliance of toxic heavy metals such as gadolinium and chromium for such systems limits their applicability[50, 51].

Carregal-Romero *et. al.* have recently reported the development of polyelectrolyte multilayer (PEM) hollow core microcapsules for the NIR triggered release of encapsulated macromolecules[52]. The PEM microspheres were grown by the layer by layer (LbL) addition of poly(styrene sulfonate) and poly(allyl amine) around a calcium carbonate ($CaCO_3$) core. After preparation the $CaCO_3$ could be removed by complexing with ethylenediaminetetraacetic acid (EDTA) leaving a hollow core behind. It has been shown that similar PEM microcapsules have large pores, ~ 13 nm, present in the polymer walls which allow the penetration of molecules into the core. However, upon heating the polymers are raised above their glass transition temperature ($T_g$) and rearrange shrinking the pore size to ~ 5 nm, entrapping any large macromolecules inside[53]. Carregal-Romero *et. al.* modified the walls of the microcapsules by embedding gold nanoparticles into them and upon illumination with NIR radiation the gold nanoparticles induced a drastic rise in local temperature causing the microcapsules to release their payload.

Using light as an external stimulus is not a new concept; however the applicability of such systems has been restricted due to the low penetration of light within bodily tissues. The window of the electromagnetic spectrum that can be used medically has defined limits. The wavelength of light used must be between 300-1000 nm, below this region the radiation administered is too damaging to human tissue and above it $H_2O$ absorbs the majority of the radiation reducing its penetration depth. However between these limits it is has been shown that as the wavelength increases so does the penetration depth of the light. Eichler *et. al.* have shown that the transmission of light with a wavelength of 400 nm is only 20 % in a tissue depth of 0.4 mm. However, when using a wavelength of 700 nm transmission is 70 % and when the tissue depth was increased to 1 mm penetration using a wavelength of 700 nm remained decent at 40 %[54]. The reason why much of the light administered does not penetrate is because of absorption by haemoglobin which has a strong absorbance at 540 and 576 nm with a lot of scattering in the region of 300-450 nm[55]. However between 700-1000 nm the penetration of light in tissue can reach several millimetres[56]. Due to the limited penetration of light in tissue one would think that any technique that relies of the use of illumination would not be very efficient. However recent advances in micron sized endoscopy[57] and dual photon microscopy[58] (which involves exciting a fluorophore with two photons of lower energy than that needed for one photon excitation) have improved the administration of light into bodily tissues many times over.

### *1.1.4 The medical potential for stimulus responsive inorganic nanoparticles*

Cells are typically around 10 µm in diameter, organelles have typical dimensions of 0.2-5 µm (depending on the organelle) and proteins have sizes in the range of around 5 nm, meaning nanoparticles have the ability to interact with cells on a level as small as that of proteins.

There is a large push to understand biological processes on the nanoscale and quantum dots have a great potential for use as cellular probes for monitoring cellular processes. As mentioned above the high stability of quantum dots is in itself a pronounced advantage over traditional fluorescent probes, however the ability to modify the surface, for example with antibodies, of the quantum dots to target particular cells *in vivo* holds great possibilities for their use as diagnostic tools.

Bruchex *et. al.* were amongst the first to report the use of bleaching resistant CdSe-CdS quantum dots for biological staining and they detailed a remarkable increase in detectability and stability of the quantum dots compared to classically used markers[59].

Gold nanoparticles are of particular importance in medicine in a field known as photothermal therapy. Hirsch *et. al.* have shown that gold nanoparticles with an average size of 3 nm induce a dramatic change in temperature ($\Delta T = 37.4 \pm 6.6$ °C) in surrounding tissue upon radiation with near infrared (NIR) light[60]. This change in temperature resulted in the irreversible damage of surrounding tissue highlighting the potential of using gold nanoparticles for treating tumours which are located in sensitive areas and may not be treatable by conventional means. Also it has been shown that gold nanoparticles may be suitable for drug delivery applications by co-localising drugs and gold nanoparticles into a thermally responsive organic shell, which is disrupted upon irradiation releasing the payload[61].

Another biomedical use of nanoparticles is as contrast agents for MRI as mentioned previously. Lee *et. al.* have shown that metal ion doped ferrite ($Fe_2O_3$) nanoparticles show enhanced contrast compared to typical contrast agents; in particular the imaging of small tumours that were practically undetectable using traditional means was greatly enhanced[62]. There is an evident potential to use these, and indeed many other, nanoparticles for dual action in that the surface of the nanoparticles can be modified with, for example, cancer therapeutic drugs so that the target sight can be imaged and, if needs be, treated simultaneously.

Indeed the field of stimulus responsive nanoparticles is a rapidly growing one. The primary focus of this thesis is to develop biocompatible $TiO_2$ nanoparticles which become cytotoxic upon UV excitation. The following chapter introduces the many different methods that can be employed for the synthesis of metal oxide, specifically $TiO_2$, nanoparticles.

## 1.2 Metal Oxides

Metal oxide nanoparticles include a diverse range of materials which are useful for many applications including catalysis[63], bactericidal agents[64] and gas sensing[65], just to name a few. Due to the wide range of applications that metal oxide nanoparticles can be used for, a large amount of research is being diverted towards their synthesis. During the synthesis of nanoparticles it is desirable to have a method where high control is kept over the growth of the nanoparticles and that they have a rather uniform size, i.e. they are monodisperse after synthesis. There are a number of methods to produce metal oxide nanoparticles with the most commonplace highlighted below.

### *1.2.1 Overview of synthetic methods*

Traditionally bulk metal oxide materials were prepared by a powder based technique involving the direct reaction of fine powders, however the high temperatures and pressures required for such a reaction negate the ability to produce nanosized structures[66].

Co-precipitation was an early method used for the production of metal oxide nanoparticles. In short the nanoparticles are produced from sparingly soluble precursors in a saturated aqueous solution. Upon nucleation the nanoparticles grow by aggregation and precipitation. However, this method is very crude as all steps of nanoparticle growth being nucleation, growth, coarsening/agglomeration all happen simultaneously and control over the resulting size, shape and uniformity of the nanoparticles is very difficult[67].

Using microemulsions to produce metal oxide nanoparticles is similar to the co-precipitation method. Typically a reverse micelle solution with the metal precursor in the core is added to an aqueous solution, the metal oxide nanoparticles are then produced in the micelle core and as such the resulting size is limited to the size of the micelles, in this process the micelles are often referred to as nanoreactors. Whilst the nanoparticles produced are typically of a uniform nature, heating is required to remove remaining water and to induce crystallinity in the nanoparticles[68]. When heating metal oxide nanoparticles it is inevitable that the nanoparticles agglomerate together, through further condensation reactions, therefore the nano regime and monodispersity are lost[69] (more details on this matter are provided in chapter 1.2.2).

The solvothermal method is a widely used method to produce metal oxide nanoparticles. In short the reaction involves heating the soluble metal precursor up to temperatures higher than the normal boiling point of the solvent however due to the high pressures involved the solvent is actually in a supercritical state[70]. The temperature provided allows the metal precursors to react together creating nanoparticles. This method does indeed allow the synthesis of monodisperse nanoparticles with the size and crystallinity of the products being able to be manipulated by varying the reaction conditions. However, the high pressures and temperatures involved generally make this method of synthesis unfeasible for a general laboratory setup.

Despite the number of methods available to synthesise metal oxide nanoparticles one particular method has gained a rapid amount of attention in recent years. This method is called sol-gel synthesis and this was the method of synthesis employed to produce the nanoparticles presented later on in this thesis. The reasons as to why sol-gel chemistry is the choice method for producing metal oxide nanoparticles, are outlined below.

### *1.2.2 Sol-gel synthesis*

The importance of sol-gel chemistry was first recognised by Ebelmen who reported the synthesis of $SiO_2$ through the hydrolysis of $Si(OC_2H_5)_4$[71]. As the name suggests, in sol-gel synthesis a solid product (gel) is prepared from liquid precursors in solution (sol). For the synthesis of metal oxide nanoparticles there are two main routes available to their production utilising sol-gel techniques. These two methods are aqueous sol-gel and non-aqueous sol-gel and a description of each technique is given below.

Aqueous sol-gel synthesis has been used for many years for the production of metal oxide nanoparticles[72-74]. Typically the reaction involves a soluble metal oxide precursor, typically an alkoxylated or halogenated metal centre, which is dissolved into an aqueous environment. The growth of the nanoparticles is primarily governed by two processes being; 1) the hydrolysis of the ligands on the metal centre and 2) the condensation of these hydroxy ligands to form a metal-oxygen-metal bridge with the release of water. Figure 1.2.2-1 represents the main steps involved in the growth of metal oxide nanoparticles from metal alkoxide precursors dispersed in $H_2O$.

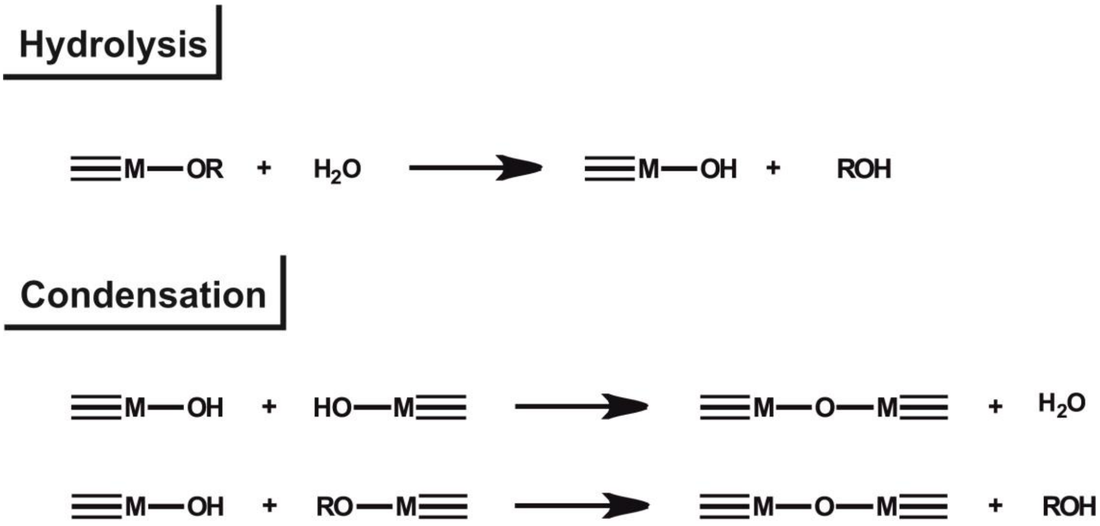

**Figure 1.2.2-1** There are two main steps in aqueous sol-gel synthesis 1) The metal precursor is hydrolysed and 2) The hydroxyl ligands then condense together, or a hydroxyl ligand condenses with a parent alkoxide ligand, forming an oxygen bridge between two metal centres and the release of $H_2O$. Note: Here OR represents an alkoxide, however similar steps happen with a halogenated metal precursor.

Now whilst the reaction does provide nanoparticles there are two major limitations to this method. Firstly the hydrolysis and condensation reactions occur at such fast rates that control over the specific size of the nanoparticles obtained is virtually non-existent. Also, as an effect of the fast reaction rate, there is often a very low degree of crystallisation within the nanoparticles. As a lot of metal oxide nanoparticle applications rely on their crystallinity this is a problem; crystallinity is induced into the nanoparticles by annealing them at temperatures often higher than 600 °C[75]. Whilst heating the nanoparticles induces crystallinity, by providing sufficient energy to rearrange the atoms into a more energy favourable state, the process inevitably induces further condensation between the nanoparticles causing an increase in overall size. As a result of the growing need for controllable and reproducible methods to synthesise metal oxide nanoparticles the sol-gel method was adapted as discussed below.

To combat the problems associated with aqueous sol-gel synthesis, synthetic routes which negated the use of water were developed. Before going any further it should be mentioned that non-aqueous sol-gel synthetic methods may also be split into two categories be they either solvent mediated or surfactant mediated. Surfactant mediated synthesis typically involves the injection of a metal precursor into a hot solvent in the presence of surfactants[76]. These surfactants prevent the agglomeration of the nanoparticles during synthesis therefore the result is highly crystalline nanoparticles with very small dimensions[77]. However, the number of cases where this method has proven successful are limited with the main mechanism of nanoparticle formation poorly understood. Also the use of surfactants results in considerate effort needed to purify the nanoparticles for further use. For these reasons this method of synthesis was disregarded for this thesis, and in its place a solvent mediated non-aqueous sol-gel synthetic method was adopted.

In non-aqueous reactions the starting materials are typically the same as those for the aqueous synthesis i.e. an alkoxylated or halogenated centre which can be dispersed in an aqueous free solvent. For reactions in aqueous solvents the oxygen is provided by the water present whereas for non-aqueous systems the oxygen may be either provided by the parent ligands, e.g. alkoxides, or by substitution of the primary ligands, e.g. halogens, with short chain alcohols such as ethanol[78-80]. The reaction is then heated to commence the condensation reactions. As there are no hydroxy ligands in the non-aqueous synthesis the condensation reactions occur between the oxygen bearing ligands present on the metal precursors. For example, when using alkoxylated precursors the alkoxides may condense together forming ethers[81]. However, since for non-aqueous sol-gel synthesis the process is typically carried out in alcohols with high boiling points, such as benzyl alcohol, they may also substitute the parent alkoxides leading to the possibility of a combination of ethers being released upon condensation (Figure R)[81, 82]. When starting from a halogenated metal centre it is also possible for the condensation to occur between a halogen and alkoxide resulting in the release of a halgenoalkane[83]. All these condensation pathways are made possible due to the fact that substitution reactions never reach 100 % and an equilibrium always exists. Therefore, there will always be a variety of ligands present on the metal precursors during the condensation steps. Figure R illustrates a number of routes available for the production of metal oxides from metal alkoxide/halide precursors in benzyl alcohol (the choice solvent for the synthesis of $TiO_2$ nanoparticles in this thesis).

The list of examples given in Figure 1.2.2-2 is not exhaustive and only outlines modes of condensation which are the most apparent. In some cases the role of the solvent may not be as clear cut as that shown. Niederberger *et. al.* have reported the synthesis of various perovskite type nanoparticles (i.e. alkaline earth $TiO_3$ blends such as $BaTiO_3$, $SrTiO_3$ etc.) in benzyl alcohol[84]. They revealed that during the condensation step barely any ethers are formed, in fact the main by-product observed was 4-phenyl-2-butanol. Whilst the reaction mechanism for the formation of this by-product is not shown here, briefly it involves the formation of a C-C bond between the α carbon of the alcohol solvent and the β carbon of the $Ti(O^iPr)_4$ precursor leading to the formation of a Ti-O-Ti bridge and the release of 4-phenyl-2-butanol.

Due to the fact of steric hindrance and the lower reactivity of alkoxide, relative to hydroxy ligands, the rate of condensation reactions is much reduced compared to aqueous methods[85]. Therefore the size of the nanoparticles can be controlled to a much higher degree when using non-aqueous solvents. Also, due to the slow condensation rate, the growth of the nanoparticles is governed by thermodynamics rather than kinetics and therefore the nanoparticles typically exhibit a high degree of crystallinity[86].

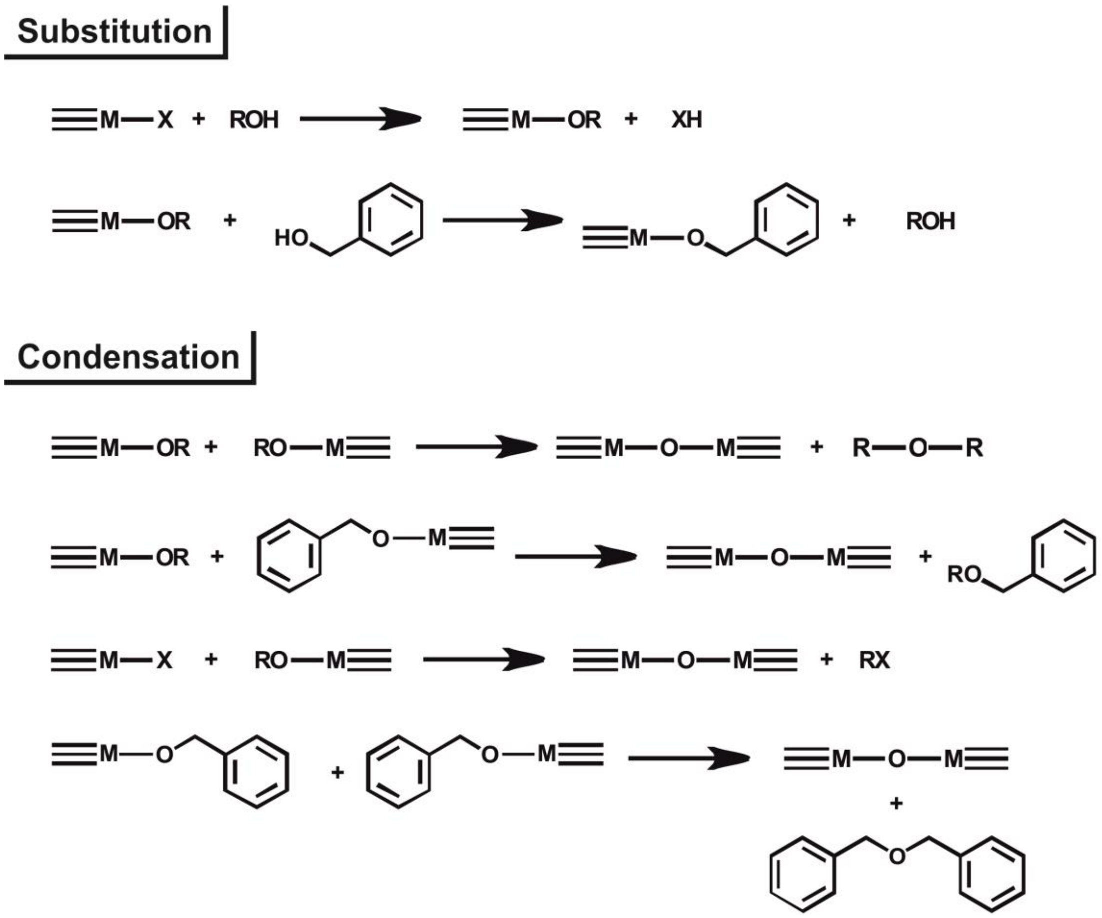

**Figure 1.2.2-2** An illustration of the possible processes taking place during a non-aqueous sol-gel synthesis. Substitution reactions may occur where the ligand on the metal precursor may be liberally interchanged between parent alkoxide, parent halides and the solvent the reaction is taking place in. Due to the wide number of metal-ligand precursors a large number of routes can be employed during the condensation step resulting in various ethers or halogenoalkanes being produced. However, regardless of the route employed the metal-oxygen-metal bridge is formed in all cases.

### 1.2.3 The application of the sol-gel method for $TiO_2$ nanoparticle preparation

Due to the fact that a high degree of control can be kept over the resulting properties of nanoparticles a non-aqueous sol-gel synthetic method was adopted for the synthesis of $TiO_2$ nanoparticles in this thesis. The fact that the reaction can be carried out under mild conditions and with standard laboratory equipment was also a driving force to use this method rather than using a solvothermal method.

Niederberger *et. al.* have demonstrated that titanium tetrachloride ($TiCl_4$) dispersed in benzyl alcohol upon heating to various temperatures from 40 to 150 °C produces $TiO_2$ nanoparticles[87]. The size of the nanoparticles was governed by reaction temperature and time of reaction however in all cases $TiO_2$ nanoparticles with an average size between 5-8 nm were produced. X-ray powder diffraction (XRD) patterns of the nanoparticles showed that they were highly crystalline with only the anatase form of $TiO_2$ present, more details on the crystalline phases of $TiO_2$ can be found in chapter 1.4. This method of synthesis is particularly interesting for the production of nanoparticles which are intended for biomedical use because of the choice of solvent. Benzyl alcohol is widely used in the food and cosmetics industry due to it being highly biocompatible and the fact that it is quickly metabolised to benzoic acid and further to hippuric acid which is then excreted from the body[88]. Therefore benzyl alcohol is a choice solvent for the production of biomaterials over using more toxic solvents such as dichloromethane (DCM), dimethylformamide (DMF) etc..

It has recently been shown in our group that $TiO_2$ nanoparticles may be produced by prior alkoxylation of $TiCl_4$ with ethanol and subsequent dispersion in benzyl alcohol[89]. After heating to 80 °C for 9 hours highly crystalline anatase nanoparticles with an average size of around 9 nm were produced. The nanoparticles were then able to be easily redispersed into an aqueous environment at a low pH to prevent their aggregation through electrostatic repulsion. This is therefore ideal for our synthesis as the control of using an organic solvent for synthesis is kept whilst dispersion into an aqueous environment, which is vital for use *in vivo*, is allowed. This method of synthesis has been adopted for the synthesis of the nanoparticles used in this research as it was desirable to produce anatase nanoparticles with size ranges around the 10 nm mark which were dispersible in an aqueous environment. However, it has been documented that using halogenated titanium precursors may hinder the resulting photoactivity of the nanoparticles due to the poisoning of surface sites, therefore, for this project, the tetraalkoxide precursor was used directly rather than alkoxylating the tetrachloride precursor in situ[90]. Also by using the fully alkoxylated precursor the ambiguity around the exact metal species undergoing condensation was removed, thus leading to a more controlled reaction.

## 1.3 Titanium dioxide

$TiO_2$ is a very diverse material and has found uses in many applications including pigments in paints[91], gas sensing[92], water purification[93], photovoltaics[94], sunscreen[95] and self-cleaning windows[96]. The majority of applications that utilise $TiO_2$ can be split into two main categories being energy production and catalysis, both of which rely on the unique photoactive capability the metal oxide exhibits. It is its photoactivity along with $TiO_2$ being extremely biocompatible, which has made it a viable candidate for biomedical applications[9].

### *1.3.1 Current uses of micro/nano $TiO_2$*

When $TiO_2$ is illuminated with near UV light an electron is promoted from the valence to the conduction band. Upon splitting, the electron and the positive hole are free to migrate to the surface of the crystal and transfer their energy to surface adsorbed species. It is this transfer of energy from the bulk crystal to the surrounding area which is of particular interest for this thesis and more detail is given in chapter 1.3.2. For example in self-cleaning windows the $TiO_2$ is activated by sunlight and the excitons react with any organic matter on the surface of the window, breaking it down and therefore allowing the matter to be more easily washed from the surface the next time it rains[97]. The same applies to water purification where any organic contaminants are broken down upon illumination. In aqueous systems however the contaminants do not necessarily need to be adsorbed on the $TiO_2$ to be broken down. Instead energy can be transferred from the surface of $TiO_2$ to surface adsorbed $H_2O$ or $O_2$ releasing ROS. These ROS then diffuse away from the surface of the $TiO_2$ and degrade any organic matter in the vicinity; this is discussed in greater detail in the next chapter (1.3.2).

In sunscreen the $TiO_2$ absorbs any harmful UV radiation before it reaches and damages the skin. The phenomenon of energy transfer is restricted by coating the nanoparticles with aluminium oxide which halts the migration of the excitons thus stopping the nanoparticles from reacting with the skin. In photovoltaics, dyes, typically ruthenium complexes, are adsorbed onto the surface of the $TiO_2$, it is these dyes rather than the metal oxide which act as the photoactive agent in this case[94] and $TiO_2$ acts to propagate and aid the transfer of the created excitons which can be integrated into an electrical circuit. The reason for using dyes is that $TiO_2$ is activated by UV light which at ground level only makes up a small percentage of the incoming solar radiation[98]; whereas, the addition of a dye shifts the maximum absorbance of the system to wavelengths of > 500 nm which penetrate the atmosphere a lot more than UV allowing a higher proportion of the incoming solar radiation to be utilised[99, 100]. The idea of using dyes to shift the maximum absorbance of the $TiO_2$-dye complex is visited again later in this thesis in Chapter 1.4.2.

Recently $TiO_2$ nanoparticles have received considerable interest for use as *in vivo* transport agents[101-103]. For these applications it is not their photoactivity but their relatively low toxicity, coupled with the ease of surface modification, which give them high potential as transport scaffolds. In particular, a number of research groups are modifying the surface of $TiO_2$ nanoparticles with novel MRI contrast agents. For example, Paunesku *et. al.* have modified the surface of $TiO_2$ nanoparticles with gadolinium MRI contrast agents, which were attached onto the nanoparticle surface using catechols (see Chapter 1.4.2 for more details)[104]. They reported a significant increase in intracellular accumulation, retention and subcellular localization compared to the free contrast agent. It has also been hypothesised that the surface of $TiO_2$ nanoparticles may be further modified in order to enhance cellular uptake. Coating the nanoparticles with folic acid has been shown to increase uptake into tumour cells in mice[105].

Due to its low toxicity and unique photoactive properties the future of nano-$TiO_2$ is looking bright for now, and with the recent explosion in the number of publications related to the application of $TiO_2$ in biomedicine, the trend is set to continue for many years to come.

### *1.3.2 The structure of $TiO_2$*

Three main crystalline forms of $TiO_2$ are rutile, anatase and brookite and all three have slightly different band gaps at 3.05, 3.26 and 3.27 eV respectively[106, 107]. Using Equation 1.3.2-1 the wavelengths of light required to promote an electron into the valence band for each crystalline form are 413 nm for rutile, 380 nm for anatase and 376 nm for brookite.

$$\lambda = \left(\frac{ch}{e}\right)\left(\frac{1}{b}\right)$$

**Equation 1.3.2-1** Where λ is the wavelength of light, c is the speed of light, h is Planck's constant, e is the elementary charge and b is the band gap.

From their activation wavelengths you would expect that the most photoactive crystal form of $TiO_2$ would be rutile followed by anatase and finally brookite. Whilst it is certainly true that brookite is the least photoactive it has been found that anatase is actually more photoactive than rutile. The reason behind anatase having a higher photoactivity is the fact that the recombination rate of the electrons with the holes is around ten times less than that found for rutile[108]. Therefore for many applications an anatase structure is required for the $TiO_2$ and this fits in with a non-aqueous sol-gel synthetic method as it predominantly produces anatase nanoparticles whereas processes involving calcination often produce a mixture of anatase and rutile phases[109]. It was indeed the aim to produce anatase nanoparticles for this thesis as these are the most photoactive making them the most suitable crystal form of $TiO_2$ for photodynamic therapy (PDT).

## 1.4 Photodynamic therapy

PDT was first developed around 100 years ago where von Tappeiner and Jesionek first saw that when eosin was in contact with skin tumours and then illuminated with white light the tumour size shrank over time[110]. In PDT an active component, known as a photosensitizer (PS), is administered to the body, either intravenously or topically. Under illumination an electron is excited into a higher energy state and in an oxygenated aqueous solution the sensitizer can then transfer the energy to surrounding molecules, either $H_2O$ or $O_2$, creating ROS which can induce apoptosis and cell death in surrounding tissue.

To date there are a several photosensitizers approved for commercial use with each one usually falling into the category of either porphyrins, chlorophylls or dyes, and they are used to treat a wide range of maladies ranging from a number of different cancers to psoriasis. Photofrin was the first commercially available PDT sensitizer and it is composed of a mixture of oligomers of up to eight porphyrin units which has a wavelength of activation of 630nm and was approved for use to treat bladder cancer in 1993[111]. Meyer-Betz was the first person to test the effects of porphyrin on humans, himself in fact, in 1913[110]. After applying porphyrin to certain areas of his skin, especially hands and face he went for a short walk. On his return he noticed that the areas which were exposed to sunlight were inflamed and sore and 3 days after exposure the areas inflamed had swollen so much that he became almost unrecognisable. The swelling and pain Meyer-Betz experienced was due to the reaction of ROS with his skin and in modern treatment exposure to light is one of the major problems with PDT, typically when being treated the patient must stay out of strong light, both artificial and sunlight, for up to 2 weeks.

Typically it has been found that the main ROS produced upon illumination is singlet oxygen ($^1O_2$). Upon illumination the sensitizer is excited and promotes an electron to a higher energy singlet state. This singlet state has a very short lifetime and usually undertakes one of two relaxation pathways either radiative emission in the form of fluorescence and relax back down to ground state, or it may undergo internal conversion producing heat. However, the excited PS may undergo intersystem crossing to a relatively long lived triplet state. It is this triplet state which is required in the PDT mechanism and which will ultimately undergo energy conversion to produce an array of ROS in one of two ways. In the type one reaction the PS directly transfers an electron or proton to adsorbed species which typically create hydroxyl radicals ($^{\bullet}OH$), superoxide anions ($O_2^{\bullet -}$) or peroxide ($H_2O_2$). Alternatively a type 2 reaction may occur in which the triplet state PS directly transfers its energy to molecular oxygen to produce singlet oxygen (Figure 1.4-1)[112]. After production the ROS are free to disperse into the surrounding media where they induce apoptosis in neighbouring cells by reacting with unsaturated fatty acid chains and side chains of certain amino acids[113]. The main advantage of PDT over conventional cancer treatments is the fact that the active agent is generally non-toxic when it is not illuminated. Also the light source used to excite the photosensitizer can be directed with great accuracy therefore only the affected areas of the body are targeted leaving healthy tissue unharmed.

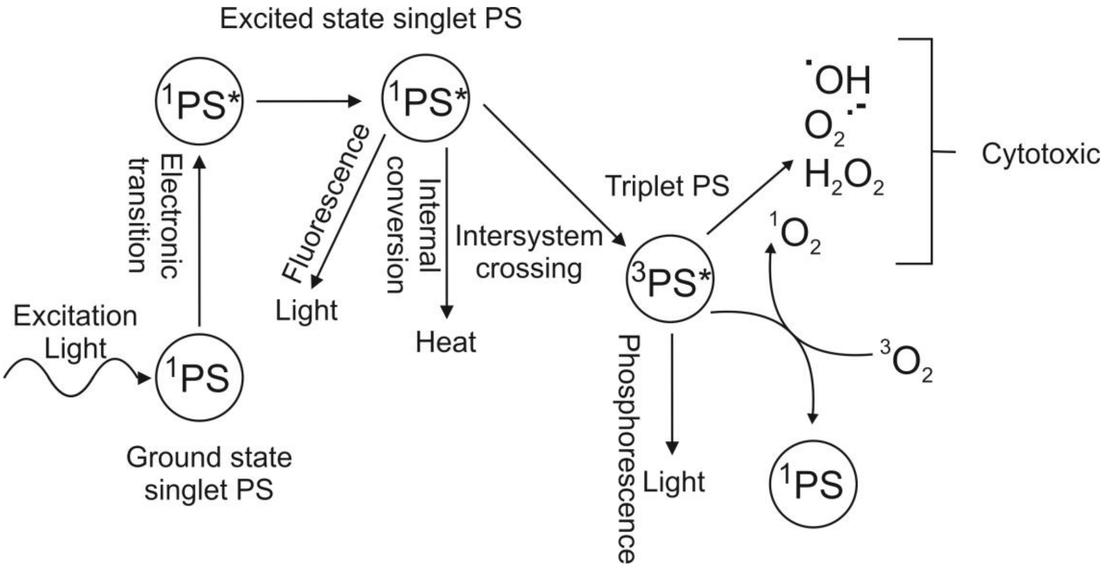

**Figure 1.4-1** Schematical representation of the energy conversion pathways typically undertaken by a PS under illumination. (Figure modified from Ref. 100).

It has been hypothesised for some time now that $TiO_2$ may be used as the next generation of photosensitizer in PDT. Although the wavelength of activation of $TiO_2$ is short, thus dropping the penetration potential of light in tissue, there are a number of benefits to use $TiO_2$ being 1) The surface of the $TiO_2$ can be easily modified thus allowing the attachment of a wide range of anitbodies, such as tumour specific antigens (e.g. CA-125[114], carcinoembryonic antigen[115] etc.) to allow specific targeting of cells within the body, thus limiting unwanted sensitization; 2) The photoactivity of $TiO_2$ is directly related to its surface area therefore the photoactivity can be dramatically increased in the nano regime; 3) The production cost of $TiO_2$ is extremely low and highly reproducible unlike commonly used sensitizers which are typically derived from blood samples.

Under illumination in aqueous conditions it has been reported that $TiO_2$ also produces $^1O_2$ however the predominant ROS formed is actually the superoxide anion ($O_2^{\cdot -}$) along with a whole host of other secondary reactive oxygen species. The electron and hole pair created upon illumination move to the surface of the nanoparticle as previously described. Here a number of processes take place 1) the electron reduces an electron acceptor, primarily this occurs as $O_2$ being reduced to $O_2^{\cdot -}$; 2) the hole oxidises an adsorbed electron donor, this happens in two ways, the conversion of $H_2O$ to $^{\cdot}OH$ or the conversion of surface titanols to radical titanol species (Figure 1.4-2)[106]. It has also been seen that positive holes can directly oxidise adsorbed species which is particularly influential for applications in water decontamination[116]. Secondary ROS, such as $H_2O_2$, can be produced with further energy transfer reactions of the primary ROS.

After their production the ROS diffuse in the surrounding solution, the lifetimes and migration distances of the most common ROS produced upon $TiO_2$ illumination are given in Table 1.4-1 and it is clear that $O_2^{\cdot -}$ is the longest lived, which may be the reason why it has been shown to be the most prominent ROS produced upon $TiO_2$ illumination.

**Table 1.4-1** The half-lives and diffusion distances on the 3 most common ROS produced upon illuminating $TiO_2$ with UV light. Please note, the half-lives and distances are given in orders of magnitude rather than definitive values as they typically depend on the concentration of the ROS.

| ROS | Half-life | Diffusion distance |
|---|---|---|
| $^1O_2$ | μs[117] | nm[118] |
| $^{\cdot}OH$ | ns[119] | Å[119] |
| $O_2^{\cdot -}$ | ms[120] | μm[120] |

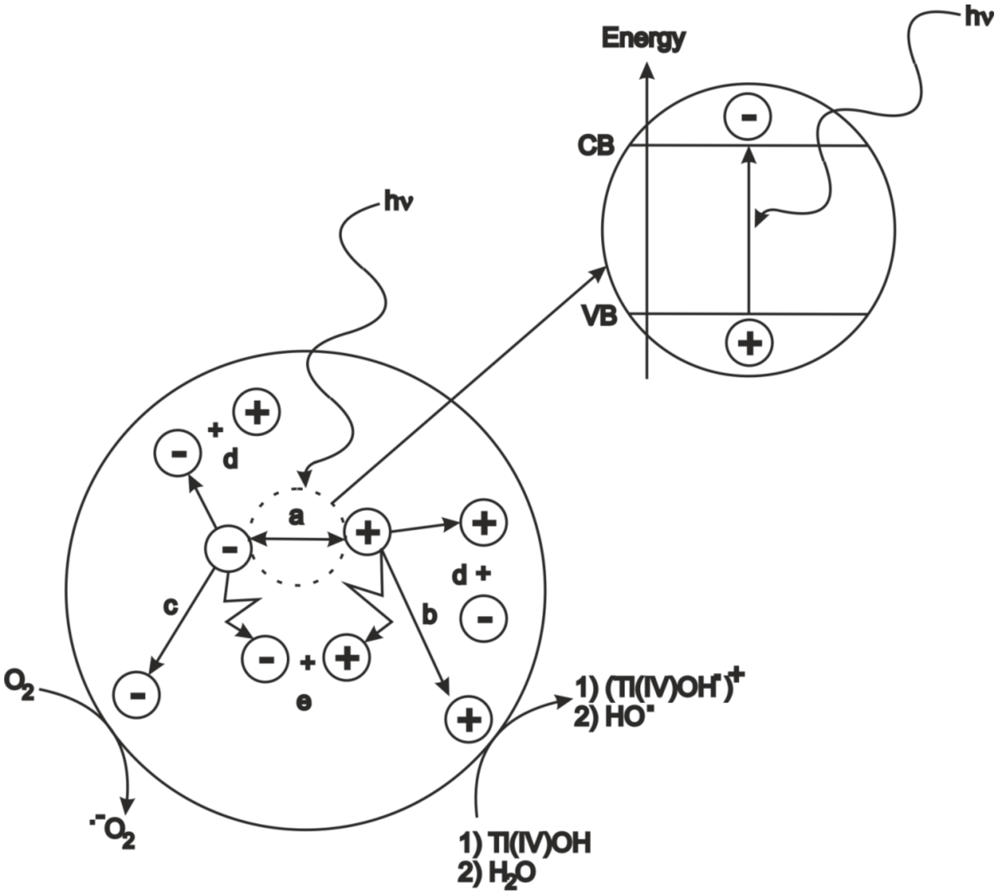

**Figure 1.4-2** Scheme indicating the main processes occurring within a $TiO_2$ nanoparticle under illumination. a) electron-hole generation; b) migration of positive holes to the nanoparticle surface resulting in the oxidation of an electron donor; c) migration of the electron to the nanoparticle surface resulting in the reduction of an electron acceptor; d) recombination of the electron hole pair at the surface of the nanoparticle; e) electron hole pair recombination in the bulk of the nanoparticle. (Figure modified from Reference 112).

## 1.5 The design of $TiO_2$ nanoparticles for photodynamic therapy: Chemical, physical and biological aspects

The design of $TiO_2$ nanoparticles for PDT has to take into account a number of different aspects, from the size and structure of the nanoparticles to the post-coating of the nanoparticles in order to extend their lifetime *in vivo*. This section aims to explain the rationale behind the design of the $TiO_2$ nanoparticles for PDT.

### *1.5.1 $TiO_2$ nanoparticles: Synthesis, size and structure*

When designing materials for use *in* vivo it is necessary to minimise the use of toxic or harmful reagents during the synthesis. As mentioned previously, a non-aqueous sol-gel method in benzyl alcohol was chosen for the synthesis of the nanoparticles. Benzyl alcohol is highly biocompatible and can be rapidly metabolised and excreted by the body therefore any residual traces in the final nanoparticle product, however unlikely, will not cause any adverse effects[88]. However, the benzyl alcohol route was also chosen for more pressing reasons than for biocompatibility alone.

When using non-deformable nanoparticles *in vivo* there is an upper limit on their usable size. This limit is ~ 200 nm and is set by the spleen as any nanoparticles larger than this cut off limit are rapidly filtered out rendering them useless[121]. Also there is a lower cut off limit of ~ 5 nm this is to ensure that the nanoparticles remain above the size of where quantum confinement effects start to take place[122]. The lower limit is typically of little concern as synthesising nanoparticles with a size lower than 5 nm is not very commonplace. Rather, the upper limit of 200 nm causes most problems in the synthesis of nanoparticles for biomedical applications. However, due to the high degree of control that the non-aqueous synthetic route allows, the production of metal oxide nanoparticles with diameters of less than 200 nm is quite readily achievable[123, 124]. Particularly, $TiO_2$ nanoparticles have been synthesised in benzyl alcohol on a number of occasions with dimensions between below this upper limit[125-127].

Regardless of the fact that nanoparticles with diameters less than 200 nm need to be used for *in vivo* applications, there is also an added bonus for producing $TiO_2$ at the nanoscale. The photoactivity of $TiO_2$ is directly linked to the number of surface sites present, therefore it stands to reason that as you reduce the size of the particles the overall photo-oxidative efficiency of the nanoparticles increases due to the increase in surface area to volume ratio[128].

After synthesis the nanoparticles need to be removed from the parent solvent and redispersed in an aqueous environment if they are to be used in biomedical applications. This step is typically quite crucial as it is here that a large amount of agglomeration can occur between the nanoparticles resulting in an overall increase in size. However, once again the benzyl alcohol route guards against excessive agglomeration. In particular Kotsokechagia *et. al.* have previously shown that $TiO_2$ nanoparticles synthesised in benzyl alcohol could be redispersed in a 50:50 mix of $H_2O$:Ethanol, at pH 2, with only a minor degree of aggregation occurring resulting in an increase in size from 10 to 35 nm[89]. The ability for the nanoparticles to be redispersed in this solvent mixture is due to the fact that alkoxide ligands are present on the surface of the nanoparticles after synthesis, these hinder agglomeration which occurs through further condensation between surface hydroxyl ligands. After redipsersion the nanoparticles can be purified through dialysis resulting in "naked" (i.e. solely hydroxyl ligands coating the surface) nanoparticles. A major point to address here is the need for the nanoparticles to be redispersed in an acidic (pH 2) solution, this is due to the fact that $TiO_2$ has an isoelectric point ~ pH 4.8 – 6.2[129]. Redispersing the nanoparticles into an acidic solution protonates the surface of the nanoparticles and prevents unwanted agglomeration through electrostatic repulsion. Therefore if the nanoparticles were redispersed at neutral pH they would agglomerate immediately rendering them useless for biomedical applications. Here in though lies a problem as inevitably the nanoparticles will need to be dispersed into a solution at physiological pH (pH 7). If the nanoparticles were left naked they would inevitably agglomerate. Consequently the surface of the nanoparticles needs to be coated with a suitable ligand in order to prevent agglomeration at neutral pH ($TiO_2$ surface coatings are discussed further in Chapter 1.5.2).

Finally, as well as size, control needs to be kept over the crystal structure of the resulting nanoparticles. As previously mentioned there are three main crystal forms of $TiO_2$, being anatase, rutile and brookite, and the anatase modification has been shown to be the most photoactive[108]. Therefore for this project it was desired that the nanoparticles not only had diameters in the nano regime but that they exhibited a mostly anatase structure. Once again the benzyl alcohol route for the synthesis of $TiO_2$ nanoparticles favours the formation of nanoparticles with an anatase morphology[89, 127]. This is due to the slow condensation rate of the titanium precursors, allowing the nanoparticles to orientate themselves into a crystalline morphology.

From the above discussion it was concluded that in order to optimise the photoactivity of the $TiO_2$ nanoparticles and to enable their application *in vivo* they had to have average diameters in the nanoregime (< 200 nm), have a predominantly anatase phase and be dispersible in an aqueous medium. The non-aqueous sol-gel route in benzyl alcohol allowed fine control over all these characteristics and was deemed suitable for this study. However, upon redispersion the nanoparticles were only stable at acidic pH therefore the surface of the nanoparticles needed to be modified in order for them to be redispersed at physiological pH.

### *1.5.2 $TiO_2$ nanoparticles: Surface composition and biological aspects*

In order to disperse the nanoparticles at neutral pH it is necessary to modify the surface of the nanoparticles to prevent them from agglomerating. This can be done *via* one of two ways by either modifying the surface charge of the nanoparticles or attaching sufficiently bulky groups to the surface, which prevent the surface of the nanoparticles from coming into contact through steric interference.

Dispersing the nanoparticles at acidic pH prevents them from agglomerating due to electrostatic repulsion between the positively charged surfaces. Upon neutralising the solution there is effectively no charge on the surface of the nanoparticles thus they agglomerate and precipitate out of solution. The addition of surface groups which remain or become charged at neutral pH is one way to stabilise the nanoparticles. For example, the nanoparticles may be coated with a suitable ligand which has a carboxylic acid tail. Upon neutralisation the carboxylic acid will deprotonate leaving a carboxylate present on the nanoparticle surface[130]. At a sufficient ligand density the carboxylates will prevent agglomeration through electrostatic repulsion much in the same way as protonating the surface at acidic pH. On the other hand quaternary amines may be used to stabilise the nanoparticles, and since their charge is not dependant on the pH of the solution, the nanoparticles will be stable at a wide range of pH's. However, whilst the nanoparticles will be stable, charged nanoparticles will be rapidly recognised *in vivo* and their lifetime will be much reduced[131]. The method of recognition is outlined below along with a method to evade detection and extend the lifetime of the nanoparticles *in vivo*.

Following injection into the bloodstream many nanoparticles are rapidly detected and eliminated out of the bloodstream. The main method of removal is the mononuclear phagocyte system (MPS) coupled with the complement system[132]. There is a second method of elimination of nanoparticles and this depends on the size of the particles themselves. For particles >200 nm in size the nanoparticles will accumulate and agglomerate in the spleen. Therefore, as previously mentioned, it is necessary for the particles to be of a size less than 200 nm to avoid filtration out of the bloodstream[133]. These responses present a problem for nanoparticles within a biological environment as elimination is often too swift and many particles are practically detected and eliminated almost immediately without sufficient time for them to have a therapeutic effect.

The complement system is the main method of recognition of nanoparticles in the blood stream. Nanoparticles are recognised by complement proteins, known as opsonins, such as C3b, immunoglobulins G and M and fibronectin to name just a few, overall around 30 binding proteins are known to be utilised as opsonins in the human body[132]. There are a number of activation pathways that opsonins can undertake, but in regard to nanoparticles the main pathway involves the adsorption of these complement proteins onto the nanoparticle surface, this process is known as opsonisation. Following adsorption, MPS cells are recruited, which recognise the adsorbed proteins with the use of specific receptors found on the cells surface and subsequently bind the proteins to the surface of the MPS cells. After binding to the cell surface, the nanoparticle may be then invaginated within the cell *via* an endocytic mechanism (discussed below)[132].

The MPS (also known as the reticuloendothelial system) is the other major form of blood clearance response to nanoparticles and colloidal structures[132]. The MPS is made up of two main classes of cells, these being macrophages and monocytes. The main role of the MPS is to remove dead cells from the bloodstream and to remove dead cells and foreign bodies from the blood stream following recruitment by complement proteins as previously discussed[132, 134]. MPS cells uptake foreign bodies by an irreversible process known as endocytosis, where the cell membrane of the MPS cell surrounds the foreign body and pinches off forming a vesicle within the cell trapping the foreign material[135, 136]. There are three main methods of endocytosis, these being phagocytosis, pinocytosis and receptor mediated endocytosis, and all three are described in more detail below.

Phagocytosis (meaning cell eating) is an active process performed by MPS cells, such as macrophages and neutrophils, *via* the use of specific or non-specific receptors to engulf larger particles of a size greater than 0.5 µm[132]. Phagocytic cells are used alongside the complement system and phagocytosis is the main method of endocytosis following opsonisation of the foreign body[137].

Pinocytosis (meaning cell drinking) on the other hand, involves the non-specific uptake of solute molecules *via* non-coated vesicles and does not involve the use of receptors on the surface of the cells[132].

The final method of endocytosis that remains to be discussed is receptor mediated endocytosis. On the surface of a number of MPS cells membranes, specific receptors may be found which bind to specific ligands or anti-bodies[135]. For example on the surface of lymphocytes the low density lipoprotein receptor may be expressed and it binds to LDL which, in turn, enables the invagination of cholesterol into the cell[135]. There are a large number of receptors present on the surface of cells and any invading body (such as nanoparticles) which complement these receptors will quickly be internalised by MPS cells.

After internalisation in the cell, the vesicle containing internalised material, will be transported and fused with endosomes and lysosomes[132]. Biological materials would then normally undergo either degradation then excretion out of the body or be recycled within the cell. However, if the nanoparticle is inorganic, it is not typically degraded by the lysosomes. Instead it is rather thought that inorganic particles remain in the body indefinitely encapsulated in a vesicle, rendering them inert.

From the above discussion, it can be concluded that to be of any effect in therapeutics, nanoparticles need to be designed to by-pass the MPS when circulating in the bloodstream. One way to accomplish this task is to conjugate protein repellent hydrophilic polymers to the surface of the nanoparticles which (as the name suggests) disguise the nanoparticles for the MPS and allowing extended circulation times.

Coating the nanoparticles with a protein repellent polymer may not only be beneficiary for extending the lifetime of the nanoparticles *in vivo*, but also for stabilising the nanoparticles at neutral pH. It has been shown on a number of occasions that adsorbing polymers of a sufficient molecular weight and surface grafting density stabilises nanoparticles against aggregation. Here the stability is not related to electrostatic repulsion but to the steric interference between polymer chains thus restricting the surface of the nanoparticles from coming into contact with one another.

Pain *et al.* were one of the first to report that polysaccharide (particularly dextran) coated liposomes had a circulatory half-life twice of that of “naked” liposomes[138]. This increase in circulatory time was relatively modest and research was conducted into polymers that increase the half-life further. The next major class of molecules found to increase the half-life was glycolipids, such as monosialoganglioside $GM_I$[139]. Glycolipids proved highly effective at evading the MPS, particularly in the liver and a two-fold decrease in uptake has been observed[139]. Although effective, glycolipids have two major drawbacks, the first being their cost and the second being the difficulty in their purification. Studies into the surface modification of liposomes with $GM_I$ yielded separate results from different research groups. It was found that even the smallest impurity in the glycolipid used resulted in a reduced effect of the "stealth" giving character[139].

Research into surface modification using polyethylene glycol (PEG) actually predated that of polysaccharides, and its importance was overlooked for many years. Abuchowski *et al.* reported studies in 1977 into modifying bovine serum albumin with PEG and the results showed a dramatic increase in evasion of the MPS[140]. PEG has undoubtedly received the most interest recently in modifying the surface of inorganic nanoparticles as it is already food and drug administration (FDA) approved for drug use. It has been noted that PEG with an average molecular weight of 1000 – 2000 $gmol^{-1}$ increases the circulation half-life substantially and PEG is a popular choice for the surface coating of biomaterials[139]. Further functionalisation of the terminal OH group on PEG can lead to the polymer being chemically grafted to ligands which have an affinity for adsorbing onto the surface of inorganic structures[141]. Due to the wide use of PEG in coating inorganic nanoparticles it seems that PEG derivatives will be suitable in coating $TiO_2$ nanoparticles in this project[142, 143].

Before PEG can be adsorbed onto the surface of the $TiO_2$ nanoparticles it is necessary to conjugate it to a suitable ligand which has a high affinity for adsorbing to the surface of $TiO_2$. There are quite a number of ligands which have the ability to adsorb onto $TiO_2$ but without doubt there are two classes of ligands which stand out, these are catechols[144, 145] and phosph(on)ates[146, 147] (Figure 1.5.2-1). Catechols are rigid 1,2 diols which have gained a considerable amount of attention for the surface modification of $TiO_2$. The ligand binds to unsaturated $TiO_2$ sites, where a site is unsaturated if the titanium is bound to a hydroxyl ligand which are highly labile. Each titanium atom in titanium dioxide forms 6 bonds to oxygen atoms and in macroscopic $TiO_2$ surface titanium atoms typically only have one unsaturated surface site. Therefore, when catechols adsorb onto macroscopic $TiO_2$ they bridge two titanium centres. However, due to the curvature of the nanoparticles, on the nanoscale, surface titanium atoms typically have multi unsaturated sites therefore and each catechol can bind solely to one titanium centre in a chelating fashion resulting in the formation of a five membered ring[144]. The rigid structure of the 1,2 diols of catechols means that they readily bind in a chelating fashion. Catechols are particularly interesting for the surface modification of $TiO_2$ where the nanoparticles have to remain photoactive. This is due to fact that when catechols adsorb onto the surface of $TiO_2$ the $\lambda_{max}$ of the system shifts from ~ 380 nm to 435 nm i.e. the visible region[148]. Therefore it is theorised that light of a longer wavelength can be used to excite the nanoparticles. For biomedical applications this is particularly interesting as the longer the wavelength of light the deeper the penetration into bodily tissue.

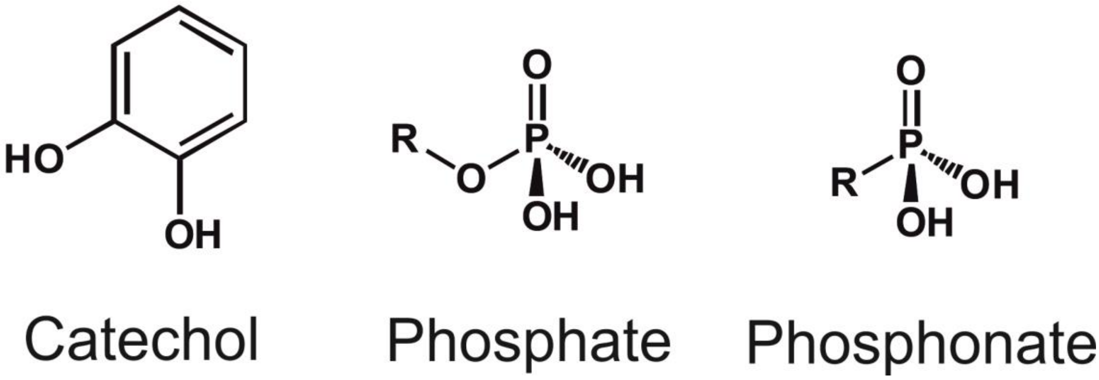

**Figure 1.5.2-1** Skeletal structures of catechols, phosphates and phosphonates.

Research into the surface modification of $TiO_2$ using phosph(on)ates is gradually gaining more interest in recent years. Phosph(on)ates have similar adsorption properties to catechols where the ligand can adsorb by bridging two metal centres or chelate in a bidentate fashion directly to one centre[149] and it has also been noted that they can bind in a tridentate fashion[146]. Catechols and phosph(on)ates also seem to have relatively similar binding constants between $10^3$ and $10^4$ $M^{-1}$ therefore they are both suitable ligands for the surface of $TiO_2$[150, 151]. However, phosph(on)ates do not cause a shift in the $\lambda_{max}$ of the $TiO_2$ system towards the visible light region therefore the nanoparticles remain photoactive under near UV illumination. On the other hand phosph(on)ates have been reported to increase the photooxidative capability of $TiO_2$

quite substantially. For example Zhang *et. al.* have shown that modifying the surface of $TiO_2$ nanoparticles increases the photodegradation rate of 4-chlorophenol, phenol and Rhodamine blue. The increase in rate was attributed to the fact that upon adsorption phosph(on)ates donate a negative charge to the surface of the $TiO_2$[152]. This negative charge enhances the positive hole migration to the surface of the nanoparticles resulting in a much increased production of the $^{\bullet}OH$ radical.

For this thesis catechols and phosph(on)ates were used to tether PEG to the surface of the $TiO_2$ nanoparticles. Both ligands were chosen for their high binding efficiency towards $TiO_2$ and the fact that they both have the potential to enhance the photoactivity in drastically different ways.

## 1.6 Scope of thesis and Authors Contribution

The development of stimulus responsive biomaterials has gained much attention in recent years for applications such as drug delivery and cancer therapeutics. This thesis reports the development of hybrid titanium dioxide polymeric nanoparticles for biomedical applications, in particular for use in PDT and stimuli-responsive drug delivery systems.

The project can be divided into a number of stages with the first being the synthesis of water dispersible $TiO_2$ nanoparticles. It was desired that the nanoparticles were monodisperse with an average diameter of between 5-200 nm, with the goal being to produce nanoparticles as small as possible in order to increase the surface area to volume ratio and in effect increase their photoactivity. It was also desired that the nanoparticles had an anatase crystallinity in order to enhance their photodegradative capability even further. Chapter 2 reports the results into the synthesis of $TiO_2$ nanoparticles through a predominantly non-aqueous sol-gel synthetic method using benzyl alcohol as the reaction solvent. For this reaction molar equivalents of $H_2O$ were added in order to a) decrease the reaction time and b) gain fine control over the synthesis of the nanoparticles.

Chapter 3 reports the results into the surface functionalisation of the $TiO_2$ nanoparticles with a variety of ligands all based on either catechols or phosph(on)ates. The stability of the nanoparticles was assessed at physiological pH as a function of ligand species and grafting density. Subsequently the effect of surface composition on the photodegradative capability of the nanoparticles was assessed. The photoactivity was assessed by monitoring the degradation of methylene blue (MB) under illumination in the presence of the nanoparticles either coated or uncoated. MB is highly susceptible to ROS degradation in solution and it's degradation can be easily recorded by monitoring the subsequent decrease in its absorbance at 665 nm over time.

Chapter 4 introduces the results into using the $TiO_2$ nanoparticles for a different application other than PDT. Here we have created PEM microcapsules with the $TiO_2$ nanoparticles embedded within the walls. The microcapsules could be loaded with a model dye and under illumination the ROS created were able to damage and rupture the polymer walls and subsequently release the model dye within.

### *1.6.1 Author's Contributions*

Dr. Andrea Pucci performed the thermogravimetric analysis runs in Chapter 2 contributing to 0.5% of this overall thesis. Dr. Ghislaine Robert-Nicoud synthesised the dye conjugated polymers for chapter 4 and also co-supervised Mr. Qamar Hussain in procuring a number of the results, 3 % of this thesis is attributed to each of them. The remaining 93.5% of this thesis was done solely by the author Mr. Christopher J. Cadman.

## 1.7 References

1. Gottesman, M. M.; Pastan, I., Biochemistry of multidrug-resistance mediated by the multidrug transporter. *Annu. Rev. Biochem.* **1993,** 62, 385-427.

2. Evans, W. E.; McLeod, H. L., Drug therapy - Pharmacogenomics - Drug disposition, drug targets, and side effects. *N. Engl. J. Med.* **2003,** 348, (6), 538-549.

3. Alivisatos, P., The use of nanocrystals in biological detection. *Nat. Biotechnol.* **2004,** 22, (1), 47-52.

4. Brigger, I.; Dubernet, C.; Couvreur, P., Nanoparticles in cancer therapy and diagnosis. *Adv. Drug Deliv. Rev.* **2002,** 54, (5), 631-651.

5. Rosi, N. L.; Mirkin, C. A., Nanostructures in biodiagnostics. *Chem. Rev.* **2005,** 105, (4), 1547-1562.

6. Niemeyer, C. M., Nanoparticles, proteins, and nucleic acids: Biotechnology meets materials science. *Angew. Chem.-Int. Edit.* **2001,** 40, (22), 4128-4158.

7. Medintz, I. L.; Uyeda, H. T.; Goldman, E. R.; Mattoussi, H., Quantum dot bioconjugates for imaging, labelling and sensing. *Nat. Mater.* **2005,** 4, (6), 435-446.

8. Diebold, U., The surface science of titanium dioxide. *Surf. Sci. Rep.* **2003,** 48, (5-8), 53-229.

9. Zhang, D. Q.; Li, G. S.; Wang, H. B.; Chan, K. M.; Yu, J. C., Biocompatible Anatase Single-Crystal Photocatalysts with Tunable Percentage of Reactive Facets. *Cryst. Growth Des.* **2010,** 10, (3), 1130-1137.

10. Song, M.; Zhang, R. Y.; Dai, Y. Y.; Gao, F.; Chi, H. M.; Lv, G.; Chen, B. A.; Wang, X. M., The in vitro inhibition of multidrug resistance by combined nanoparticulate titanium dioxide and UV irradition. *Biomaterials* **2006,** 27, (23), 4230-4238.

11. Loo, C.; Lowery, A.; Halas, N. J.; West, J.; Drezek, R., Immunotargeted nanoshells for integrated cancer imaging and therapy. *Nano Lett.* **2005,** 5, (4), 709-711.

12. Mroz, P.; Tegos, G. P.; Gali, H.; Wharton, T.; Sarna, T.; Hamblin, M. R., Photodynamic therapy with fullerenes. *Photochem. Photobiol. Sci.* **2007,** 6, (11), 1139-1149.

13. Ivask, A.; Bondarenko, O.; Jepihhina, N.; Kahru, A., Profiling of the reactive oxygen species-related ecotoxicity of CuO, ZnO, TiO(2), silver and fullerene nanoparticles using a set of recombinant luminescent Escherichia coli strains: differentiating the impact of particles and solubilised metals. *Anal. Bioanal. Chem.* **2010,** 398, (2), 701-716.

14. Faraday, M., The Bakerian lecture: experimental relations of gold (and other metals) to light. *Philos. T. R. Soc Lond* **1847,** 147, 145-181.

15. Feynman, R., There's Plenty of Room at the Bottom. *The Caltech Alumni Magazine,* **February 1960,** reprinted *J. Microelectromech. S.* **1992,** 1, 60.

16. Binnig, G.; Rohrer, H., Scanning tunneling microscopy. *Helv. Phys. Acta* **1982,** 55, (6), 726-735.

17. Kroto, H. W.; Heath, J. R.; Obrien, S. C.; Curl, R. F.; Smalley, R. E., C-60 - Buckminsterfullerene. *Nature* **1985,** 318, (6042), 162-163.

18. Tadros, T.; Izquierdo, R.; Esquena, J.; Solans, C., Formation and stability of nano-emulsions. *Adv. Colloid Interface Sci.* **2004,** 108, 303-318.

19. Avella, M.; De Vlieger, J. J.; Errico, M. E.; Fischer, S.; Vacca, P.; Volpe, M. G., Biodegradable starch/clay nanocomposite films for food packaging applications. *Food Chem.* **2005,** 93, (3), 467-474.

20. Nazeeruddin, M. K.; Kay, A.; Rodicio, I.; Humphrybaker, R.; Muller, E.; Liska, P.; Vlachopoulos, N.; Gratzel, M., Conversion of light to electricity by cis-x2bis(2,2'-bipyridyl-4,4'-dicarboxylate)ruthenium(ii) charge-transfer sensitizers (x = cl-, br-, i-, cn-, and scn-) on nanocrystalline $TiO_2$ electrodeS. *J. Am. Chem. Soc.* **1993,** 115, (14), 6382-6390.

21. Wu, X. Y.; Liu, H. J.; Liu, J. Q.; Haley, K. N.; Treadway, J. A.; Larson, J. P.; Ge, N. F.; Peale, F.; Bruchez, M. P., Immunofluorescent labeling of cancer marker Her2 and other cellular targets with semiconductor quantum dots. *Nat. Biotechnol.* **2003,** 21, (1), 41-46.

22. Nel, A.; Xia, T.; Madler, L.; Li, N., Toxic potential of materials at the nanolevel. *Science* **2006,** 311, (5761), 622-627.

23. Maynard, A. D.; Aitken, R. J.; Butz, T.; Colvin, V.; Donaldson, K.; Oberdorster, G.; Philbert, M. A.; Ryan, J.; Seaton, A.; Stone, V.; Tinkle, S. S.; Tran, L.; Walker, N. J.; Warheit, D. B., Safe handling of nanotechnology. *Nature* **2006,** 444, (7117), 267-269.

24. Tsuji, J. S.; Maynard, A. D.; Howard, P. C.; James, J. T.; Lam, C. W.; Warheit, D. B.; Santamaria, A. B., Research strategies for safety evaluation of nanomaterials, part IV: Risk assessment of nanoparticles. *Toxicol. Sci.* **2006,** 89, (1), 42-50.

25. Auffan, M.; Rose, J.; Bottero, J. Y.; Lowry, G. V.; Jolivet, J. P.; Wiesner, M. R., Towards a definition of inorganic nanoparticles from an environmental, health and safety perspective. *Nat. Nanotechnol.* **2009,** 4, (10), 634-641.

26. Selin, C., Expectations and the emergence nanotechnology. *Sci. Technol. Hum. Values* **2007,** 32, (2), 196-220.

27. http://ec.europa.eu/environment/chemicals/nanotech/index.htm#definition Nanomaterials.

28. Stankovich, S.; Dikin, D. A.; Piner, R. D.; Kohlhaas, K. A.; Kleinhammes, A.; Jia, Y.; Wu, Y.; Nguyen, S. T.; Ruoff, R. S., Synthesis of graphene-based nanosheets via chemical reduction of exfoliated graphite oxide. *Carbon* **2007,** 45, (7), 1558-1565.

29. Teo, W. E.; Ramakrishna, S., A review on electrospinning design and nanofibre assemblies. *Nanotechnology* **2006,** 17, (14), R89-R106.

30. Pileni, M. P., Nanosized particles made in colloidal assemblies. *Langmuir* **1997,** 13, (13), 3266-3276.

31. Wang, Y.; Herron, N., Nanometer-sized semiconductor clusters - materials synthesis, quantum size effects, and photophysical properties. *J. Phys. Chem.* **1991,** 95, (2), 525-532.

32. Alivisatos, A. P., Semiconductor clusters, nanocrystals, and quantum dots. *Science* **1996,** 271, (5251), 933-937.

33. Astruc, D.; Lu, F.; Aranzaes, J. R., Nanoparticles as recyclable catalysts: The frontier between homogeneous and heterogeneous catalysis. *Angew. Chem.-Int. Edit.* **2005,** 44, (48), 7852-7872.

34. Haruta, M.; Kobayashi, T.; Sano, H.; Yamada, N., Novel gold catalysts for the oxidation of carbon-monoxide at a temperature far below 0-degrees-c. *Chem. Lett.* **1987**, (2), 405-408.

35. Yoffe, A. D., Low-dimensional systems - quantum-size effects and electronic-properties of semiconductor microcrystallites (zero-dimensional systems) and some quasi-2-dimensional systems. *Adv. Phys.* **1993,** 42, (2), 173-266.

36. Murray, C. B.; Norris, D. J.; Bawendi, M. G., Synthesis and characterization of nearly monodisperse cde (e = s, se, te) semiconductor nanocrystallites. *J. Am. Chem. Soc.* **1993,** 115, (19), 8706-8715.

37. Yu, J. H.; Joo, J.; Park, H. M.; Baik, S. I.; Kim, Y. W.; Kim, S. C.; Hyeon, T., Synthesis of quantum-sized cubic ZnS nanorods by the oriented attachment mechanism. *J. Am. Chem. Soc.* **2005,** 127, (15), 5662-5670.

38. Samia, A. C. S.; Dayal, S.; Burda, C., Quantum dot-based energy transfer: Perspectives and potential for applications in photodynamic therapy. *Photochem. Photobiol.* **2006,** 82, (3), 617-625.

39. Dabbousi, B. O.; RodriguezViejo, J.; Mikulec, F. V.; Heine, J. R.; Mattoussi, H.; Ober, R.; Jensen, K. F.; Bawendi, M. G., (CdSe)ZnS core-shell quantum dots: Synthesis and characterization of a size series of highly luminescent nanocrystallites. *J. Phys. Chem. B* **1997,** 101, (46), 9463-9475.

40. Bae, Y.; Fukushima, S.; Harada, A.; Kataoka, K., Design of environment-sensitive supramolecular assemblies for intracellular drug delivery: Polymeric micelles that are responsive to intracellular pH change. *Angew. Chem.-Int. Edit.* **2003,** 42, (38), 4640-4643.

41. Dong, L. C.; Hoffman, A. S., A novel-approach for preparation of ph-sensitive hydrogels for enteric drug delivery. *Journal of Controlled Release* **1991,** 15, (2), 141-152.

42. Du, J. Z.; Tang, Y. Q.; Lewis, A. L.; Armes, S. P., pH-sensitive vesicles based on a biocompatible zwitterionic diblock copolymer. *J. Am. Chem. Soc.* **2005,** 127, (51), 17982-17983.

43. Roy, D.; Nehilla, B. J.; Lai, J. J.; Stayton, P. S., Stimuli-Responsive Polymer-Antibody Conjugates via RAFT and Tetrafluorophenyl Active Ester Chemistry. *ACS Macro Lett.* **2013,** 2, (2), 132-136.

44. Vaupel, P.; Kallinowski, F.; Okunieff, P., Blood-flow, oxygen and nutrient supply, and metabolic microenvironment of human-tumors - a review. *Cancer Res.* **1989,** 49, (23), 6449-6465.

45. Vo, C.-D.; Cadman, C. J.; Donno, R.; Goos, J. A. C. M.; Tirelli, N., Combination of Episulfide Ring-Opening Polymerization With ATRP for the Preparation of Amphiphilic Block Copolymers. *Macromol. Rapid Comm.* **2013,** 34, (2), 156-162.

46. Napoli, A.; Valentini, M.; Tirelli, N.; Muller, M.; Hubbell, J. A., Oxidation-responsive polymeric vesicles. *Nat. Mater.* **2004,** 3, (3), 183-189.

47. Giri, S.; Trewyn, B. G.; Stellmaker, M. P.; Lin, V. S. Y., Stimuli-responsive controlled-release delivery system based on mesoporous silica nanorods capped with magnetic nanoparticles. *Angew. Chem.-Int. Edit.* **2005,** 44, (32), 5038-5044.

48. Hu, S. H.; Tsai, C. H.; Liao, C. F.; Liu, D. M.; Chen, S. Y., Controlled Rupture of Magnetic Polyelectrolyte Microcapsules for Drug Delivery. *Langmuir* **2008,** 24, (20), 11811-11818.

49. Bridot, J. L.; Faure, A. C.; Laurent, S.; Riviere, C.; Billotey, C.; Hiba, B.; Janier, M.; Josserand, V.; Coll, J. L.; Vander Elst, L.; Muller, R.; Roux, S.; Perriat, P.; Tillement, O., Hybrid gadolinium oxide nanoparticles: Multimodal contrast agents for in vivo imaging. *J. Am. Chem. Soc.* **2007,** 129, (16), 5076-5084.

50. Watanabe, T.; Tammer, R.; Boretius, S.; Frahm, J.; Michaelis, T., Chromium(VI) as a novel MRI contrast agent for cerebral white matter: Preliminary results in mouse brain in vivo. *Magn. Reson. Med.* **2006,** 56, (1), 1-6.

51. Caravan, P.; Ellison, J. J.; McMurry, T. J.; Lauffer, R. B., Gadolinium(III) chelates as MRI contrast agents: Structure, dynamics, and applications. *Chemical Reviews* **1999,** 99, (9), 2293-2352.

52. Carregal-Romero, S.; Ochs, M.; Rivera-Gil, P.; Ganas, C.; Pavlov, A. M.; Sukhorukov, G. B.; Parak, W. J., NIR-light triggered delivery of macromolecules into the cytosol. *J. Control. Release* **2012,** 159, (1), 120-127.

53. Kohler, K.; Sukhorukov, G. B., Heat treatment of polyelectrolyte multilayer capsules: A versatile method for encapsulation. *Adv. Funct. Mater.* **2007,** 17, (13), 2053-2061.

54. Eichler, J.; Knof, J.; Lenz, H., Measurements on depth of penetration of light (0.35-1.0mu-m) in tissue. *Radiat. Environ. Biophys.* **1977,** 14, (3), 239-242.

55. Horecker, B. L., The absorption spectra of hemoglobin and its derivatives in the visible and near infra-red regions. *J. Biol. Chem.* **1943,** 148, (1), 173-183.

56. Frangioni, J. V., In vivo near-infrared fluorescence imaging. *Curr. Opin. Chem. Biol.* **2003,** 7, (5), 626-634.

57. Mahalati, R. N.; Gu, R. Y.; Kahn, J. M., Resolution limits for imaging through multi-mode fiber. *Optics Express* **2013,** 21, (2), 1656-1668.

58. Helmchen, F.; Denk, W., Deep tissue two-photon microscopy. *Nat. Methods* **2005,** 2, (12), 932-940.

59. Bruchez, M.; Moronne, M.; Gin, P.; Weiss, S.; Alivisatos, A. P., Semiconductor nanocrystals as fluorescent biological labels. *Science* **1998,** 281, (5385), 2013-2016.

60. Hirsch, L. R.; Stafford, R. J.; Bankson, J. A.; Sershen, S. R.; Rivera, B.; Price, R. E.; Hazle, J. D.; Halas, N. J.; West, J. L., Nanoshell-mediated near-infrared thermal therapy of tumors under magnetic resonance guidance. *Proc. Natl. Acad. Sci. U. S. A.* **2003,** 100, (23), 13549-13554.

61. Huschka, R.; Zuloaga, J.; Knight, M. W.; Brown, L. V.; Nordlander, P.; Halas, N. J., Light-Induced Release of DNA from Gold Nanoparticles: Nanoshells and Nanorods. *J. Am. Chem. Soc.* **2011,** 133, (31), 12247-12255.

62. Lee, J. H.; Huh, Y. M.; Jun, Y.; Seo, J.; Jang, J.; Song, H. T.; Kim, S.; Cho, E. J.; Yoon, H. G.; Suh, J. S.; Cheon, J., Artificially engineered magnetic nanoparticles for ultra-sensitive molecular imaging. *Nat. Med.* **2007,** 13, (1), 95-99.

63. Oelerich, W.; Klassen, T.; Bormann, R., Metal oxides as catalysts for improved hydrogen sorption in nanocrystalline Mg-based materials. *J. Alloy. Compd.* **2001,** 315, (1-2), 237-242.

64. Stoimenov, P. K.; Klinger, R. L.; Marchin, G. L.; Klabunde, K. J., Metal oxide nanoparticles as bactericidal agents. *Langmuir* **2002,** 18, (17), 6679-6686.

65. Pinna, N.; Neri, G.; Antonietti, M.; Niederberger, M., Nonaqueous synthesis of nanocrystalline semiconducting metal oxides for gas sensing. *Angew. Chem.-Int. Edit.* **2004,** 43, (33), 4345-4349.

66. Jansen, M., A concept for synthesis planning in solid-state chemistry. *Angew. Chem.-Int. Edit.* **2002,** 41, (20), 3747-3766.

67. Bond, G. C.; Tahir, S. F., Vanadium-oxide monolayer catalysts - preparation, characterization and catalytic activity. *Appl. Catal.* **1991,** 71, (1), 1-31.

68. Cong, Y.; Zhang, J. L.; Chen, F.; Anpo, M., Synthesis and characterization of nitrogen-doped TiO2 nanophotocatalyst with high visible light activity. *J. Phys.Chem. C* **2007,** 111, (19), 6976-6982.

69. Wang, C.; Zhao, J. C.; Wang, X. M.; Mai, B. X.; Sheng, G. Y.; Peng, P.; Fu, J. M., Preparation, characterization and photocatalytic activity of nano-sized ZnO/SnO2 coupled photocatalysts. *Appl. Catal. B-Environ.* **2002,** 39, (3), 269-279.

70. Kempaiah, D. M.; Yin, S.; Sato, T., A facile and quick solvothermal synthesis of 3D microflower CeO2 and Gd:CeO2 under subcritical and supercritical conditions for catalytic applications. *Crystengcomm* **2011,** 13, (3), 741-746.

71. Ebelmen, Untersuchungen über die Verbindungen der Borsäure und Kieselsäure mit Aether. *Liebigs Ann. Chem.* **1846,** 57, (3), 319-355.

72. Pelizzetti, E.; Minero, C.; Borgarello, E.; Tinucci, L.; Serpone, N., Photocatalytic activity and selectivity of titania colloids and particles prepared by the sol-gel technique - photooxidation of phenol and atrazine. *Langmuir* **1993,** 9, (11), 2995-3001.

73. Balmer, M. L.; Lange, F. F.; Jayaram, V.; Levi, C. G., Development of nano-composite microstructures in $ZrO_2$-$Al_2O_3$ via the solution precursor method. *J. Am. Ceram. Soc.* **1995,** 78, (6), 1489-1494.

74. Kan, S. H.; Yu, S.; Peng, X. G.; Zhang, X. T.; Li, D. M.; Xiao, L. Z.; Zou, G. T.; Li, T. J., Formation process of nanometer-sized cubic ferric oxide single crystals. *J. Colloid Interf. Sci.* **1996,** 178, (2), 673-680.

75. Zak, A. K.; Abrishami, M. E.; Abd Majid, W. H.; Yousefi, R.; Hosseini, S. M., Effects of annealing temperature on some structural and optical properties of ZnO nanoparticles prepared by a modified sol-gel combustion method. *Ceram. Int.* **2011,** 37, (1), 393-398.

76. Donega, C. D.; Liljeroth, P.; Vanmaekelbergh, D., Physicochemical evaluation of the hot-injection method, a synthesis route for monodisperse nanocrystals. *Small* **2005,** 1, (12), 1152-1162.

77. Park, J.; Lee, E.; Hwang, N. M.; Kang, M. S.; Kim, S. C.; Hwang, Y.; Park, J. G.; Noh, H. J.; Kini, J. Y.; Park, J. H.; Hyeon, T., One-nanometer-scale size-controlled synthesis of monodisperse magnetic iron oxide nanoparticles. *Angew. Chem.-Int. Edit.* **2005,** 44, (19), 2872-2877.

78. Cushing, B. L.; Kolesnichenko, V. L.; O'Connor, C. J., Recent advances in the liquid-phase syntheses of inorganic nanoparticles. *Chem. Rev.* **2004,** 104, (9), 3893-3946.

79. Kakihana, M., "Sol-Gel" preparation of high temperature superconducting oxides. *J. Sol-Gel Sci. Technol.* **1996,** 6, (1), 7-55.

80. Vioux, A., Nonhydrolytic sol-gel routes to oxides. *Chem. Mat.* **1997,** 9, (11), 2292-2299.

81. Niederberger, M.; Garnweitner, G.; Pinna, N.; Neri, G., Non-aqueous routes to crystalline metal oxide nanoparticles: Formation mechanisms and applications. *Prog.in Solid State Ch.* **2005,** 33, (2-4), 59-70.

82. Pinna, N.; Garnweitner, G.; Antonietti, M.; Niederberger, M., Non-aqueous synthesis of high-purity metal oxide nanopowders using an ether elimination process. *Adv. Mater.* **2004,** 16, (23-24), 2196-+.

83. Hay, J. N.; Raval, H. M., Synthesis of organic-inorganic hybrids via the non-hydrolytic sol-gel process. *Chem. Mat.* **2001,** 13, (10), 3396-3403.

84. Niederberger, M.; Garnweitner, G.; Pinna, N.; Antonietti, M., Nonaqueous and halide-free route to Crystalline $BaTiO_3$, $SrTiO_3$, and $(Ba,Sr)TiO_3$ nanoparticles via a mechanism involving C-C bond formation. *J. Am. Chem. Soc.* **2004,** 126, (29), 9120-9126.

85. Livage, J.; Henry, M.; Sanchez, C., Sol-gel chemistry of transition-metal oxides. *Prog. Solid State Chem.* **1988,** 18, (4), 259-341.

86. Niederberger, M., Nonaqueous sol-gel routes to metal oxide nanoparticles. *Accounts Chem. Res.* **2007,** 40, (9), 793-800.

87. Niederberger, M.; Bartl, M. H.; Stucky, G. D., Benzyl alcohol and titanium tetrachloride - A versatile reaction system for the nonaqueous and low-temperature preparation of crystalline and luminescent titania nanoparticles. *Chem. Mat.* **2002,** 14, (10), 4364-4370.

88. Cosmetic Ingredient Review, E., Final report on the safety assessment of Benzyl Alcohol, Benzoic Acid, and Sodium Benzoate. *Int. J. Toxicol.* **2001,** 20, 23-50.

89. Kotsokechagia, T.; Cellesi, F.; Thomas, A.; Niederberger, M.; Tirelli, N., Preparation of ligand-free $TiO_2$ (anatase) nanoparticles through a nonaqueous process and their surface functionalization. *Langmuir* **2008,** 24, (13), 6988-6997.

90. Stapleton, D. R.; Konstantinou, I. K.; Mantzavinos, D.; Hela, D.; Papadaki, M., On the kinetics and mechanisms of photolytic/$TiO_2$-photocatalytic degradation of substituted pyridines in aqueous solutions. *Appl. Catal. B-Environ.* **2010,** 95, (1-2), 100-109.

91. Middlemas, S.; Fang, Z. Z.; Fan, P., A new method for production of titanium dioxide pigment. *Hydrometallurgy* **2013,** 131, 107-113.

92. Garzella, C.; Comini, E.; Tempesti, E.; Frigeri, C.; Sberveglieri, G., $TiO_2$ thin films by a novel sol-gel processing for gas sensor applications. *Sens. Actuator B-Chem.* **2000,** 68, (1-3), 189-196.

93. Mills, A.; Davies, R. H.; Worsley, D., Water-purification by semiconductor photocatalysis. *Chem. Soc. Rev.* **1993,** 22, (6), 417-425.

94. Oregan, B.; Gratzel, M., A low-cost, high-efficiency solar-cell based on dye-sensitized colloidal TiO2 films. *Nature* **1991,** 353, (6346), 737-740.

95. Serpone, N.; Dondi, D.; Albini, A., Inorganic and organic UV filters: Their role and efficacy in sunscreens and suncare product. *Inorg. Chim. Acta* **2007,** 360, (3), 794-802.

96. Paz, Y.; Luo, Z.; Rabenberg, L.; Heller, A., Photooxidative self-cleaning transparent titanium-dioxide films on glass. *J. Mater. Res.* **1995,** 10, (11), 2842-2848.

97. Xi, B. J.; Verma, L. K.; Li, J.; Bhatia, C. S.; Danner, A. J.; Yang, H.; Zeng, H. C., $TiO_2$ Thin Films Prepared via Adsorptive Self-Assembly for Self-Cleaning Applications. *ACS Appl. Mater. Interfaces* **2012,** 4, (2), 1093-1102.

98. Madronich, S.; McKenzie, R. L.; Bjorn, L. O.; Caldwell, M. M., Changes in biologically active ultraviolet radiation reaching the Earth's surface. *J. Photoch. Photobio. B* **1998,** 46, (1-3), 5-19.

99. Bach, U.; Lupo, D.; Comte, P.; Moser, J. E.; Weissortel, F.; Salbeck, J.; Spreitzer, H.; Gratzel, M., Solid-state dye-sensitized mesoporous $TiO_2$ solar cells with high photon-to-electron conversion efficiencies. *Nature* **1998,** 395, (6702), 583-585.

100. Hagfeldt, A.; Boschloo, G.; Sun, L. C.; Kloo, L.; Pettersson, H., Dye-Sensitized Solar Cells. *Chem. Rev.* **2010,** 110, (11), 6595-6663.

101. Chen, C.; Lv, G.; Pan, C.; Song, M.; Wu, C. H.; Guo, D. D.; Wang, X. M.; Chen, B. A.; Gu, Z. Z., Poly(lactic acid) (PLA) based nanocomposites - a novel way of drug-releasing. *Biomed. Mater.* **2007,** 2, (4), L1-L4.

102. Abbas, K.; Cydzik, I.; Del Torchio, R.; Farina, M.; Forti, E.; Gibson, N.; Holzwarth, U.; Simonelli, F.; Kreyling, W., Radiolabelling of $TiO_2$ nanoparticles for radiotracer studies. *J. Nanopart. Res.* **2010,** 12, (7), 2435-2443.

103. Arora, H. C.; Jensen, M. P.; Yuan, Y.; Wu, A. G.; Vogt, S.; Paunesku, T.; Woloschak, G. E., Nanocarriers Enhance Doxorubicin Uptake in Drug-Resistant Ovarian Cancer Cells. *Cancer Res.* **2012,** 72, (3), 769-778.

104. Paunesku, T.; Ke, T.; Dharmakumar, R.; Mascheri, N.; Wu, A. G.; Lai, B.; Vogt, S.; Maser, J.; Thurn, K.; Szolc-Kowalska, B.; Larson, A.; Bergan, R. C.; Omary, R.; Li, D. B.; Lu, Z. R.; Woloschak, G. E., Gadolinium-conjugated $TiO_2$-DNA oligonucleotide nanoconjugates show prolonged intracellular retention period and T1-weighted contrast enhancement in magnetic resonance images. *Nanomed.-Nanotechnol. Biol. Med.* **2008,** 4, (3), 201-207.

105. Oyewumi, M. O.; Yokel, R. A.; Jay, M.; Coakley, T.; Mumper, R. J., Comparison of cell uptake, biodistribution and tumor retention of folate-coated and PEG-coated gadolinium nanoparticles in tumor-bearing mice. *J..Control. Release* **2004,** 95, (3), 613-626.

106. Carp, O.; Huisman, C. L.; Reller, A., Photoinduced reactivity of titanium dioxide. *Prog. Solid State Chem.* **2004,** 32, (1-2), 33-177.

107. Mattsson, A.; Osterlund, L., Adsorption and Photoinduced Decomposition of Acetone and Acetic Acid on Anatase, Brookite, and Rutile $TiO_2$ Nanoparticles. *J. Phys. Chem. C* **2010,** 114, (33), 14121-14132.

108. Sclafani, A.; Herrmann, J. M., Comparison of the photoelectronic and photocatalytic activities of various anatase and rutile forms of titania in pure liquid organic phases and in aqueous solutions. *Jo. Phys. Chem.* **1996,** 100, (32), 13655-13661.

109. Hanaor, D. A. H.; Sorrell, C. C., Review of the anatase to rutile phase transformation. *J. Mater. Sci.* **2011,** 46, (4), 855-874.

110. Dolmans, D.; Fukumura, D.; Jain, R. K., Photodynamic therapy for cancer. *Nat. Rev. Cancer* **2003,** 3, (5), 380-387.

111. Dougherty, T. J.; Gomer, C. J.; Henderson, B. W.; Jori, G.; Kessel, D.; Korbelik, M.; Moan, J.; Peng, Q., Photodynamic therapy. *J. Natl. Cancer Inst.* **1998,** 90, (12), 889-905.

112. Castano, A. P.; Demidova, T. N.; Hamblin, M. R., Mechanisms in photodynamic therapy: part one-photosensitizers, photochemistry and cellular localization. *Photodiag. Photodyn.* **2004,** 1, (4), 279-293.

113. Ochsner, M., Photophysical and photobiological processes in the photodynamic therapy of tumours. *J. Photochem. Photobio. B* **1997,** 39, (1), 1-18.

114. Viswanathan, S.; Rani, C.; Delerue-Matos, C., Ultrasensitive detection of ovarian cancer marker using immunoliposomes and gold nanoelectrodes. *Anal. Chim. Acta* **2012,** 726, 79-84.

115. Tang, D. P.; Yuan, R.; Chai, Y. Q., Magnetic core-shell $Fe_3O_4$@Ag nanoparticles coated carbon paste interface for studies of carcinoembryonic antigen in clinical immunoassay. *J. Phys. Chem. B* **2006,** 110, (24), 11640-11646.

116. Kormann, C.; Bahnemann, D. W.; Hoffmann, M. R., Photolysis of chloroform and other organic-molecules in aqueous $TiO_2$ suspensions. *Environ. Sci. Technol.* **1991,** 25, (3), 494-500.

117. Kuimova, M. K.; Yahioglu, G.; Ogilby, P. R., Singlet Oxygen in a Cell: Spatially Dependent Lifetimes and Quenching Rate Constants. *J. Am. Chem. Soc.* **2009,** 131, (1), 332-340.

118. Skovsen, E.; Snyder, J. W.; Lambert, J. D. C.; Ogilby, P. R., Lifetime and diffusion of singlet oxygen in a cell. *J. Phys.Chem. B* **2005,** 109, (18), 8570-8573.

119. Roots, R.; Okada, S., Estimation of life times and diffusion distances of radicals involved in x-ray-induced dna strand breaks or killing of mammalian-cells. *Radiat. Res.* **1975,** 64, (2), 306-320.

120. Saran, M.; Bors, W., Signaling by $O-_2$(-center-dot) and no-center-dot - how far can either radical, or any specific reaction-product, transmit a message under in-vivo conditions. *Chem.-Biol. Interact.* **1994,** 90, (1), 35-45.

121. Albanese, A.; Tang, P. S.; Chan, W. C. W., The Effect of Nanoparticle Size, Shape, and Surface Chemistry on Biological Systems. In *Annu. Rev. Biomed Eng, Vol 14*, Yarmush, M. L.; Duncan, J. S.; Gray, M. L., Eds. Annual Reviews: Palo Alto, 2012; Vol. 14, pp 1-16.

122. Kormann, C.; Bahnemann, D. W.; Hoffmann, M. R., Preparation and characterization of quantum-size titanium-dioxide. *J. Phys. Chem.* **1988,** 92, (18), 5196-5201.

123. Debecker, D. P.; Mutin, P. H., Non-hydrolytic sol-gel routes to heterogeneous catalysts. *Chem. Soc. Rev.* **2012,** 41, (9), 3624-3650.

124. Li, P. Y.; Jiang, W.; Li, F. S., Non-aqueous sol-gel preparation of carbon-supported nickel nanoparticles. *J. Sol-Gel Sci. Technol.* **2013,** 65, (3), 359-366.

125. Wu, B. H.; Guo, C. Y.; Zheng, N. F.; Xie, Z. X.; Stucky, G. D., Nonaqueous Production of Nanostructured Anatase with High-Energy Facets. *J. Am. Chem. Soc.* **2008,** 130, (51), 17563-17567.

126. Koziej, D.; Fischer, F.; Kranzlin, N.; Caseri, W. R.; Niederberger, M., Nonaqueous $TiO_2$ Nanoparticle Synthesis: a Versatile Basis for the Fabrication of Self-Supporting, Transparent, and UV-Absorbing Composite Films. *ACS Appl. Mater. Interfaces* **2009,** 1, (5), 1097-1104.

127. Hsu, Y. C.; Lin, H. C.; Lue, C. W.; Liao, Y. T.; Yang, C. M., A novel synthesis of carbon-coated anatase nanocrystals showing high adsorption capacity and photocatalytic activity. *Appl. Catal. B-Environ.* **2009,** 89, (3-4), 309-314.

128. Yamashita, H.; Ichihashi, Y.; Harada, M.; Stewart, G.; Fox, M. A.; Anpo, M., Photocatalytic degradation of 1-octanol on anchored titanium oxide and on $TiO_2$ powder catalysts. *J. Catal.* **1996,** 158, (1), 97-101.

129. Sharma, V. K., Aggregation and toxicity of titanium dioxide nanoparticles in aquatic environment-A Review. *J. Environ. Sci. Heal. A* **2009,** 44, (14), 1485-1495.

130. Wang, C. X.; Wang, Y.; Xu, L.; Shi, X. D.; Li, X. W.; Xu, X. W.; Sun, H. C.; Yang, B.; Lin, Q., A Galvanic Replacement Route to Prepare Strongly Fluorescent and Highly Stable Gold Nanodots for Cellular Imaging. *Small* **2013,** 9, (3), 413-420.

131. Dobrovolskaia, M. A.; Aggarwal, P.; Hall, J. B.; McNeil, S. E., Preclinical studies to understand nanoparticle interaction with the immune system and its potential effects on nanoparticle biodistribution. *Mol. Pharm.* **2008,** 5, (4), 487-495.

132. Vonarbourg, A.; Passirani, C.; Saulnier, P.; Benoit, J. P., Parameters influencing the stealthiness of colloidal drug delivery systems. *Biomaterials* **2006,** 27, (24), 4356-4373.

133. Brunner, T. J.; Wick, P.; Manser, P.; Spohn, P.; Grass, R. N.; Limbach, L. K.; Bruinink, A.; Stark, W. J., In vitro cytotoxicity of oxide nanoparticles: Comparison to asbestos, silica, and the effect of particle solubility. *Environ. Sci. Technol.* **2006,** 40, (14), 4374-4381.

134. Nagaveni, K.; Sivalingam, G.; Hedge, M. S.; Madras, G., Solar photocatalytic degradation of dyes: high activity of combustion synthesized nano TiO2. *Appl. Catal. B-Environ.* **2004,** 48, (2), 83-93.

135. Bilecka, I.; Niederberger, M., New developments in the nonaqueous and/or non-hydrolytic sol-gel synthesis of inorganic nanoparticles. *Electrochim. Acta* **2010,** 55, (26), 7717-7725.

136. Kimberly, R. P.; Ralph, P., Endocytosis by the mononuclear phagocyte system and autoimmune-disease. *Am. J. Med.* **1983,** 74, (3), 481-493.

137. Li, G. S.; Li, L. P.; Boerio-Goates, J.; Woodfield, B. F., High purity anatase TiO2 nanocrystals: Near room-temperature synthesis, grain growth kinetics, and surface hydration chemistry. *J. Am. Chem. Soc.* **2005,** 127, (24), 8659-8666.

138. Pain, D.; Das, P. K.; Ghosh, P.; Bachhawat, B. K., Increased circulatory half-life of liposomes after conjunction with dextran. *J. Biosci.* **1984,** 6, (6), 811-816.

139. Allen, T. M., The use of glycolipids and hydrophilic polymers in avoiding rapid uptake of liposomes by the mononuclear phagocyte system. *Adv. Drug Deliv. Rev.* **1994,** 13, (3), 285-309.

140. Abuchowski, A.; Vanes, T.; Palczuk, N. C.; Davis, F. F., Alteration of immunological properties of bovine serum-albumin by covalent attachment of polyethylene-glycol. *J. Biol. Chem.* **1977,** 252, (11), 3578-3581.

141. Storm, G.; Belliot, S. O.; Daemen, T.; Lasic, D. D., Surface modification of nanoparticles to oppose uptake by the mononuclear phagocyte system. *Adv. Drug Deliv. Rev.* **1995,** 17, (1), 31-48.

142. Blummel, J.; Perschmann, N.; Aydin, D.; Drinjakovic, J.; Surrey, T.; Lopez-Garcia, M.; Kessler, H.; Spatz, J. P., Protein repellent properties of covalently attached PEG coatings on nanostructured $SiO_2$-based interfaces. *Biomaterials* **2007,** 28, (32), 4739-4747.

143. Rozhkova, E. A.; Ulasov, I.; Lai, B.; Dimitrijevic, N. M.; Lesniak, M. S.; Rajh, T., A High-Performance Nanobio Photocatalyst for Targeted Brain Cancer Therapy. *Nano Letters* **2009,** 9, (9), 3337-3342.

144. Araujo, P. Z.; Morando, P. J.; Blesa, M. A., Interaction of catechol and gallic acid with titanium dioxide in aqueous suspensions. 1. Equilibrium studies. *Langmuir* **2005,** 21, (8), 3470-3474.

145. Jankovic, I. A.; Saponjic, Z. V.; Comor, M. I.; Nedeljlkovic, J. M., Surface Modification of Colloidal TiO2 Nanoparticles with Bidentate Benzene Derivatives. *J. Phys. Chem. C* **2009,** 113, (29), 12645-12652.

146. Bae, E. Y.; Choi, W. Y.; Park, J. W.; Shin, H. S.; Kim, S. B.; Lee, J. S., Effects of surface anchoring groups (Carboxylate vs phosphonate) in ruthenium-complex-sensitized $TiO_2$ on visible light reactivity in aqueous suspensions. *J. Phys. Chem. B* **2004,** 108, (37), 14093-14101.

147. Nilsing, M.; Lunell, S.; Persson, P.; Ojamae, L., Phosphonic acid adsorption at the $TiO_2$ anatase (101) surface investigated by periodic hybrid HF-DFT computations. *Surf. Sci.* **2005,** 582, (1-3), 49-60.

148. Kotsokechagia, T.; Zaki, N. M.; Syres, K.; de Leonardis, P.; Thomas, A.; Cellesi, F.; Tirelli, N., PEGylation of Nanosubstrates (Titania) with Multifunctional Reagents: At the Crossroads between Nanoparticles and Nanocomposites. *Langmuir* **2012,** 28, (31), 11490-11501.

149. Stumm, W., The inner-sphere surface complex - a key to understanding surface reactivity. In *Adv. Chem. Ser.*, Huang, C. P.; Omelia, C. R.; Morgan, J. J., Eds. Amer Chemical Soc: Washington, 1995; Vol. 244, pp 1-32.

150. Creutz, C.; Chou, M. H., Binding of catechols to mononuclear titanium(IV) and to 1-and 5-nm $TiO_2$ nanoparticles. *Inorg. Chem.* **2008,** 47, (9), 3509-3514.

151. Gillaizeau-Gauthier, I.; Odobel, F.; Alebbi, M.; Argazzi, R.; Costa, E.; Bignozzi, C. A.; Qu, P.; Meyer, G. J., Phosphonate-based bipyridine dyes for stable photovoltaic devices. *Inorg. Chem.* **2001,** 40, (23), 6073-6079.

152. Zhao, D.; Chen, C. C.; Wang, Y. F.; Ji, H. W.; Ma, W. H.; Zang, L.; Zhao, J. C., Surface modification of TiO2 by phosphate: Effect on photocatalytic activity and mechanism implication. *J. Phys. Chem. C* **2008,** 112, (15), 5993-6001.

## 1.8 Appendix - Nanocharacterisation Techniques and Examples of Their Application

### *1.8.1 Introduction*

A complete understanding of the properties of nanomaterials requires the combined use of several characterization techniques. Hereafter, some of the most common techniques will be reviewed, providing a succinct theoretical background and examples of their application directly taken from the research work performed in the frame of this thesis. Some of the methods can be employed also in the study of macroscopic materials, while others take advantage of the specificities of the nano scale. Specifically, we will examine X-Ray Diffraction (XRD) and Transmission Electron Microscopy (TEM) as examples of the first group, and Dynamic Light Scattering (DLS) and Atomic Force Microscopy (AFM) as typical of the second group.

### *1.8.2 Experimental Details*

*X-ray diffraction:* XRD pattern of titanium dioxide ($TiO_2$) nanoparticles were obtained in reflection mode with CuK$\alpha$ radiation on an IPD PW1800 diffractometer (PANalytical) using freeze dried nanoparticles, whose synthesis is reported in Chapter 2 of this thesis.

*Transmission electron microscopy*: We have employed amphiphilic block copolymers, namely poly(propylene sulfide)-poly(glycerol monomethacrylate) (PPS-PGMMA) and poly(glycerolmonomethacrylate)-poly(dimethylsiloxane)-poly(glycerolmonomethacrylate) (SilGMMA), whose synthesis is described in reference 1 for PPS-PGMMA[1] and in reference 2 for SilGMMA[2]. The sample preparation for TEM analysis was identical for both classes of block copolymers. Images were acquired on a Philips CM30 HRTEM operated at 300 kV. A 2% aqueous phosphotungstic acid solution (adjusted to pH 7.3 using NaOH 1 M) was used as a contrast enhancer. The grids (mesh 300 Cu, diameter 3.05 mm) were covered with a formvar film and then coated with carbon (Agar Scientific, Essex, UK). A drop of 1 mg/mL sample solution was left for 90 seconds on top of the grid and the excess solution was removed using filter paper. A drop of contrast solution was then placed on the grid and left for 90 seconds. The excess solution was removed with filter paper leaving a thin layer of solution and the grid was allowed to fully dry in air before analysis.

*Dynamic light scattering:* The measurements were performed using a Zetasizer Nano ZS instrument (Malvern Instrument Ltd., U.K.) equipped with a solid state laser ($\lambda$ = 633 nm), disposable cuvettes with an optical path of 10 mm were used for the measurements.

*Atomic force microscopy:* Images were acquired at 25˚C in water using a Molecular Force Probe 3D AFM (MFP-3D, Asylum Research, Santa Barbara, CA) and a silicon nitride cantilever (model NP-S10 D, Bruker) with a nominal spring constant, tip radius, tip height and resonance frequency of 0.06 N/m, 10 nm, 2.5-8.0 μm and 18 kHz, respectively. PGMMA films were grown on glass slide cover slips (synthesis has been omitted), after which they were fixed to the bottom of a petri dish. After fully drying the samples were immersed in water for 1 hour and subsequently imaged in contact mode at a scan rate of 0.5 Hz.

### *1.8.3 X-ray Diffraction (XRD)*

The main focus of this PhD project was the development of crystalline $TiO_2$ nanoparticles, specifically targeting the development of an anatase crystalline phase that is considered beneficial to maximize the oxidative photoactivity of the resulting materials. An essential tool for the characterisation of nanoparticles is therefore the analysis of crystallinity, which is generally performed through XRD (results can be seen in Chapter 2.3.5). X-rays can be elastically scattered by atoms, an effect primarily produced by the external electrons (the electron shell); the scattered photons may be seen as secondary waves (see Figure 1.8.3-1). In an amorphous material (lacking long-range organisation) the secondary waves interfere both constructively and destructively in a random fashion therefore there is no observable preferential scattering direction. A different situation is presented in materials characterized by the presence of long-range order, e.g. in crystals: since the wavelength of X-rays is comparable to the spacing between the planes of a crystal (1-100 Å), whilst yet most of the scattered X-rays interfere destructively, there will also be areas in which they may interfere constructively creating what is known as a diffraction pattern; Bragg's law is generally used to link the angle(s) of incidence Θ (angle between the direction of the light beam and the director of a crystalline plane) for which a constructive interference can be observed, to the features of the crystal and of the measuring system[3] (Equation 1.8.3-1).

$$2d\sin\theta = n\lambda$$

**Equation 1.8.3-1** Bragg's law where d is the spacing between the diffracting crystal planes, θ is the angle of the incoming X-rays, n is an integer and λ is the wavelength of the incoming beam.

Therefore by knowing the wavelength of the incoming radiation and the angle of the reflected radiation (which is specular to the incidence angle), the spacing *d* between diffracting planes can be determined. Since *d* is unique for each crystalline phase, XRD allows the absolute assignment of the crystalline phase(s) present in a certain material.

With crystalline domains sized less than 100-200 nm, it is also possible to use XRD to calculate the crystallite size: in a diffraction scan, the peaks are characterized by a finite width, which is inversely proportional to the size of the crystallites. The Scherrer equation has been developed to quantify this effect[4] (Equation 1.8.3-2), and can therefore be used to calculate the average crystallite size β of a sample.

$$\tau = {}^{K\lambda}/_{\beta cos\theta}$$

**Equation 1.8.3-2** Scherrer equation where τ is the average size of the crystal domain, K is the shape factor (also known as the Scherrer constant) typically being 0.9 but may differ depending on the actual shape of the crystallite, λ is the wavelength of the incident X-rays, β is the line broadening (full width half maximum, FWHM) of the peak and θ is the Bragg angle.

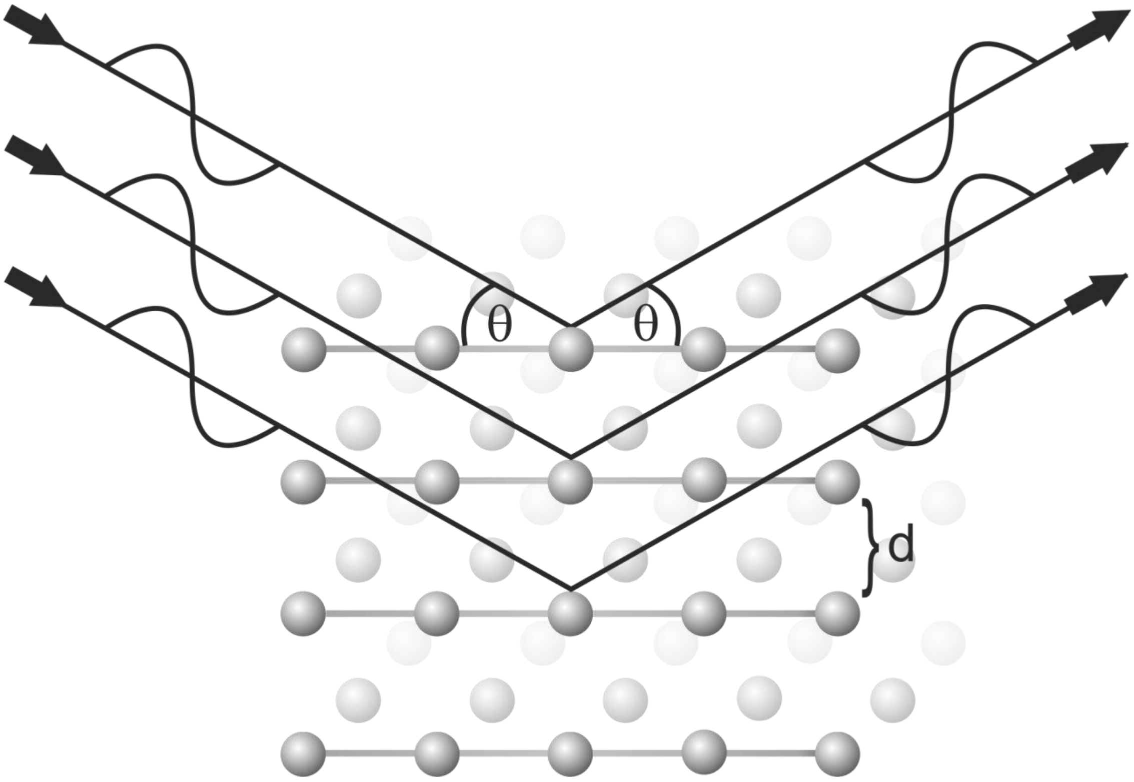

**Figure 1.8.3-1** Schematic representation of the scattering of X-rays from the electron shell of atoms in a primitive cubic crystal.

It is important to note that Scherrer analysis provides a minimum value to the size of a crystalline material; whenever the crystals are polydisperse, or above all in the presence of crystal aggregates, the size derived from the Scherrer equation will be that of the smallest components. For example, in Chapter 2 the Scherrer analysis of $TiO_2$ nanoparticles synthesised through the non-aqueous process showed that, although the overall size of the nanoparticles was in the range of 8-10 nm (via DLS), they were composed of smaller ~3 nm crystalline centres that aggregated during the process to form larger nanoparticles.

### *1.8.4 Dynamic Light Scattering*

DLS was developed as a technique to measure the size of solid nanoparticles in suspension and has also been used to investigate polymer solutions. The technique relies on the time-dependant fluctuation in the intensity of the light scattered at a fixed angle; the fluctuations in intensity are caused by fluctuations in the concentration of the scattering particles, owing to the random nature of the Brownian motion of objects (nanoparticles) dispersed in a fluid (Figure 1.8.4-1).

This phenomenon typically applies to sub-micron objects, typically referred to as colloidal objects: at a given temperature, each body is characterized by a defined value of thermal energy (only proportional to $k_B$T); by expressing this as kinetic energy, it follows that there exists an inverse relationship between mass and the square of the object velocity, hence an object with small dimensions, by virtue of its small mass, would also move with high speed. As a side result, below a certain size the speed of (random) diffusional motion allows to effectively reduce the effect of gravity, which is the reason of the stability of colloidal dispersions against sedimentation.

It is generally difficult to measure the real speed of a particle moving randomly, while it is considerably easier to evaluate its overall displacement as a function of time; the displacement is not to be confused with the distance covered and it identifies with it only in the case of motion along a line. In a pure random motion, the relationship between average displacement and time is quadratic ($2\overline{X^2} = Dt$) and the proportionality constant (*D*) is known as the translational diffusion coefficient and is a measure of the effective speed of a colloid. The Stokes-Einstein equation allows to estimate the hydrodynamic radius ($R_H$) of a colloidal object from its diffusion coefficient knowing the viscosity (η) and the temperature (T) of the solution (Equation 1.8.4-1)[5].

$$R_H = {}^{k_B T}\!/_{3\pi\eta D}$$

**Equation 1.8.4-1** Stokes-Einstein equation where D is the translational diffusion coefficient, kB is Boltzmann's constant and $R_H$ is the hydrodynamic radius of the particle.

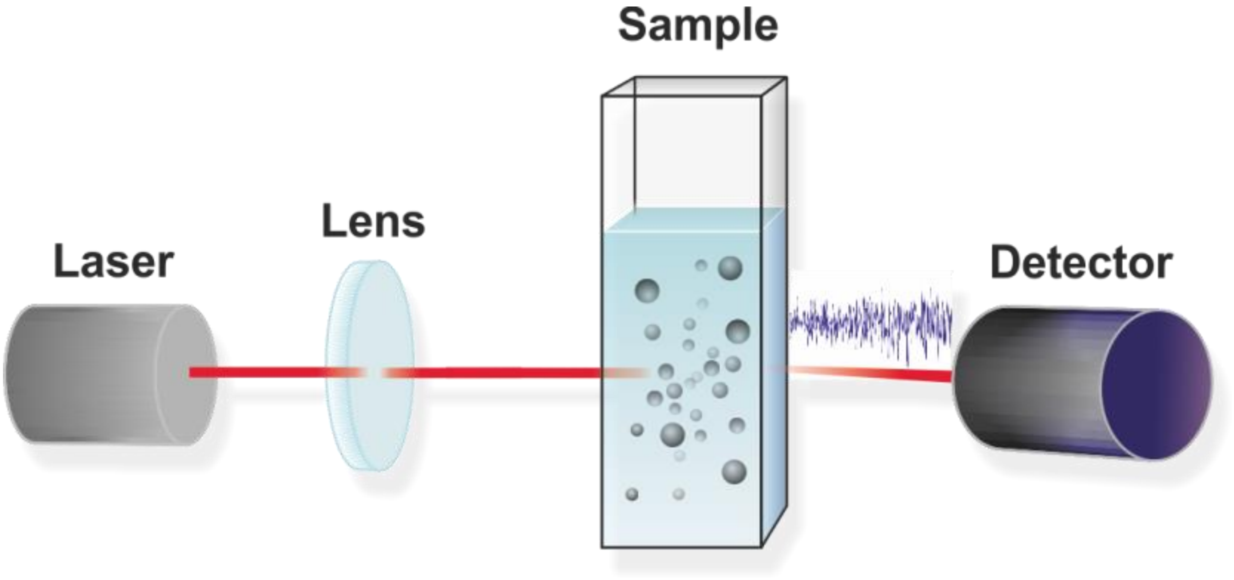

**Figure 1.8.4-1** General representation of a dynamic light scattering setup. A light source generates a beam, which is focused in a small volume of a sample. The intensity of the radiation scattered at a given angle is recorded as a function of time, providing an apparently noisy signal that contains all the information related to the diffusion properties of the dispersed materials.

The problem is therefore to measure the diffusion coefficients of colloidal particles. The solution offered by DLS is based on the fact that, by measuring the fluctuations in the concentration of particles of a given volume of a colloidal dispersion, one can gather information about their size (the larger, the slower they move, the slower the fluctuations). In particular, using the intensity of the scattered light as a measure of the particle concentration, it is possible to create a correlation function G(τ) that provides a quantitative measure of the persistence of a particle in a certain volume (Figure 1.8.4-2 *insert*) (Equation 1.8.4-2)[6].

$$G(\tau) = \int I(t) * I(t+\tau)dt$$

**Equation 1.8.4-2** Where I is the intensity of the scattered light, t is the time and τ is the time difference of the correlator.

There are a number of models used to fit the correlation function to generate a distribution of diffusion coefficients and thus calculate the size distribution of the particles in solution. Typically, the correlation function is fitted as an exponential decaying function of the correlator time delay τ; for a monodisperse sample the correlation function may be fit with a single exponential function (Equation 1.8.4-3 a)[6].

$$a) \quad G(\tau) = A[1 + Bexp(-2\Gamma\tau)]$$

$$b) \quad \Gamma = Dq^2$$

$$c) \quad q = {}^{4\pi n}/_{\lambda_o} \ \sin({}^{\theta}/_{2})$$

**Equation 1.8.4-3** *a)* The correlation function can be fit as single exponential decaying function of the time delay where A is the baseline of the correlation function and B is the intercept of the correlation function. *b)* The main time-independent parameter gathered through this fitting is **Γ**, which is the decay rate of the correlation function and it is directly (linearly) linked to the diffusion coefficient of the colloidal objects. *c)* The parameter q linking the diffusion coefficient to the decay rate depends on the experimental conditions, i.e. the refractive index *n* of the dispersant, the wavelength $\lambda_o$ of the laser and the scattering angle $\theta$ of the laser.

For polydisperse samples the correlation function is often approximated with a multiple exponential function (Equation 1.8.4-4) which can be resolved using cumulant or CONTIN analysis[6].

$$a)\qquad G(\tau) = A[1 + Bg_1(\tau)^2]$$

$$b)\qquad g_1(q;\tau) = \sum_{i=1}^{n} G_i(\Gamma_i)e^{-\Gamma_i\tau} = \int G\,(\Gamma)e^{-\Gamma\tau}d\Gamma$$

**Equation 1.8.4-4** The correlation function $\boldsymbol{G(\tau)}$ can be fit as a multiple exponential decaying function of the time delay; $g_1(\tau)$ is the sum of all the exponential decays present in the correlation function.

Based on cumulant analysis theory, an average decay rate ($\bar{\Gamma}$) may be calculated (Equations 1.8.4-5 a and b) along with a polydispersity index (PDI) of the sample (Equation 1.8.4-5 c). It is worth mentioning that parameters beyond $\mu_3$ are often neglected in order not to over-determine the problem. Using Equation 1.8.4-5 b, $\bar{\Gamma}$ can be converted into an average diffusion coefficient which can in turn be related to an average hydrodynamic radius ($R_h$) via the Stoke-Einstein equation (Equation 1.8.4-1). In summary, an intensity average size and a PDI are obtained through cumulant analysis and a Gaussian distribution can be constructed assuming a single species is present in solution.

$$a)\qquad g_1(q,\tau) = e^{-\bar{\Gamma}\tau}\left(1 + \frac{\mu_2}{2!}\tau^2 - \frac{\mu_3}{3!}\tau^3 + \cdots\right)$$

$$b)\qquad \bar{\Gamma} = q^2 D_z$$

$$c)\qquad PDI = {}^{\mu_2}\!/_{\bar{\Gamma}^2}$$

**Equation 1.8.4-5** The average decay rate can be calculated through *a)* and *b)* where $\mu_2$ is the expected value. *c)* is the PDI of the sample (often referred to as second order PDI since it is calculated on the second parameter of the series expansion).

Size distributions of polydisperse samples can be obtained through CONTIN analysis. CONTIN uses an inverse Laplace to transform a correlation function depending on time (τ) to a function of the decay rate (Γ) (Equation 1.8.4-6). From a decay rate distribution, an intensity size distribution can be constructed after converting Γ to D (Equation 1.8.4-3 b) and D to $R_h$ (Equation 1.8.4-1).

$$G(\Gamma) = L^{-1}[g^{-1}(\tau)]$$

**Equation 1.8.4-6** Inverse Laplace in order to transform a time dependant correlation function to one that depends on the average decay rate.

Figure 1.8.4-2 shows a typical size distribution of a monodisperse sample of $TiO_2$ nanoparticles synthesised for this project (see chapter 2) with the correlation function shown inset.

DLS has been implemented for the size analysis of a wide range of colloidal systems with relatively accurate results. However, there are a number of drawbacks when using DLS. Firstly, the average sizes obtained from measurements are actually hydrodynamic sizes, which take into account the thickness of the layer of solvent molecules, which diffuse together with the particles. Further extrapolations are needed to calculate the size of just the particle[7].

Secondly, DLS analysis is based on the presumption that particles are perfect hard spheres[8]. As a perfect hard sphere is near enough impossible to attain, problems can arise in the interpretation of the results if the sample being analysed has a permanent non-spherical shape or deforms while diffusing.

An example of the possible development of non-spherical morphologies is shown in Figure 1.8.4-3. Two block copolymers composed of poly(propylene sulphide) and poly(glycerol monomethacrylate) (PPS-PGMMA) have been dispersed in an aqueous solution. Upon dissolution the polymer arranges itself into micelle like structures where the polymer chains organise themselves so that the hydrophilic portion of the polymer (PGMMA) is exposed to the aqueous solution whereas the hydrophobic PPS section is directed towards the centre of the micelle away from the water[9]. Typically micelles exist as spherical constructs (Figure 1.8.4-3 C) but depending on the ratio of the hydrophilic section to hydrophobic section they may adopt different morphologies such as worm like micelles (Figure 1.8.4-3 B).

The average sizes of the polymer constructs by DLS, whilst varying the hydrophilic/hydrophobic ratio, can be seen in Figure 1.8.4-3 A with the corresponding TEM images for two of the samples also shown. $PPS_{39}$-$PGMMA_{75}$ dispersed in an aqueous solution gives an average hydrodynamic radius of 45 nm and the corresponding TEM image (Figure 1.8.4-3 C) shows that the polymer adopts a classical spherical micelle shape (the reasons as to why TEM shows a smaller size for the micelles is given in chapter 1.8.5). The size and shape where also confirmed by atomic force microscopy (AFM), this technique is described later in chapter 1.8.6. By increasing the hydrophobic content of the polymer to $PPS_{30}$-$PGMMA_{53}$ the chains rearrange to give worm like micelles due to their lower surface/volume ratio[10]. However, DLS does not take into account the fact that the polymer is not in a spherical conformation and gives an average hydrodynamic diameter of 200 nm, which if only DLS was used would lead the user to conclude that their system contains spherical polymer aggregates with a diameter of 200 nm. Therefore here is a clear example as to why techniques for the analysis of nanoconstructs need to be used in conjunction to get an overall picture of what is occurring within the system.

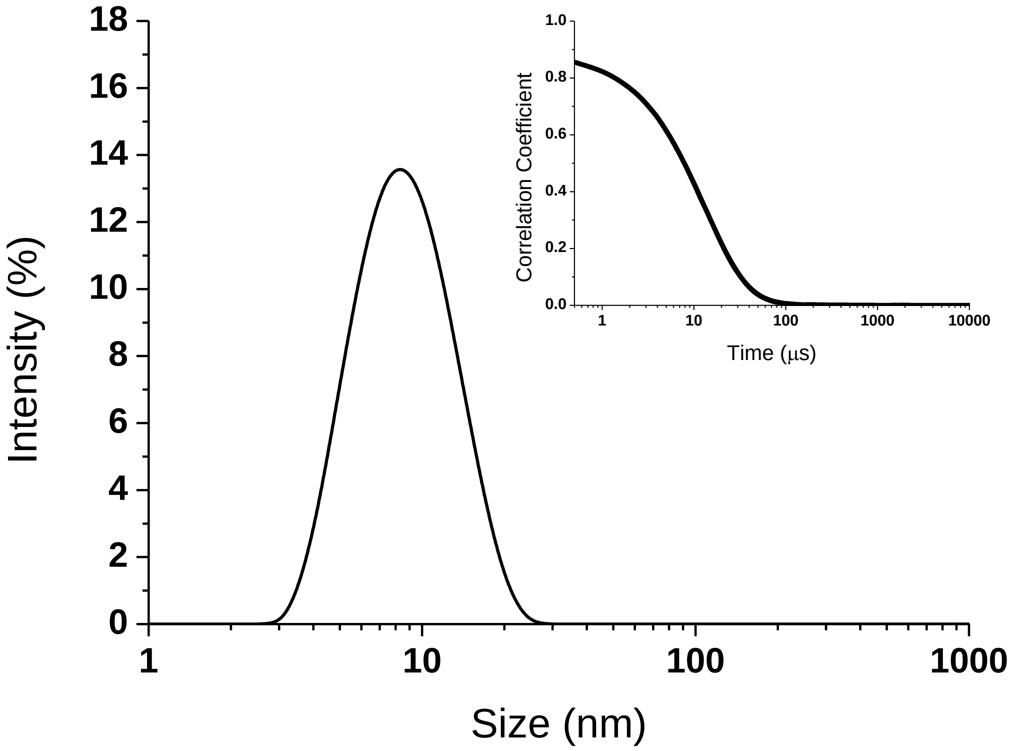

**Figure 1.8.4-2** A typical size distribution of monodisperse $TiO_2$ nanoparticles obtained by DLS. (*inset*) The correlation function of the scattering of the laser associated with the size distribution.

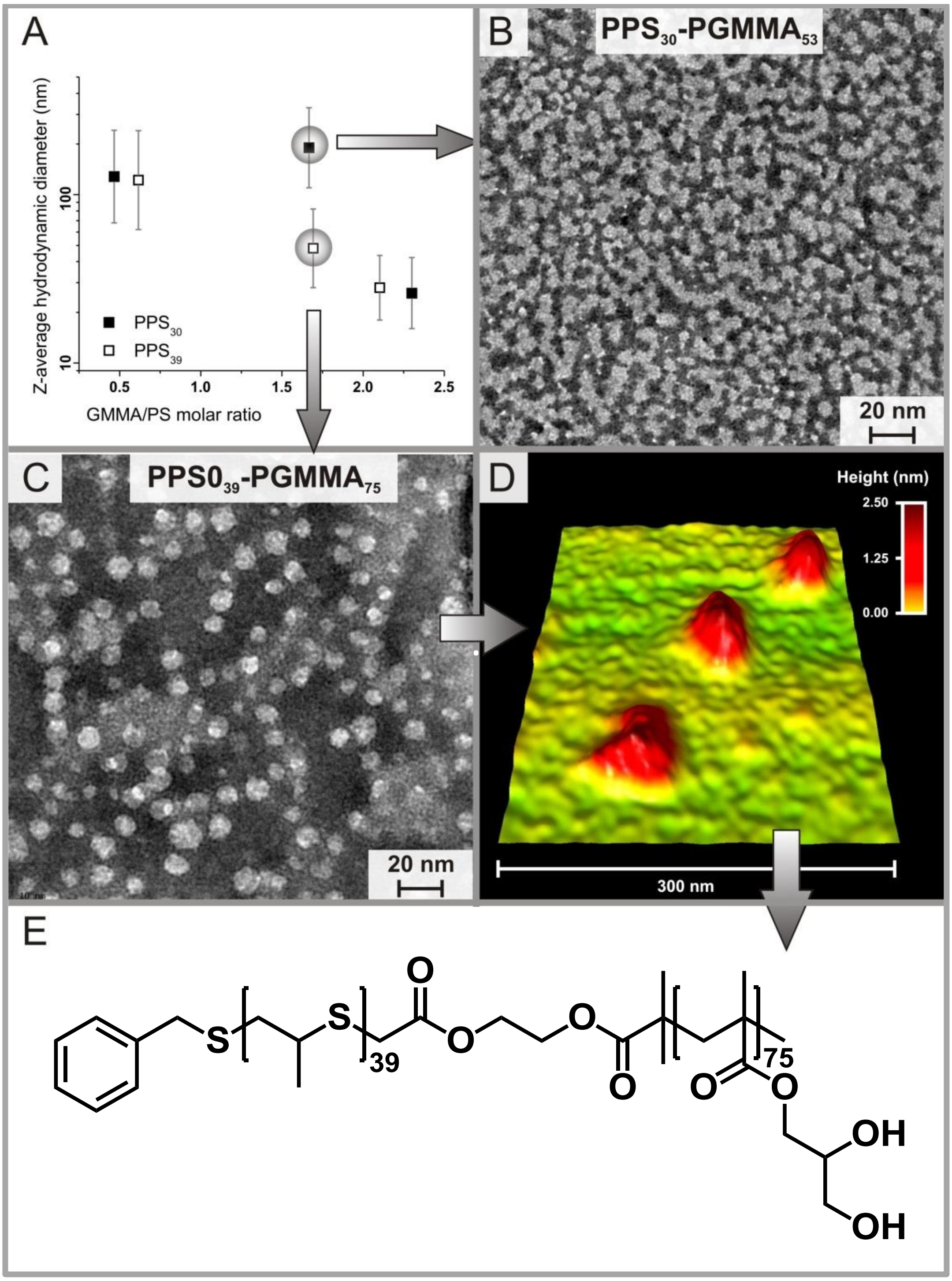

**Figure 1.8.4-3** ***A:*** Z-average size (from DLS measurements) for different PPS-PGMMA copolymers with different PPS/GMMA ratios and two different PPS degrees of polymerization. The bars represent the width at half height of the peaks. ***B:*** negative staining TEM picture for PPS$_{30}$-PGMMA$_{53}$, showing the presence of irregular elongated structures (probably worm-like micelles). ***C:*** negative staining TEM picture for PPS$_{39}$-PGMMA$_{75}$, showing the presence of spherical structures (spherical micelles). ***D:*** AFM image of PPS$_{39}$-PGMMA$_{75}$ aggregates deposited on mica. See also Supplementary Information, Figures S6 and S7. ***E:*** Structure of a PPS-PGMMA polymer chain. Polymer synthesis, DLS and AFM measurements were all performed by Dr. Cong-Duan Vo. Results published in Macromolecular and Rapid Communications[1].

### *1.8.5 Transmission Electron Microscopy*

The maximum resolution achievable on an imaging device (e.g. a microscope) is limited by the wavelength of the electromagnetic radiation employed. In microscopes, the Abbe equation $d = \frac{\lambda}{2n \sin \vartheta}$ links the minimum distance observable to the wavelength through the numerical aperture ($n$sinθ (refractive index*angle of incidence)) of a lens, which is often close to 1, causing the resolution to be around half of the wavelength[11]. For typical light microscopes this diffraction limit to the achievable resolution is at best 200 nm.

For the analysis of nanoscale structures, Knoll and Ruska were the first to utilise the wave-like properties of electrons to construct what is now known as a TEM[12]. With the wavelength of electrons typically being around 1-10 pm, depending on the operating power of the microscope, theoretically the resolution of TEM is on a sub atomic scale. However in reality the best resolution obtained to date is around 0.1 nm, mostly due to physical defects and aberrations within the lenses[13].

Briefly, in a TEM a beam of electrons is created at the emission source, which may be composed of tungsten or lanthanum hexaboride ($LaB_6$). The beam then passes through an anode in order to accelerate the electrons which then continue on through the condenser lens in order to focus the beam through an ultrathin sample (< 100 nm thick). The beam then passes through the objective and intermediate lenses which refocus the beam once it has interacted with the sample. Finally the beam passes through the projector lens which expands the beam onto either a photographic plate or, more commonly nowadays, onto a charge coupled device (CCD) camera allowing real time observation of the sample (Figure 1.8.5-1). The image is created by the scattering of the electron beam as it passes through a sample, therefore denser areas would provide lower electron transmittance[14].

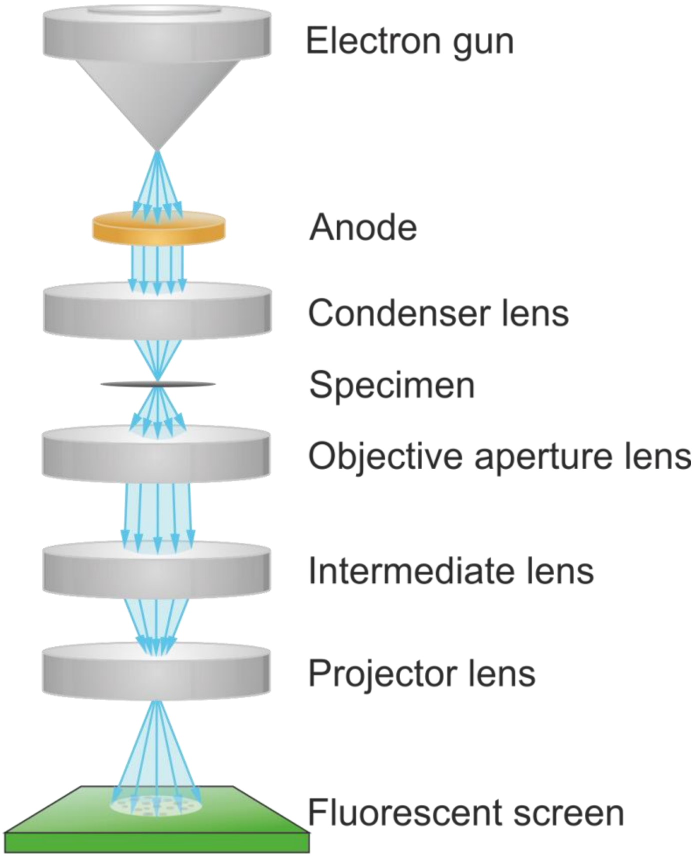

**Figure 1.8.5-1** Schematic representation of a transmission electron microscope.

This technique has been traditionally used to image materials with significant scattering also in thin samples, i.e. materials such as metals or ceramics characterized by a high density of ‘opaque’ atoms (= with a high number of electrons). However, now also biological samples can be imaged through the use of appropriate contrast agents and the fixation of the material; even more advanced is the use of the low temperature cryo-TEM where the sample is frozen (avoiding artefacts due to the evaporation of water) and vitreous ice acts as a contrast agent in the sample[15]. Organic polymers can also be imaged *via* TEM, e.g. to visualize the structures produced by self-assembly in water; most often this is obtained by negatively staining the samples with a heavy metal salt such as uranyl acetate, ammonium molybdate or, as for Figures 1.8.4-3 and 1.8.5-2, sodium phosphotungstate[16]. For example the strucutres shown in Figure 1.8.5-2 are formed by block copolymers of poly(glycerol monomethacrylate) – *block* - poly(dimethylsiloxane) – *block* - poly(glycerol monomethacrylate) (SilGMMA) stained with a sodium phosphotungstate contrast solution (2% wt.).

The negative stains allowed the visualisation of the polymer aggregates *via* staining the areas of the grid around the polymer therefore allowing to recognize the structure formed by polymers as the areas with the highest intensity of transmitted light . As with the PPS-PGMMA polymers analysed in Chapter 1.8.4, as the hydrophobic content of the SilGMMA (where the poly(dimethyl siloxane) (PDMS) block is the hydrophobic portion of the polymer) increases the morphology of the aggregates changes from a classical spherical micelle shape (SilGMMA5 and 6) to a worm like micelle one (SilGMMA1 and 3).

As well as determining the morphology of nanoconstructs TEM can also be used as an analytical tool for determining the composition and morphology of the materials being studied. The scattering of the electrons in TEM can also allow the identification of the crystalline phase of specific materials in the sample, since as seen for X-rays also electrons scatter elastically creating secondary waves which can interfere either constructively or destructively. In a crystalline sample the scattering can therefore produce a diffraction pattern which can be mapped to calculate the crystal planes in the sample[17]. Figure 2.3.5-1 (*left*) (Chapter 2.3.5) shows a high resolution TEM (HRTEM) image of $TiO_2$ nanoparticles. It can be seen that there is a regular pattern of contrasting light and dark areas present in the HRTEM image of the nanoparticles: what is being observed here are the crystal planes of the nanoparticles themselves. The distance between the spacing was measured to be 3.2Å which correlates with the 101 plane found in anatase confirming the results obtained by XRD.

Although not used in this research, TEM can also permit the determination of the elemental composition of a material. When electrons scatter off a material they can do so either elastically or inelastically, depending on whether they preserve or degrade their initial energy. The energy loss is generally caused by the ionization of the atoms the electrons come into contact with and, as the ionisation energy of each element is unique, it is possible to map the atomic composition of a sample through what is commonly referred to as electron energy loss spectroscopy (EELS)[18].

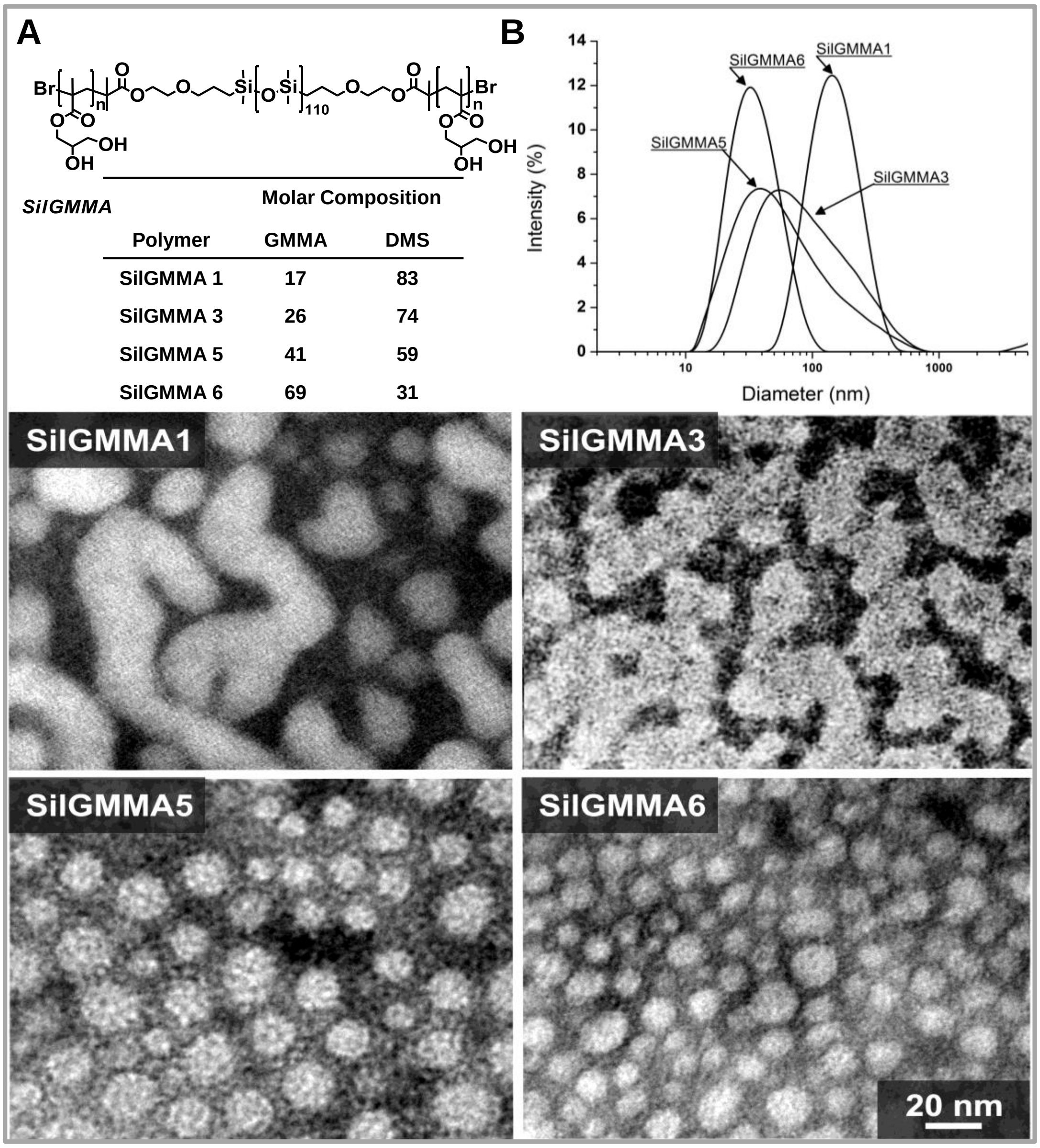

| | Molar Composition | |
|---|---|---|
| **Polymer** | **GMMA** | **DMS** |
| SilGMMA 1 | 17 | 83 |
| SilGMMA 3 | 26 | 74 |
| SilGMMA 5 | 41 | 59 |
| SilGMMA 6 | 69 | 31 |

**Figure 1.8.5-2** ***A*****:** Structure of a SilGMMA polymer chain, during this study the hydrophobic PDMS chain length was kept constant at 110 monomer units and the GMMA chain length was changed to vary the hydrophobic/hydrophilic ratio of the block copolymer. ***B*****:** DLS curves of SilGMMA dispersion in water with the corresponding TEM pictures shown below. Polymer synthesis and DLS measurements were performed by Dr. Ghislaine Robert-Nicoud.

When TEM is used for organic or biological samples there is one main drawback. Due to the use of electrons as the source of electromagnetic radiation, the TEM chamber must be under a very high vacuum; this is due to the fact that any gas molecules in the chamber will interact and scatter the electrons before reaching the sample thus knocking them out of alignment which will result in a major decrease in focusing and resolution capabilities. For inorganic materials the need to be under high vacuum is not a great problem as structure changes during preparation will be kept to a minimum[19]. However when using organic samples, as with the samples in Figures 1.8.4-3 and 1.8.5-2, the sample preparation and imaging treatment may give rise to artefacts which the user has to be aware of. The polymers used in the afore mentioned figures are prepared in an aqueous solution and the hydrophilic portion will be fully swollen by water, however upon drying the water will evacuate the hydrophilic parts causing an apparent shrinkage in the overall size of the micelles. Therefore by TEM micelles generally appear to have a smaller size than e.g. when measured by DLS in a hydrated state.

### *1.8.6 Atomic Force Microscopy*

In 1986 Binnig, Quate and Gerber published the first results on their development of what is now commonly referred to as an AFM[20]. Originally developed for the imaging of samples by “feeling” the surface with a mechanical probe, this technique has now been developed for measuring and manipulating samples at the nanoscale, making AFM one of the foremost tools for nano scale characterization. Quite simply an AFM consists of a cantilever with a sharp tip which has a radius typically in the order of a few tens nanometers; a laser is reflected off the top of the cantilever towards an array of photodiode detectors, therefore any change in the position of the reflected laser spot can be monitored (Figure 1.8.6-1).

As the tip is brought in contact with the surface, attractive or repulsive forces (electrostatic, hydrophobic/philic interactions etc.) between the tip and the sample cause a deflection of the cantilever which in turn causes a deflection of the laser which is monitored on the photodiode array. Clearly, to image a sample the tip must first experience some interaction with the surface; therefore, depending on the material being examined, the tip is brought into contact with the surface at a height to give the desired amount of deflection. The tip is then dragged along the surface of the material and as it does so the deflection of the tip is kept constant, therefore any increases or decreases in topology will result in the cantilever moving up or down respectively, this is known as contact mode AFM. As a result the laser spot reflected off the top of the cantilever onto the photodiode array will change position allowing the topology of the material to be visualised[21]. As well as contact mode, which keeps the tip static, the tip can also be oscillated at its resonant frequency just above (1-10nm) the sample so as not to come into direct contact with it, this is known as tapping mode. Van der Waal's forces from the surface of the sample interact with the tip thus decreasing the resonance frequency. The distance between the tip and the sample is then adjusted to return to the original resonance frequency and the change in height of the tip is monitored as mentioned in contact mode[22].

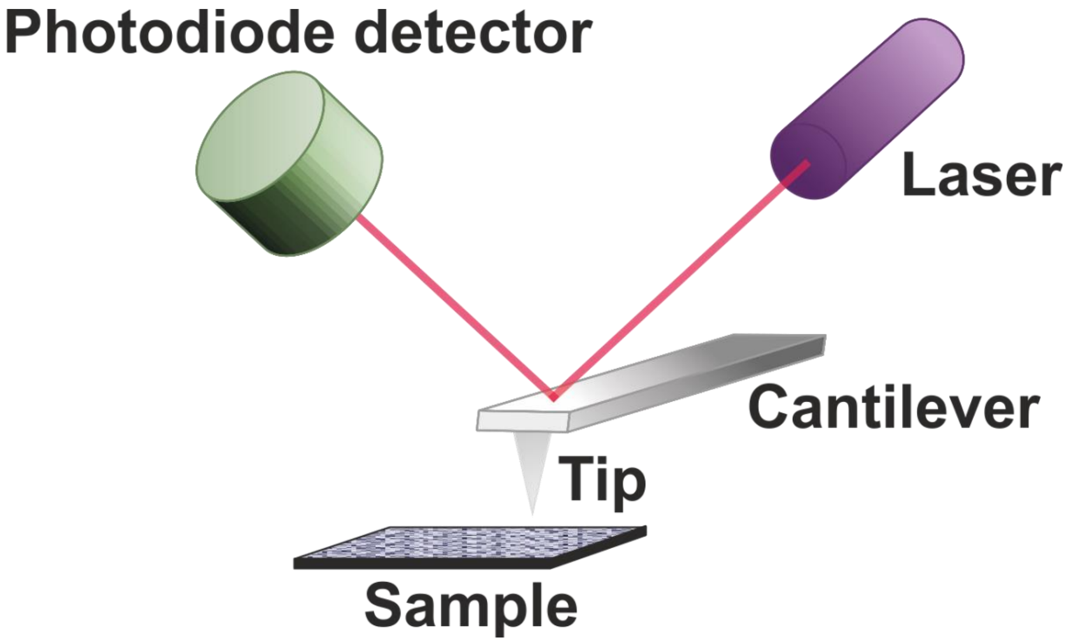

**Figure 1.8.6-1** Schematic representation of an atomic force microscope.

Typical AFM images can be seen in Figure 1.8.6-2 A and B: a glass disk (A) was coated with a layer of poly(glycerol monomethacrylate) (B) grown via a surface-initiated mechanism. A first major advantage of AFM over other common imaging techniques is the ability to perform analyses in dry or, as in this case, in aqueous conditions. Secondly, the images can be used to measure quantitatively the size of surface features: for example Figure 1.8.6-2 C shows the height profile obtained following the surface relief along an imaginary line (black dashed line in A and B) on the glass alone (white line in C) or with a polymer coating (red line in C). From the full 3D image, the roughness of the surface can be calculated; in this case the polymer coated surface showed a roughness of 23.6 nm which, although itself is smooth, has increased from that of plain glass which was 2.6 nm (Figure 1.8.6-2 A).

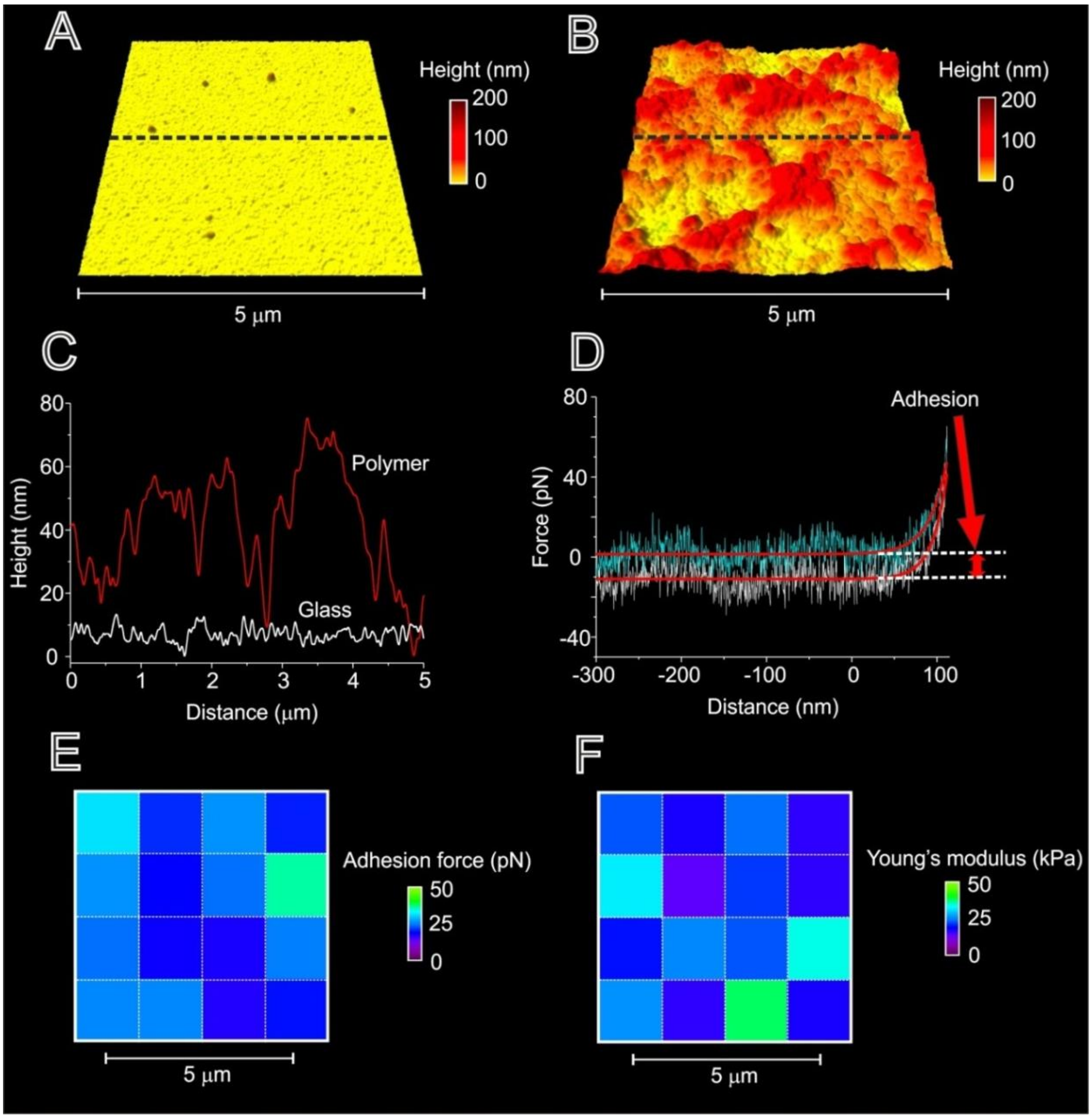

**Figure 1.8.6-2** ***A:*** AFM image of piranha treated glass, the dashed line is the area taken to provide the height profile in image C. ***B:*** AFM image of a PGMMA film grown on a glass disk, the dashed line is the area taken to provide the height profile in image C. ***C:*** Height profiles of piranha treated glass (white) and polymer film (red). ***D:*** Nanoindentation curves of the polymer film showing the indentation (blue) and retraction (white) curves. The difference in force between the indentation and retraction arises due to adhesion forces between the tip and the sample. The slope of the curves, either indentation or retraction can be fit with the Hertz model to derive the Young's modulus of the sample. ***E:*** Adesion force map of a PGMMA film grown on a glass disk. ***F:*** Young's modulus force map of a PGMMA film grown on a glass disk.

A third interesting point of AFM is the possibility to extract also chemical information, for example measuring the adhesion force from the tip and the sample. When an increasing load is placed on the tip, this will be forced into the sample at a constant rate and it will be possible to measure the deflection of the cantilever/the displacement of the tip as a function of the load. The tip can then be retracted from the sample at the same rate, to give a second force-displacement graph. Examples of the two curves are shown in Figure 1.8.6-2 D. As can be seen the retraction curve (white curve) does not overlap with the indentation curve (blue curve) and this is possibly the sign that there is an interaction between the tip and the sample; the adhesion force is the difference between the force recorded during indentation and retraction at the first contact point of the tip with the sample[23]. It is then possible to create maps of the adhesion force by repeating these measurements at regularly space locations; Figure 1.8.6-2 E shows the adhesion force map associated with the area of the PGMMA film showed in B, resulting in an average adhesion force of 19.5 ± 4.5 pN that is considerably lower than then average adhesion force of 40.7 ± 1.1 pN for the glass disks. The tip used for this analysis was composed of silicon nitride ($Si_3N_4$) which has a hydrophilic surface covered by silanol groups. Since both the hydrophilic polymer PGMMA and glass offer a high density of OH groups, it would be reasonable to expect a similar adhesion, maybe even higher for the polymer due to the possibility of deeper penetration during the indentation experiments. However, since $Si_3N_4$ has an isoelectric point of 9, while that of glass is typically below 7, at pH 7 the tip and the substrate will be oppositely charged; therefore the increase in adhesion is probably to ascribe to electrostatic attraction[24].

Using AFM in nanoindentation, along with adhesion forces it is also possible to calculate the stiffness (Young's modulus) of a substrate. As the tip approaches the surface the deflection of the laser is kept constant; however, as the tip touches and indents the surface, the laser is deflected giving rise to a typical indentation curve (see figure 1.8.6-2 D). From the shape of this deflection the stiffness of the substrate can be calculated. There are a number of models used to calculate the stiffness of a substrate; in AFM indentation the most common one is the Hertz model (Equation 1.8.6-1)[25].

$$F = {}^{4E}/_{3(1-\nu^2)}\sqrt{R}\delta^{1.5}$$

**Equation 1.8.6-1** The Hertz equation where F is the force applied, E is the Young's modulus, ν is Poisson's ratio, R is the radius of the tip and δ is the indentation depth.

The Hertz model, however, is not without drawbacks. Most importantly, it does not take into account the adhesion forces between the tip and the sample. This problem does not arise in indentation at a macroscopic scale as *1)* adhesion between the indenter and sample is weak in comparison to the mechanical loads used they are basically insignificant; *2)* with a macroscopic indenter the surface area of the tip is well defined, as it is visible to the naked eye and much easier to measure. A number of other more accurate models can be used for the fitting of indentation data, for example the Johnson-Kendall-Roberts (JKR) model and the Derjaguin-Muller-Toporov (DMT) one, which employ the surface energy of a material to take into account interaction contributions respectively only in the area of tip-sample contact or also in neighbouring, non-contact areas[26, 27]. Nevertheless although the Hertz model does not provide a wholly accurate mechanical description, due to its simplicity it is still the most widely used to fit nanoindentation data.

### 1.8.7 Appendix References

1. Vo, C.-D.; Cadman, C. J.; Donno, R.; Goos, J. A. C. M.; Tirelli, N., Combination of Episulfide Ring-Opening Polymerization With ATRP for the Preparation of Amphiphilic Block Copolymers. *Macromol. Rap. Comm.* **2013,** 34, (2), 156-162.

2. Robert-Nicoud, G.; Evans, R.; Vo, C.-D.; Cadman, C. J.; Tirelli, N., Synthesis, self-assembly and (absence of) protein interactions of poly(glycerol methacrylate)/silicone macro-amphiphiles. *Polym. Chem.* **2013,** 4, 3458-3470.

3. Bragg, W. H., The reflection of X-rays by crystals. *Phys. Z.* **1913,** 14, 472-473.

4. Patterson, A. L., The Scherrer formula for x-ray particle size determination. *Phys. Rev.* **1939,** 56, (10), 978-982.

5. Schurr, J. M.; Schmitz, K. S., Dynamic light scattering studies of biopolymers: Effects of chargs, shape and flexibility. *Annu. Rev. Phys. Chem.* **1986,** 37, 271-305.

6. Ruf, H.; Georgalis, Y.; Grell, E., Dynamic laser-light scattering to determine size distributions of vesicles. *Method Enzymol.* **1989,** 172, 364-390.

7. Pecora, R., Dynamic light scattering measurement of nanometer particles in liquids. *J. Nanopart. Res.* **2000,** 2, (2), 123-131.

8. Segre, P. N.; Behrend, O. P.; Pusey, P. N., Short time Brownian motion in colloidal suspensions: Experiment and simulation. *Phys. Rev. E* **1995,** 52, (5), 5070-5083.

9. Israelachvili, J. N.; Mitchell, D. J.; Ninham, B. W., Theory of self assembly of hydrocarbon amphiphiles into micelles and bilayers. *J. Chem. Soc. Farad. T. 2* **1976,** 72, 1525-1568.

10. Candau, S. J.; Oda, R., Linear viscoelasticity of salt-free wormlike micellar solutions. *Colloid Surf. A-Physicochem. Eng. Asp.* **2001,** 183, 5-14.

11. Scherzer, O., The theoretical resolution limit of the electron microscope. *J. Appl. Phys.* **1949,** 20, (1), 20-29.

12. Knoll, M.; Ruska, E., The Electron Microscope. *Z. Phys.* **1932,** 78, (5-6), 318-339.

13. Tanaka, N., Present status and future prospects of spherical aberration corrected TEM/STEM for study of nanomaterials. *Sci. Technol. Adv. Mater.* **2008,** 9, (1).

14. Muller, S. A.; Aebi, U.; Engel, A., What transmission electron microscopes can visualize now and in the future. *J. Struct. Biol.* **2008,** 163, (3), 235-245.

15. Dubochet, J.; Adrian, M.; Chang, J. J.; Homo, J. C.; Lepault, J.; McDowall, A. W.; Schultz, P., Cryo-electron microscopy of vitrified specimens. *Q. Rev. Biophys.* **1988,** 21, (2), 129-228.

16. Massover, W. H.; Marsh, P., Unconventional negative stains: Heavy metals are not required for negative staining. *Ultramicroscopy* **1997,** 69, (2), 139-150.

17. Qin, L. C., Electron diffraction from carbon nanotubes. *Rep. Prog. Phys.* **2006,** 69, (10), 2761-2821.

18. Egerton, R. F., Electron energy-loss spectroscopy in the TEM. *Rep. Prog. Phys.* **2009,** 72, (1).

19. Grabar, K. C.; Brown, K. R.; Keating, C. D.; Stranick, S. J.; Tang, S. L.; Natan, M. J., Nanoscale characterization of gold colloid monolayers: A comparison of four techniques. *Anal. Chem.* **1997,** 69, (3), 471-477.

20. Binnig, G.; Quate, C. F.; Gerber, C., Atomic force microscope. *Phys. Rev. Lett.* **1986,** 56, (9), 930-933.

21. Giessibl, F. J., Advances in atomic force microscopy. *Rev. Mod. Phys.* **2003,** 75, (3), 949-983.

22. Garcia, R.; Perez, R., Dynamic atomic force microscopy methods. *Surf. Sci. Rep.* **2002,** 47, (6-8), 197-301.

23. Segeren, L.; Siebum, B.; Karssenberg, F. G.; Van den Berg, J. W. A.; Vancso, G. J., Microparticle adhesion studies by atomic force microscopy. *J. Adhes. Sci. Technol.* **2002,** 16, (7), 793-828.

24. Lewis, J. A., Colloidal processing of ceramics. *J. Am. Ceram. Soc.* **2000,** 83, (10), 2341-2359.

25. Domke, J.; Radmacher, M., Measuring the elastic properties of thin polymer films with the atomic force microscope. *Langmuir* **1998,** 14, (12), 3320-3325.

26. Xu, D. W.; Liechti, K. M.; Ravi-Chandar, K., On the modified Tabor parameter for the JKR-DMT transition in the presence of a liquid meniscus. *J. Colloid Interface Sci.* **2007,** 315, (2), 772-785.

27. Song, J.; Tranchida, D.; Vancso, G. J., Contact mechanics of UV/ozone-treated PDMS by AFM and JKR testing: Mechanical performance from nano- to micrometer length scales. *Macromolecules* **2008,** 41, (18), 6757-6762.

# 2 “Non-aqueous” route to titanium dioxide nanoparticles. Can water really be omitted from the reaction mechanism?

Christopher J. Cadman[a], Andrea Pucci[b], Francesco Cellesi[a], Nicola Tirelli[c,d*]

[a] School of Pharmacy and Pharmaceutical Sciences, University of Manchester, Oxford Road, Manchester, M13 9PT, United Kingdom

[b] Department of Chemistry and Industrial Chemistry, University of Pisa, via Risorgimento 35, 56126, Pisa, Italy

[c] Institute of Inflammation and Repair, University of Manchester, Oxford Road, Manchester, M13 9PT, United Kingdom

[d] School of Materials, University of Manchester, Oxford Road, Manchester, M13 9PT, United Kingdom

[*] to whom correspondence should be addressed:

Prof. Nicola Tirelli, Institute of Inflammation and Repair, University of Manchester, Oxford Road, Manchester, M13 9PT, United Kingdom

Tel: +44 161 275 18 02

Email: Nicola.tirelli@manchester.ac.uk

## Abstract

We here present the rational development of a “non-aqueous” preparative method for inorganic nanoparticles. Non-aqueous routes are supposedly based on the absence of water; here we partially challenge this view, showing that the presence of water (or moisture) is probably necessary and is surely useful to achieve a precise control over the growth/aggregation phenomena leading to titanium dioxide nanoparticles.

In this study, we show how a careful control over process variables allowed to eventually obtain water dispersible anatase nanoparticles with <10 nm size and a ligand-free suface. We have employed three titanium alkoxides with increasingly bulky aliphatic groups ($Ti(O\textit{n}Pr)_4$, $Ti(O\textit{n}Bu)_4$ and $Ti(O^iPr)_4$), studying the generation of nanoparticles in benzyl alcohol as a function of the amount of water and HCl added. Primary (3-4 nm) nanoparticles were rapidly generated at room temperature, and upon heating (80°C) they aggregated in larger secondary nanoparticles. The size of the latter can be precisely controlled through the nature of surface groups (e.g. presence of titanols) and the duration of the thermal treatment; their fractal dimension appeared to be much affected by the acidity of the medium, possibly due to the increase in interpartical repulsion between the positively charged primary particles.

## 2.1 Introduction

Titanium dioxide-based materials have found application in a variety of fields, such as photovoltaics[1], gas sensing[2], surface (window) self-cleaning[3], sun protection[4] and water purification[5], where the use of $TiO_2$ is based on the efficient photo-induced generation of oxidants/free radicals (Reactive Oxygen Species, ROS) at surface sites. Titania also shows favourable properties as a biomaterial: for example, titania-coated materials are known to be beneficial for osteointegration[6], although this has a strong dependency on the surface morphology[7], possibly because of a mechanism of protein adsorption similar to hydroxyapatite[8]. There are, however, also controversial issues in its issues in connection with a biological environment: although titania nanoparticles have a relatively low acute toxicity[9], above all in comparison to other inorganic nanoparticles[10, 11], they do show detrimental effects on cell viability due to increased oxidative stress and thus inflammatory reactions[12], damage to nucleic acids[13] and also to cell membranes[11], the latter two points suggesting the toxicity to be based on both apoptotic and necrotic effects); interestingly, this behavior appears to be more noticeable on tumoral cells[14].

As suggested, since the 1990’s, the oxidative activity of titania nanoparticles and the resulting toxic effects could also be employed as a therapeutic tool[15]: taking advantage of the enhanced production of oxidants under UV (or visible) irradiation, the toxic effects of ROS could be targeted on cells/cell masses that are selectively irradiated, similarly to the photodynamic therapies based on low molecular weight sensitizers, e.g. porphyrins and phthalocyanins[16, 17].

In view of such an application, the synthetic approach to titania nanoparticles should allow to exert control over a number of variables:

a) Crystalline phase: the combination of anatase and rutile has been shown to be more active than the isolated components[18] and indeed commercially available photocatalysts such as Degussa P-25 have a anatase/rutile 3:1 composition [19]. However, anatase is generally reported to be more active than rutile[20], and the differences with mixed-phase photocatalysts can be easily offset by acting on other factors such as size and availability of surface sites[21]. Therefore for seek of simplicity and ease of characterization, preparative methods yielding anatase are probably to favour.

b) Surface chemistry: it is well known that surface modification with chromophoric groups, e.g. with carotenoids[22] or dyes such as alizarin blue[23], allows to extend the sensitivity of the photocatalytic activity towards the visible region of the spectrum (essentially the same as for the dye-sensitized solar cells), which would also allow deeper penetration of the radiation in biological tissues. Additionally, surface functionalization can allow to overcome agglomeration in water, due the isoelectric point of titania (any crystalline form) being too close to neutrality to allow sufficient electrostatic stabilization[24]. Last, the introduction of appropriate surface groups (for example poly(ethylene glycol) (PEG) chains or peptide/proteic groups) is a prerequisite to minimize protein adsorption and allow both a prolonged circulation in body fluids and biological targeting. Ideally, synthetic procedures should therefore easily allow for different forms of surface functionalization, and possibly to accomplish them in a water environment.

c) Size: the photocatalytic activity of $TiO_2$ is directly proportional to the number of free surface sites available, therefore nanoparticles show higher photocatalytic activity than bulk $TiO_2$[25], and smaller particles have a higher efficiency in ROS generation and phototoxicity than larger ones[26]. Additionally, the size of titania particles affects their biodistribution[9] and smaller particles are likely to diffuse faster in interstitial fluids allowing a more homogeneous distribution in a tissue. Ideally, in order to allow also blood-born applications, these particles should show the minimal size necessary to avoid renal filtration, which is in the range of 5-10 nm.

In order to extend the spectrum of nanoparticles employable for photodynamic therapy, in this study we have specifically tackled the minimization of the size of water-dispersible titania nanoparticles; only a limited number of reports exist for the preparation of very small (10-20 nm) naked titania nanoparticles[27, 28], and in no case they have been studied in colloidal dispersion, possibly because of significant agglomeration during their preparation.

Classical preparative techniques have been based on aqueous sol-gel and hydrothermal methods[29], but more recently non-aqueous sol-gel synthetic routes have become more popular[30]. Due to the relatively slow condensation rate between surface groups, such methods offer a better control over average size, crystallinity and surface composition[31]; for example, in aqueous sol-gel processes the particle size can controlled only through the use of relatively large quantities of surfactant[32], which imposes strong limitations the surface composition, while crystallinity is induced *via* calcination[28]. A review by Niederberger and Bilecka provides an in-depth overview on the advantages of non-aqueous sol-gel methods for the production of metal oxide nanoparticles[31,33].

In a previous paper, we have employed a non-aqueous process in benzyl alcohol, where $TiCl_4$ and ethanol *in situ* produce $Ti(Cl)_{4-n}(OEt)_n$ (where n is close to four), whose thermal condensation, at 80˚C, eventually produced anatase nanoparticles with an average particle diameter in the region of 30 nm[34]. The resulting nanoparticles were easily functionalized in a second step with catechols, possibly also bearing PEG chains[35]. In addition to the typical advantages of non-aqueous processes, this “benzyl alcohol method” allows the preparation of ligand-free nanoparticle dispersions in acidic water, due to the simultaneous and rapid occurrence of the hydrolysis of alkoxide surface groups and of the surface protonation, which allows for electrostatic stabilization. It is also worth mentioning that the use of the toxicologically benign benzyl alcohol as a solvent is an additional advantage in the perspective of a clinical use[36]. However, despite the significant advantages of the benzyl alcohol method (chiefly the control over size and surface chemistry), the mechanism of nanoparticle formation and growth is yet rather poorly understood; in particular, a generally unexplained lag time is often observed prior to the appearance of primary crystalline particles[37].

Here, we have worked on the hypothesis that traces of water may strongly influence both the nature of the mechanism and the presence of the lag time; we have therefore modified the synthetic approach so as to enable a higher degree of control over the different phases of growth. In our synthesis the indeterminate starting material has been replaced by $Ti(OR)_4$ where R is either a propyl ($Ti(OPr)_4$), butyl ($Ti(OBu)_4$) or isopropyl ($Ti(O^iPr)_4$) group, and we independently varied amount of HCl (as both a condensation catalyst and a protonating agent) and of water. The titanium alkoxides were chosen to guarantee a clear initial stoichiometry to the titanium centres and to understand the effect of the nature of alkoxy groups on the rate of particle growth. Water was added to clarify the possibility of its direct role in primary particle nucleation and of that of hydroxylated species in secondary particle growth (Scheme 2.1-1).

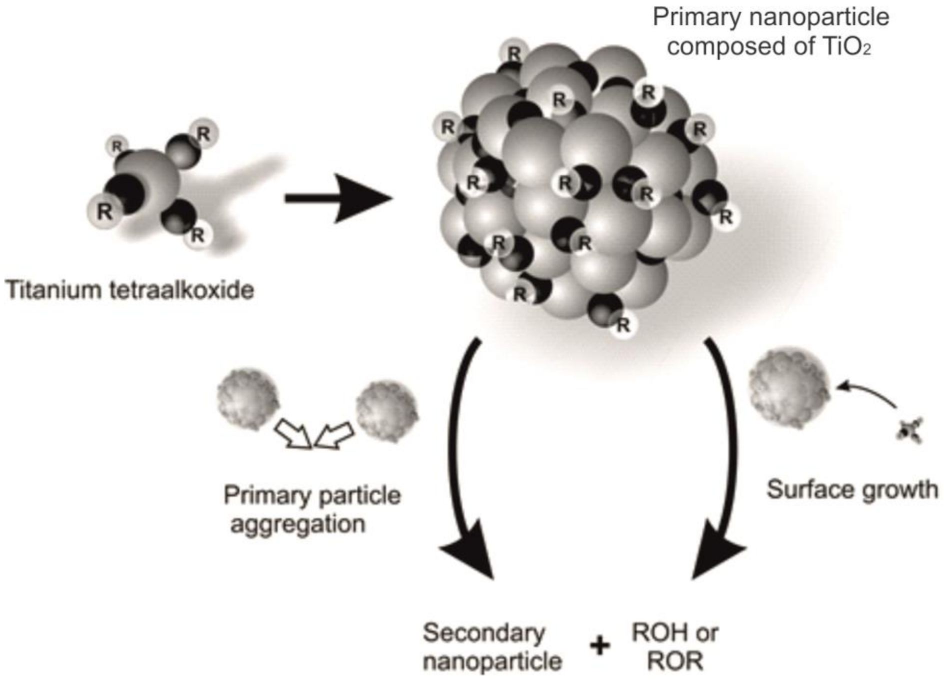

**Scheme 2.1-1** Primary $TiO_2$ nanoparticles are instantly formed upon the addition of $H_2O$ to the titanium alkoxide precursor. Subsequent heating causes growth of these particles into larger colloidal objects, which may be produced via primary particle aggregation or through the condensation of monomeric titanium species. In both cases, the growth phase will imply the presence of condensation reactions, which may release alcohols or ethers as leaving groups.

## 2.2 Experimental Section

### *2.2.1 Materials*

Titanium (IV) tetra *n*-propoxide ($Ti(OC_3H_7)_4$, 98%), titanium (IV) tetra *n*-butoxide ($Ti(OC_4H_9)_4$, purity ≥97.0%), titanium (IV) tetraisopropoxide ($Ti[OCH(CH_3)_2]_4$, purity ≥97.0%), benzyl alcohol (anhydrous, purity 99.8%), 37% hydrochloric acid solution and 0.1 N hydrochloric acid solution were supplied by Sigma-Aldrich (Dorset, UK). Diethyl ether (anhydrous), toluene, dichloromethane and dimethyl formamide were supplied by Fisher Scientific U.K. Ltd. All materials were used as received from the supplier without any further purification. Water was pre-deionised (Elga) and further purified by a Milli-Q system (Millipore, U.K.)

### *2.2.2 Preparation of nanoparticles*

In each reactor of a Radleys Carousel 12 plus Reaction Station (Radleys, UK) 9.12 mmol of $Ti(OR)_4$ (R = propyl, butyl or isopropyl) were added under argon to 20 mL of benzyl alcohol containing appropriate amounts of water and hydrochloric acid to provide Ti:$H_2O$:Ti molar ratios of 1 : 4, 3.5, 3, 2.5 and 2 : 0.5 (constant HCl concentration) or 1 : 4 : 1.17, 1, 0.75 (constant water concentration); the highest HCl concentration was obtained directly adding 37% HCl to benzyl alcohol, while all other ratios were obtained by using appropriately diluted aqueous HCl. The pale yellow mixtures were vigorously stirred (magnetic agitation in 20 mL Carousel vials, 750 rpm) for 5 mins and the presence of dispersed objects was assessed via DLS; in control experiments the size of the dispersed objects was monitored for up to 24 h.

The reactions were then rapidly heated and reached the temperature of 80 °C at time = 4 mins, when samples were taken, and then again every 15 mins until either the nanoparticles reached the size of 8-10 nm or no growth could be observed. The reactions were cooled to room temperature, and in control experiments the size of the nanoparticles remained stable for at least 48 h.

The nanoparticle dispersions were then precipitated in 150 mL of diethyl ether and centrifuged (3,500 rpm, 5 mins). The supernatant was decanted and the resulting white solid was washed twice with 50 mL of diethyl ether. The precipitate was then re-dispersed in a 20 mL of a 50 %wt. water/ethanol solution at pH = 2 (obtained with 0.1 N HCl). The resulting solution was dialysed against purified water at pH = 2 using a regenerated cellulose dialysis membrane with a MWCO of 10,000 g/mol. The final concentration of the nanoparticle suspension (typically 5 mg/mL) was calculated by precipitating the content of 1 mL of sample by raising pH using 1 N $Na_2CO_3$, followed by centrifugation (3500 rpm, 5 mins) and decantation. The sample was washed with water and centrifuged again. 10 mL of water were finally and the resulting suspension was freeze dried.

### *2.2.3 Physico-chemical characterization*

*Attenuated Total Reflection Infrared Spectroscopy (ATR-IR).* IR spectra were recorded in ATR mode on a Tensor 27 Bruker spectrometer.

*Dynamic Light Scattering (DLS) and ζ potential analysis.* The measurements were performed using a Zetasizer Nano ZS instrument (Malvern Instrument Ltd., U.K.) connected to a Malvern autotitrator MPT-2. Unless otherwise stated, quartz cuvettes with an optical path of 10 mm and disposable capillary flow cells were used respectively for DLS and zeta potential measurements.

*Thermogravimetric Analysis (TGA)* 10 mg of freeze dried samples were analysed on a Mettler Toledo Starc System at a heating rate of 10°C per minute under air; an isotherm at 120°C was typically run until constant weight in order to ensure full water desorption.

*Transmission Electron Microscopy (TEM).* $TiO_2$ nanoparticles were analysed on a FEI Tecnai FEGTEM operated at 300 kV. For imaging, 10 μl of the purified nanoparticles in acidic media at a concentration of $1.7 \times 10^{-4}$ mg/mL were pipetted onto a carbon coated 300 mesh grid. The solution was then freeze dried on the grid to avoid aggregation of the nanoparticles.

*X-Ray Diffraction (XRD).* XRD patterns were obtained in reflection mode with CuK $\alpha$ radiation on an IPD PW1800 diffractometer (PANalytical) using freeze dried nanoparticles. The diffraction patterns were recorded only on tertiary nanoparticles (after precipitation, redispersion in water and freeze drying). Primary nanoparticles were excluded: due to their small size, they could not be precipitated from benzyl alcohol and the direct drying of their dispersion may modify the particle morphology due to capillary forces. Further, tertiary nanoparticles were preferred to secondary ones, in order to eliminate any effect due to the surface alkyl groups.

The fraction of crystalline (anatase) phase was calculated according to a literature method: considering $W_A$ the anatase weight fraction, $A_A$ the area of the anatase 101 peak and $A_R$ the area of the 110 peak for a known amount of rutile standard added to the sample, and using a correction factor (0.884) calculated by Gribb and Banfield using known mixtures of finely crystalline anatase and rutile[38], the weight fraction of anatase can be calculated as $W_A = \frac{0.884 A_A}{0.884 A_A + A_R}$. The Scherrer analysis was performed according to standard algorithms[39]. The calculation of the fractal dimension was performed as described by Rivallin et. al.[40].

## 2.3 Results and Discussion

### 2.3.1 *Role of water in the non-aqueous route.*

Despite being in principle a non-aqueous process, the “benzyl alcohol route” can be significantly influenced by the presence of water. We have initially noticed this phenomenon by using the reaction of ethanol and $TiCl_4$ in benzyl alcohol to produce anatase nanoparticles[34,35] (Figure 2.3.1-1; preparation described in Supplementary Information, section 1): in a humid environment (moist argon bubbled in the reaction environment) nanoparticles can be detected relatively quickly and rapidly grow in size, while decreasing the humidity they present a much slower growth (flow of dry argon, reactor open) or can also not condense at all (no evidence of nanoparticles after up 10 hours using dry argon and sealed reactors). This effect of water may go unnoticed because most commonly the synthesis of metal oxides via the benzyl alcohol route is performed under air and with non-anhydrous benzyl alcohol, therefore traces of water can easily be present. It should be noted that here we are working at a relatively low temperature which may not provide sufficient energy for condensation *via* ether elimination. The addition of catalytic amounts of $H_2O$ allows us to prepare nanoparticles without refluxing the solvent, which would have caused difficulties in sampling during the reaction.

The accelerating effect of water could be ascribed to two possible phenomena:

a) The direct involvement of water. In the benzyl alcohol route this may correspond to the hydrolysis of Ti-Cl bonds or of *in situ* formed titanium alkoxides, to eventually produce titanols, which have always been considered the most reactive groups in the production of Ti-O-Ti groups[41]. This would not contradict the occurrence of non-titanol based reaction, which have been demonstrated in the benzyl alcohol route (elimination of ethers or halides)[42,43], but would suggest that they may be operating as secondary condensation mechanisms.

b) A hydration-dependent catalytic activity of the HCl (more or less “naked” $H^+$).

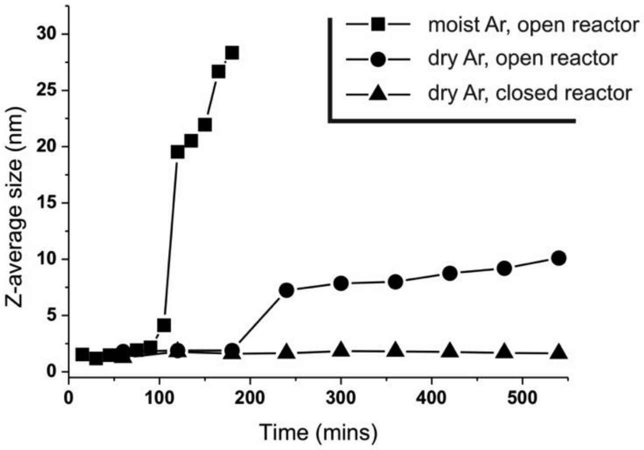

**Figure 2.3.1-1** Evolution of nanoparticle size in the reaction of $TiCl_4$ and ethanol (1:10 molar ratio) in benzyl alcohol at 80˚C (see Supplementary Information for the preparative details). Under completely inert conditions no nanoparticles were formed, however whilst leaving the reaction open nanoparticles form after an initial lag time of around 3 hours. Whilst performing the reaction under a $H_2O$ saturated atmosphere nanoparticles were formed after a short lag time of 90 minutes, then growing in an uncontrollable fashion.

### *2.3.2 Primary particles (room temp. nucleation).*

In order to clarify the role of water, we have tried to separate the preparative variables modifying the classical benzyl alcohol route by 1) adding HCl to preformed titanium alkoxides instead of producing them *in situ* through the reaction of $TiCl_4$ + alcohols, for a better control over pH; 2) using a series of alkoxides with variable hydrophobicity and resistance to hydrolysis ($Ti(OnPr)_4$, $Ti(O^iPr)_4$, $Ti(OnBu)_4$; $Ti(OEt)_4$ was excluded due to its too rapid reactivity) as the means to identify effects due to the aliphatic groups (if there are, there must be a variation of properties in the series); it is noteworthy that the bulkiness of the alkyl residues should also allow to reduce ligand exchange with benzyl alcohol.

The size of the colloidal products of this early phase of condensation was used as a measure of the effects of the nature of the alkoxide, of acidity (expressed through the Cl/Ti molar ratio) and of the water content (expressed through the $H_2O$/Ti molar ratio). We have first focused on the particles produced upon mixing of the reagents at room temperature, which were typically sized 2.5 – 5 nm and are hereafter referred to as primary nanoparticles.

Negligible differences were recorded among the three alkoxides. For all of them and independently on the HCl content, the nanoparticle size increased with increasing water content, with the limit of macroscopic precipitation for $H_2O/Ti > 4$ (Figure 2.3.2-1, left and centre). Interestingly, this ratio is close to the theoretical complete conversion of alkoxide to titanols, therefore it is reasonable to assume that macroscopic aggregation occurs upon quantitative hydrolysis.

The lack of differences attributable to the alkoxides and the predominant role of water suggest that a) primary nanoparticles are formed through titanol condensation, while direct titanol condensation would appear to have a negligible role under these conditions (room temperature and acidic environment), b) their surface should present an alkoxide-rich surface, acting as a barrier towards further aggregation. It is noteworthy that at $H_2O/Ti = 4$ a significant amount of alkoxides must still present, therefore the surface of primary nanoparticles is likely to present mixtures of alkoxides and titanols.

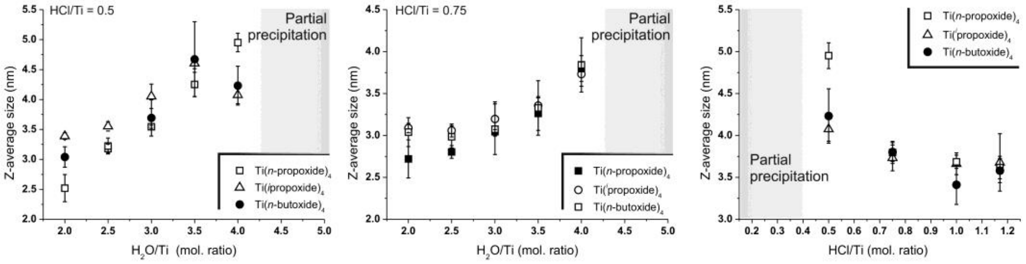

**Figure 2.3.2-1** ***Left and centre:*** Size of primary nanoparticles as a function of the water content at a constant HCl concentration (Cl/Ti mol. ratio = 0.75 in the left graph and = 0.5 in centre graph). In all experiments [Ti] = 456 mM. ***Right:*** Size of primary nanoparticles as a function of HCl concentration at a constant water content ($H_2O$/Ti mol. ratio = 4). Error bars are calculated on the basis of three separate preparative experiments.

HCl concentration seemed to have an effect on primary particle size only for Cl/Ti $\leq$ 0.5 (Figure 2.3.2-1, right), under which conditions the presence of macroscopic aggregates became appreciable; since the formation of chlorinated species would determine an opposite trend (higher reactivity and thus larger size with increasing Cl content), we are inclined to ascribe this effect to a lack of electrostatic stabilization due to insufficient surface protonation.

### *2.3.3 Secondary particles (thermal growth).*

Primary nanoparticles were indefinitely stable at room temperature but, as for the classical non-aqueous route, grew in size upon heating. This growth is attributable to further condensation of surface alkoxide groups either between themselves (aggregation of primary particles) or with monomeric titanium alkoxides (growth via surface condensation on primary nanoparticles) to yield larger colloidal objects, which are hereafter termed secondary nanoparticles. It is noteworthy that the mechanism of growth via aggregation would allow to explain the typical conglomerate morphology of the products of the classical non-aqueous process, where primary particles can still be recognized[34].

In this thermal growth phase, the agglomeration kinetics showed a small accelerating effect of HCl concentration (Figure 2.3.3-1 A-C, shown for $H_2O$/Ti = 4), which may be ascribed to its role as a catalyst in the process, or to a different internal structure of the particles produced: under the hypothesis of aggregation of primary particles, increasing surface protonation would lead to a less compact aggregate due to repulsion between neighbouring groups (hence a lower fractal dimension of the particle).

In terms of the titanium/water molar ratio, two different regimes are recognizable: A) primary particles prepared with $H_2O/Ti < 4$; the aggregation rate appeared to slightly increase with increasing initial amount of water; on the other hand, although butoxide-covered nanoparticles appeared to grow slower, the effects of the aliphatic residues were not statistically relevant (Figure 2.3.3-1 A-C). B) Primary particles prepared with $H_2O/Ti = 4$; the growth kinetics were much more rapid and clearly alkoxide-sensitive ($^i$Pro>>*n*BuO≥*n*PrO). The HCl concentration did not significantly influence the dependency on the water content; although the results were more noisy due to their border-line stability, a similar trend was observed also for particles prepared with Cl/Ti = 0.5 (see chapter 2.6 Supplementary Information, Figure 2.6.2-SI-1). This accelerated growth under conditions where the presence of intact titanium tetraalkoxides is unlikely ($H_2O/Ti = 4$), would support the hypothesis of growth via aggregation, which is further confirmed by the increase in the width of the size distribution during the thermal treatment (see chapter 2.6.3 and Figure 2.6.3-SI-1).

The surface of primary nanoparticles may present a non-negligible amount of titanols; therefore, the growth by aggregation could be associated to the production of both ethers (condensation of two alkoxides) or alcohols (titanol + alkoxide condensation). A growth mechanism predominantly based on the formation of alcohols would explain the much slower growth under conditions that likely minimize the amount of titanols, i.e. for $H_2O/Ti < 4$ and would also provide an easy explanation of the enhanced reactivity of isopropoxide-containing particles at $H_2O/Ti = 4$. Isopropanol boiling point (82°C) is indeed very close to the reaction temperature, while the other alcohols are much less volatile ($T_b$ = 98 and 118°C, resp. for *n*PrOH and *n*BuOH) and would explain the similarly slower kinetics of the corresponding particles. This explanation would not hold for ethers as leaving groups: $Ti(OnPr)_4$-derived particles do not grow much faster than $Ti(OnBu)_4$-derived ones, although the corresponding ethers have very different boiling points ($T_b$ = 90 vs. 142°C). However, it is worth pointing out that the accelerated growth of $Ti(O^iPr)_4$-derived particles may also derive from a lower surface protonation of the very hydrophobic isopropoxy groups.

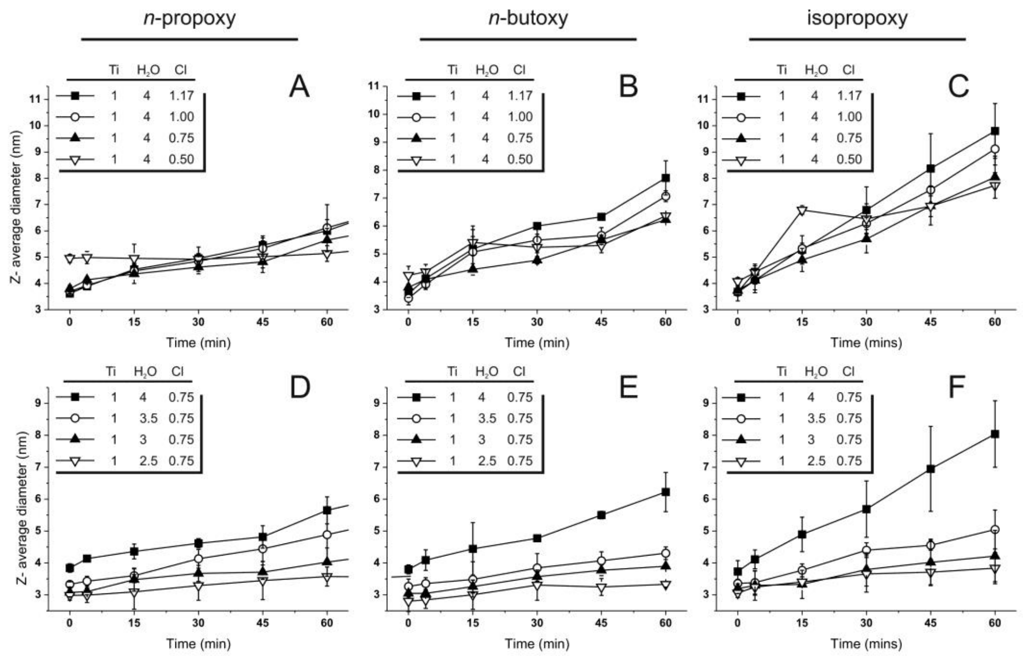

**Figure 2.3.3-1** Evolution of size (T = 80ºC) as a function of time and of the amount of HCl (*A to C*) or of water (*D to F*) added to solutions of $Ti(OnPr)_4$ (*left*), $Ti(OnBu)_4$ (*centre*), and $Ti(O^iPr)_4$ (*right*). Error bars are calculated on the basis of three separate preparative experiments.

### ***2.3.4 Tertiary particles (solvent-dependent agglomeration).***

Secondary nanoparticles (Ti:$H_2O$:HCl 1:4:1.17 molar ratio, size peaked around 7.5 nm) can be precipitated via addition of diethyl ether. They could be easily redispersed in benzyl alcohol without any change in their size distribution (Figure 2.3.4-1, top), thus indicating that no significant aggregation occurred in the precipitate.

Similarly to what previously seen for more agglomerated titania nanocrystals[34], the particles could then be redispersed in water, under acid conditions (pH = 2) that allowed at the same time full hydrolysis of the residual alkoxides and electrostatic stabilization due to the provision of a positive Zeta potential through surface protonation. In water, the nanoparticles showed an alkoxide-dependent aggregation (*n*Pro>*n*BuO>$^{i}$PrO), which indirectly confirms the presence of the original alkoxides on the nanoparticles after thermal growth (Figure 2.3.4-1, bottom). It is particularly noteworthy that the size of the particles prepared from $Ti(O^{i}Pr)_4$ was substantially unaltered in this process.

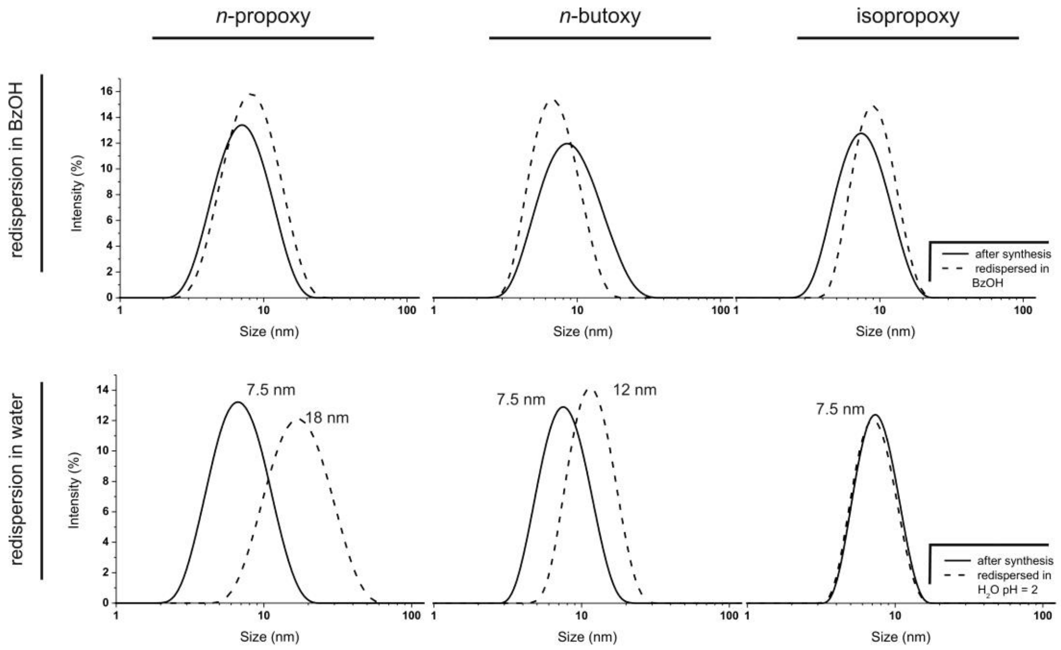

**Figure 2.3.4-1** Size distribution of nanoparticles prepared from Ti(O*n*Pr)$_4$ (*left*), Ti(O*n*Bu)$_4$ (*centre*) and $Ti(O^{i}Pr)_4$ (*right*) in benzyl alcohol at $H_2O/Ti = 4$; the particles were heated at 80ºC for the time necessary to reach an identical final size (=degree of agglomeration) of 7.5 nm. The nanoparticles were precipitated in diethyl ether and redispersed in benzyl alcohol (*top*) or in water at pH = 2 (*bottom*). The process of redispersion in water induced a variable degree of aggregation, which appears to correlate inversely to the hydrophobicity of the aliphatic residues; this effect was quantitatively reproducible (at least three separate experiments with negligible differences in Z-average size and width of the distribution). Nanoparticle concentration: 10 mg/mL after redispersion.

IR spectra (Figure 2.3.4-2, left) showed that organic species were present in the precipitate; they appeared also to include benzyl groups, which suggests a partial, although not quantitative exchange of the surface alkoxides. The organic species disappeared upon redispersion in water; in TGA the redispersion was accompanied by the substantial reduction of the high-temperature mass loss step, from ~20 to ~6%wt. of the dry mass (Figure 2.3.4-2, right and Table 2.3.4-1). It is noteworthy that IR spectra showed the presence of OH groups both before and after redispersion; due to the characteristic $\delta$OH at 1600 cm$^{-1}$ and the considerable mass loss upon

120°C isotherm in TGA, it is possible to identify them as water, most likely adsorbed on the positively charged nanoparticles during isolation and analysis.

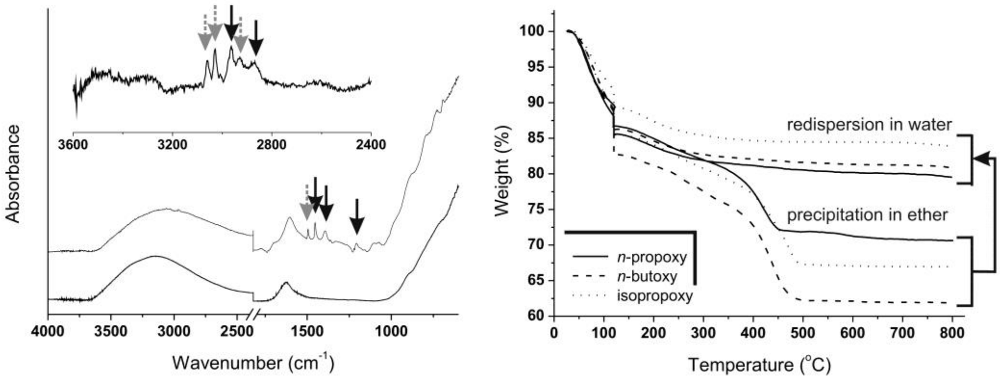

**Figure 2.3.4-2** ***Left.*** IR spectra of nanoparticles prepared from Ti(O$^i$Pr)$_4$ with a $H_2O$/Ti = 4 molar ratio precipitated from diethyl ether (*top*) and after redispersion in acidic water and drying at 120 °C (*bottom*). The inset shows a magnified view of the 2400-3600 cm$^{-1}$ region of spectrum a, after removal of the OH stretching band for spectrum *(a)*. Water is easily recognizable in both spectra from the presence of a broad OH stretching peak 2500-3500 cm$^{-1}$ and from the OH bending one at 1600 cm$^{-1}$. The isopropyl groups can be recognized (black arrows) through the peaks at 2964 and 2875 cm$^{-1}$ (resp. asymmetric and symmetric $CH_3$ stretching), by the sharp band at 1450 cm$^{-1}$ and the broad one around 1390 cm$^{-1}$ (resp. asymmetric $CH_3$ bending and most likely coalescence of the two bands associated to geminal symmetric $CH_3$ bending). Benzyl groups (grey arrows) can be recognized from the peaks 3028 and 3059 cm$^{-1}$ (two forms of =C-H stretching), at 1495 cm$^{-1}$ (aromatic ring breathing) and possibly at 2925 cm$^{-1}$ (asymmetric $CH_2$ stretching). ***Right.*** TGA runs of nanoparticles before and after redispersion. An isotherm was held at 120°C until constant weight to ensure the full desorption of water, which was present in all samples as already appeared in infrared analysis.

Since aggregation cannot be ascribed to phenomena occurring in the precipitate, it is reasonable to assume that the different agglomeration in water is due to the different hydrolysis behaviour of the surface alkoxides. However, rather unexpectedly the extent of aggregation was inversely proportional to the hydrophobicity of the alkoxides, and thus also to their rate of hydrolysis. The explanation probably lies in the interplay between the kinetics of surface hydrolysis and of protonation by the strongly acidic environment: OH groups promote aggregation, while positive charges (easier introduced on an OH-containing surface) discourage it. The slow reactivity of isopropoxy groups likely allows break-down of the precipitate and dense protonation of the nanoparticle surface before significant hydrolysis has occurred; on the other hand, the introduction of titanol groups on diluted and highly charged particles would not have appreciable effect on their aggregation.

**Table 2.3.4-1** Mass loss associated to evaporation of water and elimination of other volatile products for nanoparticles prepared with a Ti:$H_2O$:HCl 1:4:1.17 molar ratio.

| **Precursor →** | $Ti(OnPr)_4$ | | $Ti(OnBu)_4$ | | $Ti(O^iPr)_4$ | |
|---|---|---|---|---|---|---|
| **Content (% wt.)↓** | precip. | redisp. | precip. | redisp. | precip. | redisp. |
| “free” $H_2O$ [a] | 13.4 | 10.7 | 17.4 | 13.8 | 14.6 | 14.6 |
| bound $H_2O$, TiOR, TiOH [b] | 18.4 | 6.1 | 21.6 | 6.2 | 21.6 | 6.9 |

[a] calculated from the relative mass loss after an isothermal treatment at 120°C

[b] calculated from the relative mass loss at 500°C in relation to the “dry” weight of the nanoparticles, i.e. considering the weight at 125°C as 100%.

With an appropriate choice of the alkoxides it was therefore possible to control and also eliminate the stage of solvent-induced agglomeration, therefore allowing the production ligand-free secondary nanoparticles (average size ≈ 7.5 nm) in a water environment.

### 2.3.5 *Internal structure of secondary nanoparticles.*

Nanoparticles were analyzed via TEM and XRD after their redispersion in water. TEM broadly confirmed the dimensional data obtained via DLS, with an average size of 7-8 nm for secondary nanoparticles (Figure 2.3.5-1, left); it further showed the nanoparticles to be highly crystalline with 3.5 Å-spaced lattice fringes, which have already been recorded in the products of classical non-aqueous process[44] and correspond to the spacing between the 101 planes of anatase[45]. XRD showed all nanoparticles to be essentially composed of highly crystalline anatase (Figure 2.3.5-1, right and Table 2.3.5-1), as it was also recorded for the classical non-aqueous process[46]; the average crystallite size was always in the range of 3-4 nm, a value in good agreement with previous results of the classical non-aqueous route[34], and strikingly corresponding to the size of primary nanoparticles, despite the approximations intrinsic to the Scherrer equation (e.g. that of a spherical shape of the particles).

It is also worth noting that while the amount of acid catalyst did not appreciably influence either parameter, confirming its non-critical role in the process, the nature of the alkoxide appeared to have some effect on crystallinity, with a slight decrease in the order ${}^{i}$PrO>$n$PrO≥$n$BuO that may be a result of a different kinetics of primary particle formation.

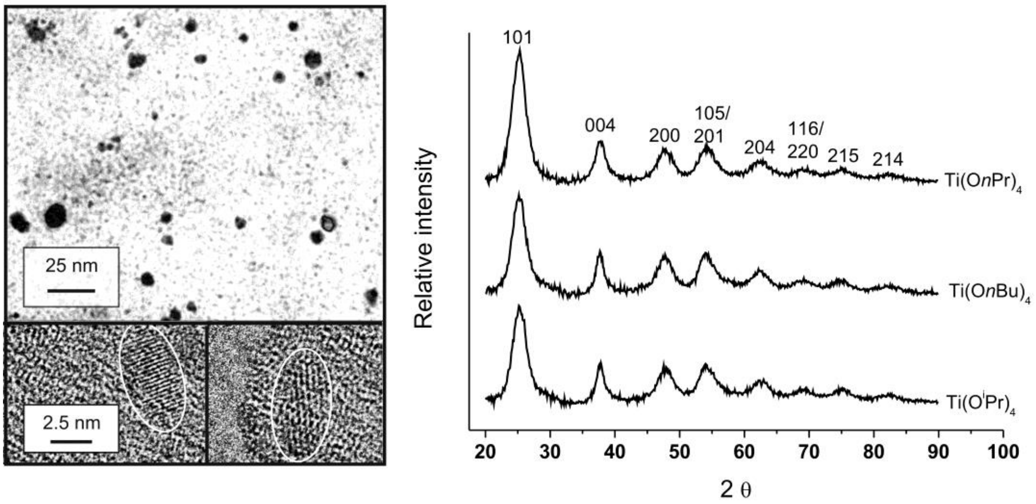

**Figure 2.3.5-1** ***Left.*** TEM images of nanoparticles obtained from $Ti(O^{i}Pr)_4$ in benzyl alcohol after redispersion in water. Most nanoparticles appeared to be sized in the region of 6-9 nm. High resolution images (bottom) show that in single nanoparticles the spacing between crystalline planes was 3.2 Å, which corresponds to the spacing between the 101 crystal plane of anatase. ***Right.*** XRD patterns of nanoparticles freeze dried from an aqueous suspension prepared using the three different titanium tetraalkoxy precursors.

In general, independently on the behaviour during thermal growth (secondary nanoparticles) and/or solvent-induced agglomeration (tertiary nanoparticles), all systems showed rather similar values of crystallinity and crystallite size, which are easy to ascribe to the primary nanoparticles.

The identification of primary particles after thermal growth (and also water redispersion) confirms the hypothesis that this phase is based on their aggregation rather than on their surface growth due to monomer deposition. Correspondingly, it can be expected the fractal dimension of the secondary particles to be <3, due to the statistical nature of the aggregation process. Typically, in a 3D structure $D_f$ would approach the value of 3 in the limit of very dense packing, while a dendritic structure can push this parameter significantly below 2.

**Table 2.3.5-1** Anatase content and crystallite size of nanoparticles as a function of the amount of HCl and of the nature of the titanium alkoxide.

| $Ti:H_2O:HCl$ molar ratio | Crystallite size (nm) [a] | | | Anatase content (% wt.) [b] | | |
|---|---|---|---|---|---|---|
| | $Ti(OnPr)_4$ | $Ti(OnBu)_4$ | $Ti(O^iPr)_4$ | $Ti(OnPr)_4$ | $Ti(OnBu)_4$ | $Ti(O^iPr)_4$ |
| 1 : 4 : 1.17 | 3.9 | 3.7 | 4.1 | 83 | 80 | 98 |
| 1 : 4 : 1 | 4.1 | 3.9 | 4.1 | 96 | 82 | 95 |
| 1 : 4 : 0.75 | 4.0 | 3.9 | 4.0 | 91 | 84 | 97 |
| 1 : 4 : 0.50 | 4.0 | 3.5 | 3.6 | 86 | 84 | 90 |

[a] The crystallite size was calculated through the Scherrer analysis[47] of the 101 peak; the data may not precisely estimate the actual crystallite size and methods other than Scherrer’s ones can be used in alternative[39].

[b] Calculated from the area of 101 peak[38], as described in the experimental section with the presumption that the remaining mass is attributed to amorphous material.

Static light scattering (SLS) is the method of choice for the determination of the fractal dimensions of colloids[48-50]: by plotting the scattered intensity $I$ as a function of the scattering vector $q = \frac{4\pi n \sin\vartheta}{\lambda}$ in a log-log plot, it is generally possible to calculate the fractal dimension $D_f$ of aggregates as the slope of the graphs. The main underlying assumption is that the dependency of $I$ on $q$ is mostly due to the structure factor $S(q)$, which scales with $q$ as a power of $D_f$, i.e. $S(q) \propto q^{-Df}$; this assumption, however, is valid only when the aggregated particles have an average radius of gyration ($R_g$) comparable or larger than the wavelength of the light used in the experiments (specifically, it should be $< R_g > q \gg 1$). This condition is not fulfilled in the present case; for example, at the end of the growth phase the largest nanoparticles, i.e. $Ti(O^iPr)_4$-derived nanoparticles produced with 1 : 4 : 1.17 $Ti:H_2O:HCl$ molar ratio, showed $< R_g > \approx$ 16 nm (see Chapter 2.6.4 Supplementary Information, Figure 2.6.4-SI-1), which is far too small in comparison to the wavelength of visible light. Correspondingly, log($I$) vs. log($q$) plots do not provide useful information about $D_f$ (see chapter 2.6.4 Supplementary Information, Figure 2.6.4-SI-2). An alternative SLS approach would use the relationship between $I(0)$ (intensity at $q$=0) and the $\frac{<R_g>}{R_p}$ ratio ($R_P$ being the radius of the primary particles), whose slope in a log-log plot would again provide the fractal dimension[51,52]. However, this approach is rather cumbersome (a Zimm plot per time point) and is affected by significant errors in the estimation of $< R_g >$ at early time points, due to the contribution of primary particles. A considerably simpler approach has been employed on similarly sized titania nanoparticles (5-40 nm) by the group of Kanaev who have used the relationship between log($I$) and log($R_H$) to calculate $Df$ as the slope of the corresponding log-log graphs (Figure 2.3.5-2, left)[40]. The theoretical foundation of this simplified method is essentially the same as for obscuration method proposed by Wu and Morbidelli (scattered intensity $\propto \left(\frac{<R_g>}{R_p}\right)^{Df}$), but the approximation of the particle dimension with the hydrodynamic radius is advantageous since it allows measurements to be performed in DLS mode (i.e. single angle, single concentration), although with a likely reduction in precision. We have accordingly fitted the scattering data recorded during the thermal growth phase, obtaining fractal dimensions always <3 (Figure 2.3.5-2, right).

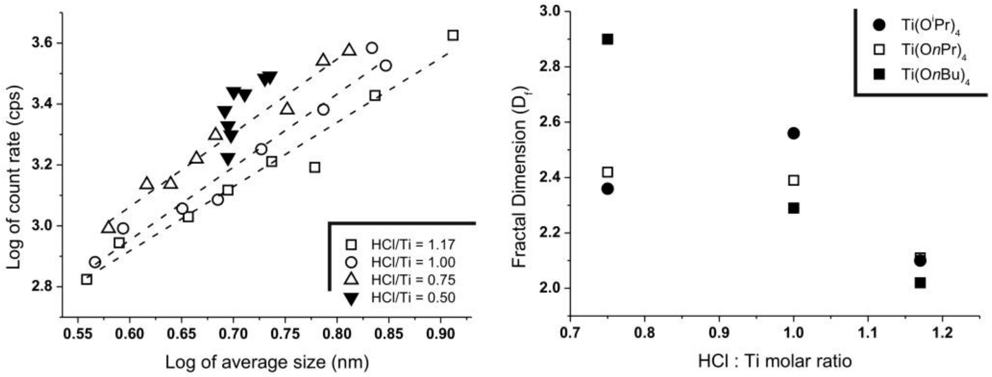

**Figure 2.3.5-2** ***Left.*** Log-log plot of nanoparticle Z-average size vs. equivalent count rate at different times for (precursor: Ti(O$^i$Pr)$_4$ ; Ti:H$_2$O 1:4); the dashed lines show the results of fittings. Please note that at Ti:HCl=0.5 D$_f$ became undefined. ***Right.*** Dependency of the fractal dimension of secondary nanoparticles on the acid content and on the nature of the titanium alkoxide.

In our case, it could be expected the ζ-potential of primary particles to play a critical role in determining the fractal dimensions of secondary particles, since larger internal repulsive interactions in the aggregates would reduce their compactness (Scheme 2.3.5-1).

Our results indeed showed a significant influence of HCl concentration and hence of surface protonation. First, at HCl:Ti = 0.5 the fractal dimension was undefined (diverged) for all titanium alkoxides: we have previously seen (Figure 2.3.5-2, right) nanoparticles to be close to flocculation at this HCl:Ti ratio, and the hypothesised lack of electrostatic repulsion fits with the formation of very compact 3D aggregates. Second, using larger amounts of HCl (Figure 2.3.5-2, right and Table 2.3.5-2) the fractal dimension gradually decreased with increasing acid content, which is easily explained with a more dendritic growth with higher electrostatic repulsion.

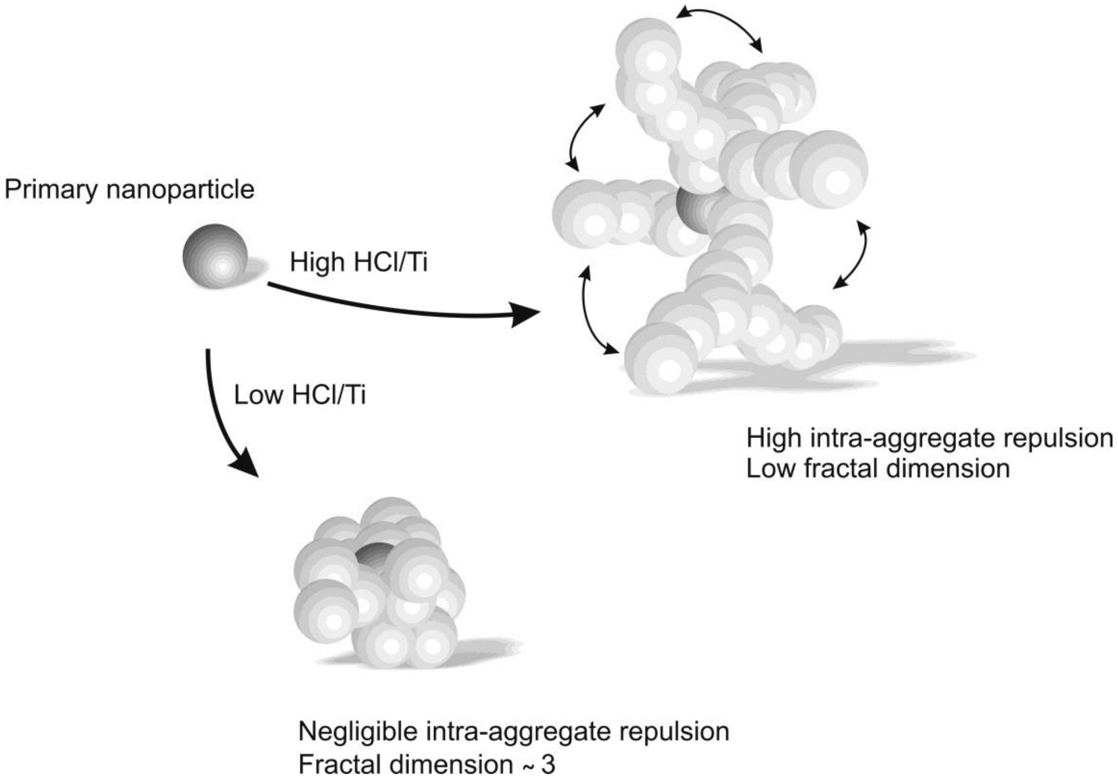

**Scheme 2.3.5-1** The mode of aggregation of primary nanoparticles should be strongly dependent on the intensity of their mutual repulsion, with more open structures produced at high Zeta potential values.

**Table 2.3.5-2** $D_f$ calculated for the growth of secondary nanoparticles as a function of the nature of the titanium alkoxide and the HCl/Ti molar ratio.

| Ti : $H_2O$ : HCl → <br>Precursor ↓ | 1 : 4 : 1.17 | 1 : 4 : 1 | 1 : 4 : 0.75 | 1 : 4 : 0.5 |
|---|---|---|---|---|
| $Ti(OPr)_4$ | 2.1 | 2.4 | 2.4 | - |
| $Ti(OBu)_4$ | 2.0 | 2.3 | 2.9 | - |
| $Ti(O^iPr)_4$ | 2.1 | 2.6 | 2.4 | - |

## 2.4 Conclusion

In this study we have demonstrated a key principle: the non-aqueous route to titanium dioxide could in reality be based on the presence of traces of water; indeed the careful dosage of water (and HCl) allows not only to avoid the lag time typical of non-aqueous processes[34,37,42], but also to operate a very precise control over dimensions and aggregation of the titania nanoparticles. In this way, we have been able to obtain stable water dispersions of ligand-free anatase nanoparticles sized less than 8 nm.

Further, we have established that:

a) The processes of thermal growth and redispersion in water are much influenced by the nature of the organic residues in the titanium alkoxide precursors; in particular, in a counter-intuitive fashion the more hydrophobic isopropoxy residues appear to minimize aggregation during redispersion, probably because of the slower kinetics of hydrolysis that allows complete breakdown of the precipitate before substantial amount of titanols are produced.

b) The process of thermal growth is due to the aggregation of primary nanoparticles and appears to be dependent also on the amount of OH groups present on their surface, therefore suggesting the aggregation to be based on the elimination of alcohols rather than ethers. This process has a statistical nature, and the fractal dimension (the compactness) of the resulting nanoparticles appears to depend on the acid content, which suggests it to be dominated by the charge of surface sites. Due to the different surface area of particles featuring different fractal dimension, it is expected this to have also an influence on the photo-oxidation activity.

## 2.5 References

1. Nazeeruddin, M. K.; Baranoff, E.; Gratzel, M., Dye-sensitized solar cells: A brief overview. *Sol. Energy* **2011,** 85, (6), 1172-1178.

2. Mercado, C.; Seeley, Z.; Bandyopadhyay, A.; Bose, S.; McHale, J. L., Photoluminescence of Dense Nanocrystalline Titanium Dioxide Thin Films: Effect of Doping and Thickness and Relation to Gas Sensing. *ACS Appl. Mater. Interfaces* **2011,** 3, (7), 2281-2288.

3. Parkin, I. P.; Palgrave, R. G., Self-cleaning coatings. *J. Mater. Chem.* **2005,** 15, (17), 1689-1695.

4. Serpone, N.; Dondi, D.; Albini, A., Inorganic and organic UV filters: Their role and efficacy in sunscreens and suncare product. *Inorg. Chim. Acta.* **2007,** 360, (3), 794-802.

5. Li, Q. L.; Mahendra, S.; Lyon, D. Y.; Brunet, L.; Liga, M. V.; Li, D.; Alvarez, P. J. J., Antimicrobial nanomaterials for water disinfection and microbial control: Potential applications and implications. *Water Res.* **2008,** 42, (18), 4591-4602.

6. Ramires, P. A.; Romito, A.; Cosentino, F.; Milella, E., The influence of titania/hydroxyapatite composite coatings on in vitro osteoblasts behaviour. *Biomaterials* **2001,** 22, (12), 1467-1474.

7. Bachle, M.; Kohal, R. J., A systematic review of the influence of different titanium surfaces on proliferation, differentiation and protein synthesis of osteoblast-like MG63 cells. *Clin. Oral Implant. Res.* **2004,** 15, (6), 683-692.

8. Ellingsen, J. E., A study on the mechanism of protein adsorption on $TiO_2$. *Biomaterials* **1991,** 12, (6), 593-596.

9. Wang, J. X.; Zhou, G. Q.; Chen, C. Y.; Yu, H. W.; Wang, T. C.; Ma, Y. M.; Jia, G.; Gao, Y. X.; Li, B.; Sun, J.; Li, Y. F.; Jiao, F.; Zhao, Y. L.; Chai, Z. F., Acute toxicity and biodistribution of different sized titanium dioxide particles in mice after oral administration. *Toxicol. Lett.* **2007,** 168, (2), 176-185.

10. Brunner, T. J.; Wick, P.; Manser, P.; Spohn, P.; Grass, R. N.; Limbach, L. K.; Bruinink, A.; Stark, W. J., In vitro cytotoxicity of oxide nanoparticles: Comparison to asbestos, silica, and the effect of particle solubility. *Environ. Sci. Technol.* **2006,** 40, (14), 4374-4381.

11. Sayes, C. M.; Wahi, R.; Kurian, P. A.; Liu, Y. P.; West, J. L.; Ausman, K. D.; Warheit, D. B.; Colvin, V. L., Correlating nanoscale titania structure with toxicity: A

cytotoxicity and inflammatory response study with human dermal fibroblasts and human lung epithelial cells. *Toxicol. Sci.* **2006,** 92, (1), 174-185.

12. Trouiller, B.; Reliene, R.; Westbrook, A.; Solaimani, P.; Schiestl, R. H., Titanium Dioxide Nanoparticles Induce DNA Damage and Genetic Instability In vivo in Mice. *Cancer Res.* **2009,** 69, (22), 8784-8789.

13. Hirakawa, K.; Mori, M.; Yoshida, M.; Oikawa, S.; Kawanishi, S., Photo-irradiated titanium dioxide catalyzes site specific DNA damage via generation of hydrogen peroxide. *Free Radic. Res.* **2004,** 38, (5), 439-447.

14. Zhu, Y. L.; Eaton, J. W.; Li, C., Titanium Dioxide ($TiO_2$) Nanoparticles Preferentially Induce Cell Death in Transformed Cells in a Bak/Bax-Independent Fashion. *PLoS One* **2012,** 7, (11).

15. Kubota, Y.; Shuin, T.; Kawasaki, C.; Hosaka, M.; Kitamura, H.; Cai, R.; Sakai, H.; Hashimoto, K.; Fujishima, A., Photokilling of T-24 human bladder-cancer cells with titanium-dioxide. *Br. J. Cancer* **1994,** 70, (6), 1107-1111.

16. Ethirajan, M.; Chen, Y. H.; Joshi, P.; Pandey, R. K., The role of porphyrin chemistry in tumor imaging and photodynamic therapy. *Chem. Soc. Rev.* **2011,** 40, (1), 340-362.

17. Bonnett, R., Photosensitizers of the porphyrin and phtalocanine series for photodynamic therapy. *Chem. Soc. Rev.* **1995,** 24, (1), 19-33.

18. Bacsa, R. R.; Kiwi, J., Effect of rutile phase on the photocatalytic properties of nanocrystalline titania during the degradation of p-coumaric acid. *Appl. Catal. B-Environ.* **1998,** 16, (1), 19-29.

19. Ohno, T.; Sarukawa, K.; Tokieda, K.; Matsumura, M., Morphology of a $TiO_2$ photocatalyst (Degussa, P-25) consisting of anatase and rutile crystalline phases. *J. Catal.* **2001,** 203, (1), 82-86.

20. Ashikaga, T.; Wada, M.; Kobayashi, H.; Mori, M.; Katsumura, Y.; Fukui, H.; Kato, S.; Yamaguchi, M.; Takamatsu, T., Effect of the photocatalytic activity of TiO2 on plasmid DNA. *Mutat. Res-Gen. Tox. En.* **2000,** 466, (1), 1-7.

21. Nagaveni, K.; Sivalingam, G.; Hedge, M. S.; Madras, G., Solar photocatalytic degradation of dyes: high activity of combustion synthesized nano $TiO_2$. *Appl. Catal. B-Environ.* **2004,** 48, (2), 83-93.

22. Konovalova, T. A.; Lawrence, J.; Kispert, L. D., Generation of superoxide anion and most likely singlet oxygen in irradiated $TiO_2$ nanoparticles modified by carotenoids. *J. Photochem. Photobiol. A-Chem.* **2004,** 162, (1), 1-8.

23. Kamps, K.; Leek, R.; Luebke, L.; Price, R.; Nelson, M.; Simonet, S.; Eggert, D. J.; Atesin, T. A.; Brown, E. M. B., Surface modification of the $TiO_2$ nanoparticle surface enables fluorescence monitoring of aggregation and enhanced photoreactivity. *Integr. Biol.* **2013,** 5, (1), 133-143.

24. Kosmulski, M., The significance of the difference in the point of zero charge between rutile and anatase. *Adv. Colloid Interface Sci.* **2002,** 99, (3), 255-264.

25. Nam, H. J.; Amemiya, T.; Murabayashi, M.; Toh, K., Photocatalytic activity of sol-gel TiO($_2$) thin films on various kinds of glass substrates: The effects of Na(+) and primary particle size. *J. Phys. Chem. B* **2004,** 108, (24), 8254-8259.

26. Xiong, S. J.; George, S. J.; Ji, Z. X.; Lin, S. J.; Yu, H. Y.; Damoiseaux, R.; France, B.; Ng, K. W.; Loo, S. C. J., Size of $TiO_2$ nanoparticles influences their phototoxicity: an in vitro investigation. *Arch. Toxicol.* **2013,** 87, (1), 99-109.

27. Rajh, T.; Thurnauer, M. C.; Thiyagarajan, P.; Tiede, D. M., Structural characterization of self-organized $TiO_2$ nanoclusters studied by small angle neutron scattering. *J. Phys. Chem. B* **1999,** 103, (12), 2172-2177.

28. Li, G. S.; Li, L. P.; Boerio-Goates, J.; Woodfield, B. F., High purity anatase $TiO_2$ nanocrystals: Near room-temperature synthesis, grain growth kinetics, and surface hydration chemistry. *J. Am. Chem. Soc.* **2005,** 127, (24), 8659-8666.

29. Wang, C. C.; Ying, J. Y., Sol-gel synthesis and hydrothermal processing of anatase and rutile titania nanocrystals. *Chem. Mat.* **1999,** 11, (11), 3113-3120.

30. Cushing, B. L.; Kolesnichenko, V. L.; O'Connor, C. J., Recent advances in the liquid-phase syntheses of inorganic nanoparticles. *Chem. Rev.* **2004,** 104, (9), 3893-3946.

31. Bilecka, I.; Niederberger, M., New developments in the nonaqueous and/or non-hydrolytic sol-gel synthesis of inorganic nanoparticles. *Electrochim. Acta* **2010,** 55, (26), 7717-7725.

32. Rossmanith, R.; Weiss, C. K.; Geserick, J.; Husing, N.; Hormann, U.; Kaiser, U.; Landfester, K., Porous anatase nanoparticles with high specific surface area prepared by miniemulsion technique. *Chem. Mat.* **2008,** 20, (18), 5768-5780.

33. Niederberger, M., Nonaqueous sol-gel routes to metal oxide nanoparticles. *Accounts Chem. Res.* **2007,** 40, (9), 793-800.

34. Kotsokechagia, T.; Cellesi, F.; Thomas, A.; Niederberger, M.; Tirelli, N., Preparation of ligand-free $TiO_2$ (anatase) nanoparticles through a nonaqueous process and their surface functionalization. *Langmuir* **2008,** 24, (13), 6988-6997.

35. Kotsokechagia, T.; Zaki, N. M.; Syres, K.; de Leonardis, P.; Thomas, A.; Cellesi, F.; Tirelli, N., PEGylation of Nanosubstrates (Titania) with Multifunctional Reagents: At the Crossroads between Nanoparticles and Nanocomposites. *Langmuir* **2012,** 28, (31), 11490-11501.

36. Nair, B., Final report on the safety assessment of Benzyl Alcohol, Benzoic Acid, Sodium Benzoate. *Int. J. Toxicol.* **2001,** 20, (Supplement 3), 23-50.

37. Jensen, G. V.; Bremholm, M.; Lock, N.; Deen, G. R.; Jensen, T. R.; Iversen, B. B.; Niederberger, M.; Pedersen, J. S.; Birkedal, H., Anisotropic Crystal Growth Kinetics of Anatase TiO($_2$) Nanoparticles Synthesized in a Nonaqueous Medium. *Chem. Mat.* **2010,** 22, (22), 6044-6055.

38. Gribb, A. A.; Banfield, J. F., Particle size effects on transformation kinetics and phase stability in nanocrystalline $TiO_2$. *Am. Miner.* **1997,** 82, (7-8), 717-728.

39. Uvarov, V.; Popov, I., Metrological characterization of X-ray diffraction methods for determination of crystallite size in nano-scale materials. *Mater. Charact.* **2007,** 58, (10), 883-891.

40. Rivallin, M.; Benmami, M.; Gaunand, A.; Kanaev, A., Temperature dependence of the titanium oxide sols precipitation kinetics in the sol-gel process. *Chem. Phys. Lett.* **2004,** 398, (1-3), 157-162.

41. Yoldas, B. E., Hydrolysis of titanium alkoxide and effects of hydrolytic polycondensation parameters. *J. Mater. Sci.* **1986,** 21, (3), 1087-1092.

42. Garnweitner, G.; Grote, C., In situ investigation of molecular kinetics and particle formation of water-dispersible titania nanocrystals. *Phys. Chem. Chem. Phys.* **2009,** 11, (19), 3767-3774.

43. Niederberger, M.; Garnweitner, G., Organic reaction pathways in the nonaqueous synthesis of metal oxide nanoparticles. *Chem.-Eur. J.* **2006,** 12, (28), 7282-7302.

44. Schattauer, S.; Reinhold, B.; Albrecht, S.; Fahrenson, C.; Schubert, M.; Janietz, S.; Neher, D., Influence of sintering on the structural and electronic properties of $TiO_2$ nanoporous layers prepared via a non-sol-gel approach. *Colloid Polym. Sci.* **2012,** 290, (18), 1843-1854.

45. Wen, P. H.; Itoh, H.; Tang, W. P.; Feng, Q., Single nanocrystals of anatase-type $TiO_2$ prepared from layered titanate nanosheets: Formation mechanism and characterization of surface properties. *Langmuir* **2007,** 23, (23), 11782-11790.

46. Colon, G.; Sampedro, P.; Fernandez-Garcia, M.; Chen, H. Y.; Hanson, J. C.; Rodriguez, J. A., Synthesis, characterization, and photodegradation behavior of single-phase anatase $TiO(_2)$ materials synthesized from Ti-oxychloride precursors. *Langmuir* **2008,** 24, (19), 11111-11118.

47. Langford, J. I.; Wilson, A. J. C., Scherrer after 60 years: Survey and some new results in determination of crystallite size. *J. Appl. Crystallogr.* **1978,** 11, (APR), 102-113.

48. Meng, Z. Y.; Hashmi, S. M.; Elimelech, M., Aggregation rate and fractal dimension of fullerene nanoparticles via simultaneous multiangle static and dynamic light scattering measurement. *Journal of Colloid and Interface Science* **2013,** 392, 27-33.

49. Filippov, A. V.; Zurita, M.; Rosner, D. E., Fractal-like aggregates: Relation between morphology and physical properties. J. Colloid Interd. Sci. **2000,** 229, (1), 261-273.

50. Bushell, G. C.; Yan, Y. D.; Woodfield, D.; Raper, J.; Amal, R., On techniques for the measurement of the mass fractal dimension of aggregates. *Adv. Colloid Interface Sci.* **2002,** 95, (1), 1-50.

51. Wu, H.; Lattuada, M.; Sandkuhler, P.; Sefcik, J.; Morbidelli, M., Role of sedimentation and buoyancy on the kinetics of diffusion limited colloidal aggregation. *Langmuir* **2003,** 19, (26), 10710-10718.

52. Wei, D.; Wu, H.; Xia, Z. B.; Xie, D. L.; Zhong, L.; Morbidelli, M., Monitoring coalescence behavior of soft colloidal particles in water by small-angle light scattering. *Colloid Polym. Sci.* **2012,** 290, (11), 1033-1040.

## 2.6 Supplementary Information

### *2.6.1 Preparation of Nanoparticles from $TiCl_4$*

$TiCl_4$ (1 ml, 9.12 mmol) was added slowly to anhydrous ethanol (5ml) in a Schlenk tube producing a pale yellow solution. Benzyl alcohol (20 mL) was then added and the solution was heated to 80 ˚C under different atmospheric conditions with continuous stirring, the growth of the nanoparticles was monitored over time using DLS. The reaction was either left open to the surrounding atmosphere, kept under an inert argon atmosphere or under a $H_2O$ saturated argon atmosphere created by bubbling the argon through a vacuum trap containing deionised $H_2O$ at a flow rate of 100 mL of gas per minute prior to entering the reaction vessel. The reaction was also performed using a Radleys Carousel 12 plus Reaction Station (Radleys, UK) for comparison with the synthesis of the nanoparticles using titanium tetraalkoxide precursors.

### *2.6.2 Thermal growth phase at Ti/Cl = 0.5*

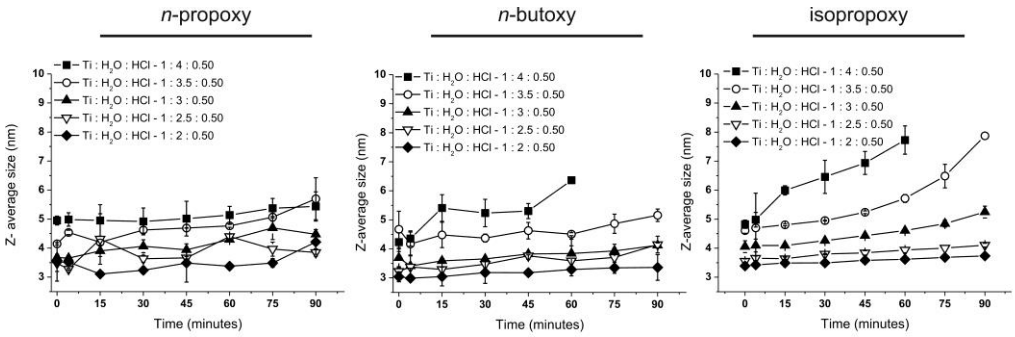

**Figure 2.6.2-SI-1** Evolution of size (T = 80ºC) as a function of time and of the amount of water for particles prepared from Ti(*n*OPr)$_4$ (*left*), Ti(O$^i$Pr)$_4$ (*centre*) and Ti(OBu)$_4$ (*right*) at a Cl/Ti = 0.5 molar ratio. From the comparison with Figure 2.3.3-1.

### 2.6.3 *Nanoparticle growth: surface condensation model*

In this model primary nanoparticles would grow in size via the condensation of monomeric titanium alkoxides onto their surface. The amount of titanium centres condensed in the time unit for a nanoparticle i.e. its rate of volume increase, would therefore be proportional to the number of available surface sites, i.e. to its surface area: $\frac{dV_i}{dt} = Kr_i^2$, which can be rearranged as $\frac{dr_i}{dt} = K'$. The integration leads to the following expression for the number average radius $R = \sum_i n_i \cdot r_i$ and the radius variance $\sigma^2 = \sum_i n_i \cdot (r_i - R)^2$ ($n_i$ is the number of particles of size $r_i$): $R = R_0 + Kt$ and $\sigma^2 = {\sigma_0}^2$ , where $R_0$ and ${\sigma_0}^2$ are the average radius and variance at time 0, respectively.

The experimental values of R and $\sigma^2$ can be calculated from DLS data (Figure 1SI). The number distributions of particle sizes were extracted from the intensity distributions by using the transformation $n_i = \frac{I_i}{{d_i}^6}$ (where $I_i$ are the percent scattered intensities of the intensity distribution curves and $d_i$ the diameters) followed by normalization. This transformation is accepted for Rayleigh scatterers smaller than about $\lambda_0/10$ (or ~50 nm, as $\lambda_0$ is the light wavelength) as in this case[24]. While the rather large noise made it difficult to establish whether the particle size followed a linear time dependency, the variance clearly increased with time.

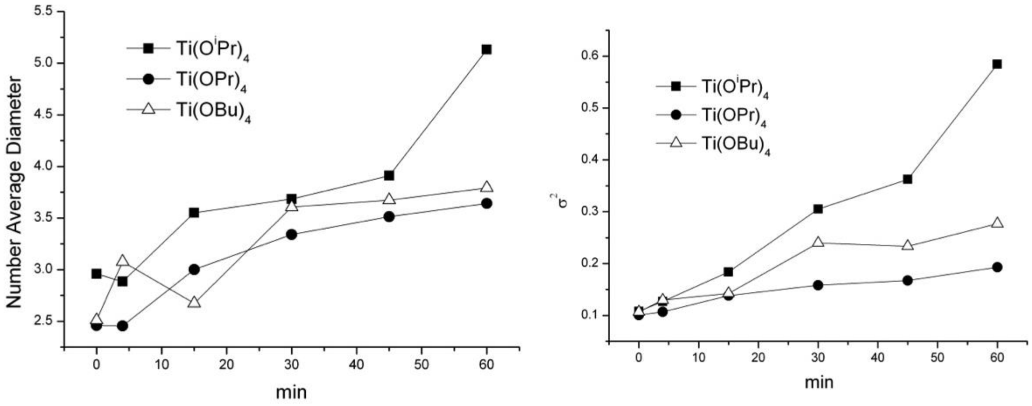

**Figure 2.6.3-SI-1** Number average diameter (*left*) and variance (*right*) of the distribution curves versus reaction time,. Particles synthesised from different precursors at a Ti : $H_2O$ : HCl molar ratios of 1:4:1.17.

The inability to apply the above model points to a mechanism of growth based on the aggregation of the primary particles.

### *2.6.4 Static Light Scattering (SLS) measurements*

Nanoparticles were synthesised as previously described, using 0.456 M $Ti(O^iPr)_4$ in benzyl alcohol, keeping the $Ti/H_2O$ molar ratio constant (1:4) and changing the Ti/HCl one (1:1.17, 1, 0.75 and 0.5). The particles were analysed at 0, 30 or 60 minutes of incubation at 80°C. The fractional dimension of each system was obtained by plotting the log(1/I) against the log*q* where I is the scattering intensity and *q* the scattering vector; the angle was changed by 5° increments in the interval 30-90°.

The system produced with 1 : 4 : 1.17 $Ti:H_2O:HCl$ molar ratio after 60 minutes at 80°C was also analysed in a Zimm plot, obtained by measuring the scattering intensity at variable angles (30-140° at 10° increments) for different concentrations of the nanoparticle dispersion (5.3, 4.0, 2.7 and 1.3 mg $mL^{-1}$). Smaller particles were not analysed due to problems in estimating their exact concentration (difficult precipitation).

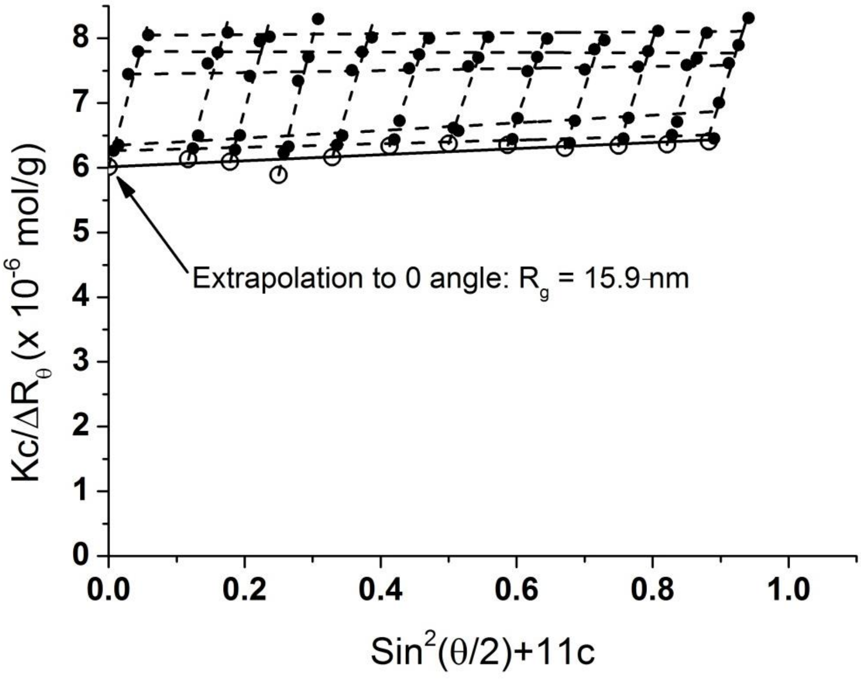

**Figure 2.6.4-SI-1** Zimm plot in benzyl alcohol dispersion for nanoparticles derived from $Ti(O^iPr)_4$ at 1 : 4 : 1.17 $Ti:H_2O:HCl$ molar ratio after 60 minutes at 80°C.

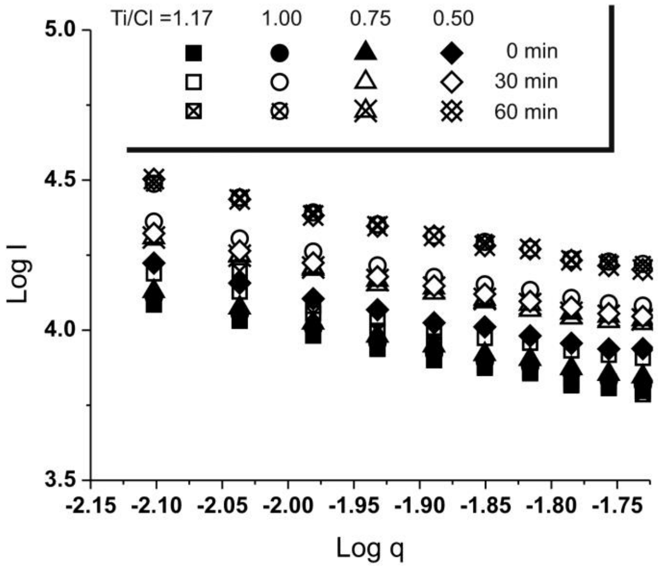

**Figure 2.6.4-SI-2** Log-log plot of scattering intensity vs. scattering vector for from Ti(O$^i$Pr)$_4$-derived nanoparticles produced at 1 : 4 : 1.17 Ti:$H_2O$:HCl molar ratio at different points of the thermal treatment at 80°C. All systems showed the same slope of 0.75, which indicates a relationship not based on the fractal dimension of the colloidal objects (which is by definition >1).

# 3 Effect of ligand adsorption and PEGylation on the photoactivity of anatase nanoparticles

Christopher J. Cadman[a], Francesco Cellesi[a] and Nicola Tirelli[*b,c]

[a] School of Pharmacy and Pharmaceutical Sciences, University of Manchester, Oxford Road, Manchester, M13 9PT, United Kingdom

[b] School of Materials, University of Manchester, Oxford Road, Manchester, M13 9PT, United Kingdom

[c] School of Medicine/Institute of Inflammation and Repair, University of Manchester, Oxford Road, Manchester, M13 9PT, United Kingdom

[*]to whom correspondence should be addressed:

Prof. Nicola Tirelli, Institute of Inflammation and Repair, University of Manchester, Oxford Road, Manchester, M13 9PT, United Kingdom

Tel: +44 161 275 18 02

Email: Nicola.tirelli@manchester.ac.uk

## Abstract

Fully water-dispersable and ligand-free titania nanoparticles with a 10 nm average size were used as a platform to develop functional photo-oxidative nano-systems with a possible application in photodynamic therapy. The main aim of this study was the development of a robust approach for the decoration of these nanoparticles with poly(ethylene glycol) chains (PEGylation) and the characterization of their photocatalytic activity.

The titania nanoparticles were decorated with ligands that featured catechol or phosph(on)ate groups as titania-binding heads; in addition to ligands containing PEG chains, other structures (primary amines or carboxylic acids) were also evaluated to provide colloidal systems stabilized via electrostatic interactions. While no significant differences were highlighted in the ligand densities achievable with the two different head groups, they provided a dramatically different photochemical behaviour; independently on their chemical structure, on their surface density and on the pH, catechol ligands were completely inactive in the oxidation of a model dye (methylene blue), whereas phosph(on)ates increased the efficiency in the generation of Reactive Oxygen Species (ROS) in comparison to uncoated particles, and showed a significant dependency on the chemistry and surface density of the ligands and on pH.

## 3.1 Introduction

The (electro)optical properties of titanium dioxide make this material popular in a number of applications, e.g. photovoltaics[1], water purification[2] and sun screening[3], that make use of its relatively low band gap. Anatase is the most photoactive of the three common crystalline forms of $TiO_2$, and presents a band gap of 3.26 eV[4], which corresponds to an activation wavelength of 385 nm. Upon absorbing of appropriate photons, electron-hole pairs are formed and, in the absence of recombination, eventually reach the surface of the crystal. In an aqueous environment the electrons and holes are free to react with $H_2O$ and dissolved $O_2$ producing a number of reactive oxygen species (ROS) including $^{\bullet}OH$, $O_2^-$, $^{\bullet}HO_2$, $H_2O_2$ and $^1O_2$[4]. Since the ROS production is a surface phenomenon, it is not surprising that nano-structured $TiO_2$ (most often in the region of 7 – 40 nm) appears to provide the highest efficiency[5-7]. These photo-oxidation processes are at the basis of the commercial uses of titanium dioxide as a photo-oxidation catalyst, e.g. in self-cleaning windows[8] or removal of dyes or other organic compounds[9] from water. However, they also offer an interesting possibility of application for $TiO_2$ in the biomedical field, where its well-known biocompatibility can be flanked by its use for photodynamic therapy (PDT)[10] for the light-induced ROS generation and the corresponding reduction in viability of target (e.g. tumoral) cells[11].

In view of the *in vivo* administration of nano-sized $TiO_2$, there are some key hurdles to overcome. Firstly, prevention of agglomeration: titania has an isoelectric point in the region of pH = 5-6, and its nanoparticles are most typically kept in acidic environment to confer them electrostatic stabilization; however, a different form of stabilization is needed in a physiological environment. Secondly, minimization of protein adsorption: the occurrence of this phenomenon in biological fluids typically determines the uptake of oxide particles by sentinel cells (resident macrophages) and their clearance from the bloodstream[12]. These two targets can in principle be achieved through the presence of a hydrophilic, protein-repellent surface layer, and poly(ethylene glycol) (PEG) is the most popular candidate for this application, which can decorate the surface of titania nanoparticles via the use of appropriate ligands, e.g. catechols[13]. Catechols and also phosphates/phosphonates are indeed among the most popular ligands used for the surface modification of $TiO_2$[14-16]. Catechols shift the $\lambda_{max}$ of the system from ~380 nm to 435 nm therefore shifting the energy required for $TiO_2$ photoactivation towards the visible light region[17], and are therefore commonly used in dye sensitized solar cells where they act as charge transfer bridges[18]. Phosphonates are also increasingly used as ligands especially in the field of biomaterials[16]; in particular recent reports have shown promising results into the enhancement of titania's photoactivity upon surface modification with phosph(on)ates[19, 20].

In this study we have therefore aimed to draft a comparison between:

A) the adsorption behaviour of catechol- and phosph(on)ate-based ligand structures (Scheme 3.1.1) on novel titania nanoparticles produced through a non-aqueous process and characterized by a very low size (also below 10 nm) and therefore by a high surface area. Specifically, we have used PEGylated ligands and control structures with ionisable groups capable to provide electrostatic stabilization; in this phase, we have aimed to optimize the ligand density on the nanoparticles that would maximize colloidal stability and minimize toxic effects on cells.

B) the photo-oxidation activity of the resulting nanoparticles. In particular, we wished to highlight with combination of ligand structure (e.g. catechols vs. phosph(on)ates) and related chemical environment (highly an/cationic environment, or PEG layers) can allow to retain or maximize titania photocatalytic activity.

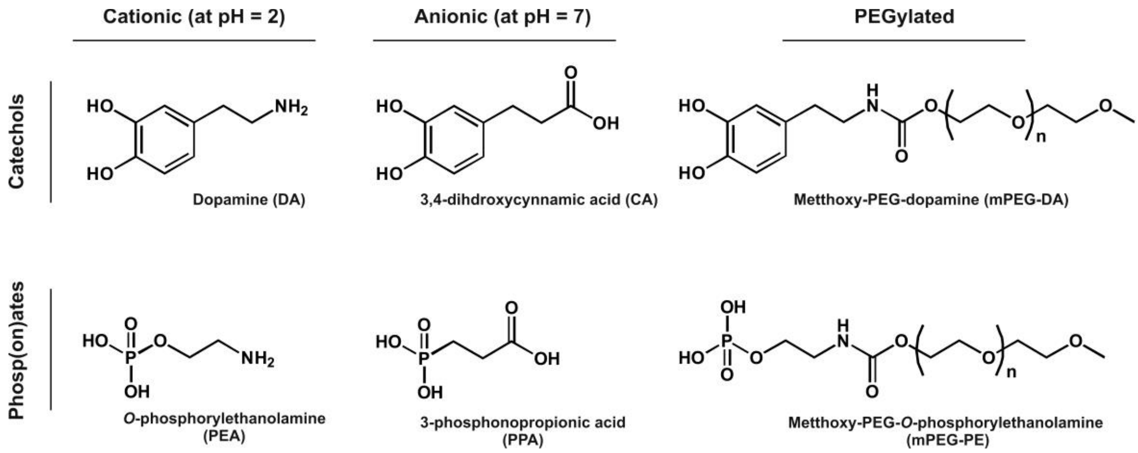

**Scheme 3.1-1** Structures of the ligands used in this study to decorate $TiO_2$ nanoparticles.

## 3.2 Experimental section

### *3.2.1 Materials and methods*

Titanium (IV) isopropoxide ($Ti[OCH(CH_3)_2]_4$, purity ≥97.0%), poly(ethylene glycol) methyl ether (average $\overline{M_n}$ ~ 2000 g/mol), 4-nitrophenyl chloroformate (**PNP**, purity ≥97.0%), dopamine hydrochloride (**DA**), triethylamine (**TEA**, purity ≥99.0%), 3,4-dihydrohydroxycinnamic acid (**CA**) (purity 98%), *O*-phosphorylethanolamine (**PEA**, ≥99.0%), 3-phosphonopropionic acid (94%), benzyl alcohol (anhydrous, purity 99.8%), 37% hydrochloric acid solution, 0.1 N hydrochloric acid solution and 3-(trimethylsilyl)-2,2',3,3'-tetradeuteropropionic acid were supplied by Sigma-Aldrich (Dorset, UK). Sephadex G-25 (medium) as bought from GE Lifecare Health Sciences (Buckinghamshire, UK). Diethyl ether (anhydrous), toluene, dichloromethane and N,N-dimethylformamide (**DMF**) were supplied by Fisher Scientific UK Ltd. All materials were used as received from the supplier without any further purification. Water was pre-deionised and further purified by a Milli-Q system (Millipore, UK).

### *3.2.2 Physico-chemical characterization*

*Dynamic Light Scattering (DLS) and ζ-potential analysis.* DLS measurements were performed using a Zetasizer Nano ZS instrument (Malvern Instrument Ltd., U.K.). A Malvern autotitrator MPT-2 was connected to the Zetasizer for ζ-potential measurements over a range of pH values. Raw data were processed by Malvern DTS software. Quartz cuvettes with a path length of 10 mm were used for size analysis and disposable capillary flow cells were used for zeta potential analyses. The stability of the nanoparticles at physiological pH, as a function of surface ligand concentration, was monitored by DLS. Variable aliquots of ligands (concentration = 2 $molL^{-1}$ for the small molecular weight free ligands and 65 $mmolL^{-1}$ for the PEGylated ligands) were added to 50 µl of a 2 mg/mL nanoparticle dispersion in deionized water adjusted to pH = 2 (0.1 M HCl). For PEGylated ligands the surface grafting density was varied between 0.1 – 65 µmol per mg of $TiO_2$ and for free ligands the grafting density was varied between 0.1 – 2000 µmol per mg of $TiO_2$. The solutions were then allowed to stabilise for 30 minutes and then neutralised with a sodium carbonate bicarbonate buffer (10% v/v 0.1 M sodium carbonate and 90% 0.1 M sodium bicarbonate, pH = 8). The ζ-potential was monitored as a function of pH employing the autotitrator, employing particles with a constant ligand grafting density of 5 µmol /mg of $TiO_2$.

*Infrared spectroscopy (ATR-IR).* IR spectra were recorded in ATR mode on a Tensor 27 Bruker spectrometer (Bruker UK Limited, UK) equipped with a 3000 Series TM High Stability Temperature Controller with RS232 Control (Specac, UK).

*Fluorescence spectroscopy.* Fluorescence spectra were recorded on a Biotek, Synergy 2 plate reader. For studies using fluorescamine the excitation and emission filters were set at 360 ± 40 and 460 ± 40 nm, respectively.

*$^1$H NMR spectroscopy.* Spectra were recorded with a 300 MHz Bruker spectrometer (Bruker UK Limited, UK); XWIN-NMR software was used to process the data. NMR samples were prepared in either $CDCl_3$ or $D_2O$ at a concentration of 1 wt.%.

### *3.2.3 Preparative procedures*

**Anatase nanoparticles.** In a Radleys Carousel 12 plus Reaction Station (Radleys, UK) 2.59 g (9.12 mmol) of $Ti(O^iPr)_4$ were added under argon to 20 mL of benzyl alcohol containing water and hydrochloric acid, respectively in 4:1 and 1.17:1 molar ratios to the titanium precursor; the acid concentration was calculated on the basis of the molar concentration of HCl in its 37 % wt. water solution. The reaction was heated at 80 °C and then stopped when the average diameter of the nanoparticles reached 10 nm. The nanoparticles were then precipitated in 150 mL of diethyl ether and centrifuged (3500 rpm, 5 mins). The supernatant was decanted and the resulting white solid was washed twice with 50 mL diethyl ether. The precipitate was then re-dispersed in 20 mL of a 50:50 w/w water-ethanol solution at pH = 2 (obtained with 0.1 N HCl). The resulting dispersion was dialysed against deionized water (pH = 2 through HCl) using a dialysis membrane with a MWCO of 10,000 g/mol. The final concentration of the nanoparticle suspension (typically 5 mg/mL) was calculated by neutralising a 1 mL sample of the solution using 1 N $Na_2CO_3$, inducing precipitation, followed by centrifugation (3,500 rpm, 5 mins), decantation and repeated washings with deionized water prior to freeze drying.

**4-nitrophenylcarbonate-terminated poly(ethylene glycol) (mPEG-pNP).** 10 g (~ 5 mmol) of poly(ethylene glycol) methyl ether were dissolved in 200 mL of toluene under argon atmosphere. The solution was refluxed for three hours through a Soxhlet extractor filled with activated molecular sieves (3 Å) to remove any traces of water present. The reaction was cooled to 0°C and TEA (3 molar equivalents per OH group) was added. Subsequently, 20 mL of a PNP (2 equivalents per OH group) solution in toluene were added drop wise to the polymer solution. The solution was left to react overnight and the following day the precipitate was filtered out and the solvent was evaporated until ~ 20 mL of a dense liquid was obtained. The polymer was then precipitated in 200 mL of cold diethyl ether and collected by centrifugation. The white precipitate was then redissolved in 50 mL of dichloromethane, condensed *via* rotary evaporation and re-precipitated with diethyl ether. The precipitate was finally washed with diethyl ether and stored under argon. Yield: 86 % wt. Conversion: 95.3 % mol (from $^1$H NMR: PEG methoxy group vs. aromatic protons).

$^1$H NMR ($CDCl_3$)**:** $\delta$ = 3.4 (s, 3H, O-**$CH_3$**), 3.6 (m, O-**$CH_2$**-**$CH_2$**-O), 3.8 (t, 2H, –C**$H_2$**-$CH_2$-OC(=O)O), 4.4 (t, 2H–$CH_2$-C**$H_2$**-OC(=O)O), 7.4 (d, 2H, aromatic –CH in ortho to phenol) and 8.3 (d, 2H, aromatic –CH in ortho to nitro group) ppm.

ATR-IR (thin film): 3082 ($\nu$ CH, aromatic ring) 2977 ($\nu_{as}$ $CH_3$), 2945 ($\nu_{as}$ $CH_2$), 2883 ($\nu_s$ $CH_2$), 1766 ($\nu$ C=O), 1529 ($\nu_{as}$ $NO_2$), 1396 ($\nu_s$ $NO_2$), 1097 ($\nu_{as}$ C-O-C) and 842 (aromatic $\delta$ out of plane CH) $cm^{-1}$

**Dopamine-terminated poly(ethylene glycol) (mPEG-DA).** DA (2 equivalents per nitrophenyl group) and TEA (5 equivalents per nitrophenyl group) were dissolved in 50 mL of DMF under argon. A solution of 5.0 g mPEG-pNP (~ 2.3 mmol) in 50 mL of DMF was added and left to react for 3 hours; it was then concentrated down to a ~ 20 mL volume *via* rotary evaporation and precipitated in 200 mL of cold diethyl ether. The white precipitate was then centrifuged, decanting off the supernatant, redissolved in a small amount of dichloromethane, precipitated again and finally washed twice with diethyl ether. The precipitate was dissolved in 20 mL of degassed water and dialysed using a dialysis membrane with a MWCO of 1000 gmol$^{-1}$ against water under constant argon bubbling. The final solution was then freeze dried and stored under argon. Yield: 84 % wt. Conversion: ~ 100 % mol (from $^1$H NMR: PEG methoxy group vs. aromatic protons).

$^1$H NMR ($D_2O$)**: mPEG-DA:** δ **=** 2.7 (t, 2H, Ar-$CH_2$-C**$H_2$**-NH), 3.3 (t, Ar-C**$H_2$**-$CH_2$-NH), 3.4 (s, 3H, O-**$CH_3$**), 3.7 (m, O-C**$H_2$**-C**$H_2$**-O), 6.7 (d, 1H, aromatic –CH in position 6), 6.8 (s, 1H, aromatic –CH in position 2), 6.9 (d, 1H, aromatic –CH in position 5) ppm

ATR-IR (thin film)**:** 3079 (ν CH, aromatic ring), 2944 ($\nu_{as}$ $CH_2$), 2885 ($\nu_s$ $CH_3$), 2858 ($\nu_s$ $CH_2$), 1714 (ν C=O), 1097 ($\nu_{as}$ C-O-C) and 841 (aromatic δ out of plane CH) cm$^{-1}$

**Phosphate-terminated poly(ethylene glycol) (mPEG-PEA).** The procedure is analogous to the previous one, but by replacing dopamine with *O*-phosphorylethanolamine (PEA) it was also necessary to introduce a phase transfer cation to enhance the solubility of the latter in organic solvents. A solution of PEA in 10 mL deionized water (3.5 molL$^{-1}$) was brought to pH = 7 using tetrabutylammonium hydroxide (TBA) and freeze dried, producing a solid soluble in DMF. PEA (2 equivalents per PNP group) and TEA (5 equivalents per PNP group) were dissolved in 50 mL of DMF under argon and the reaction was performed under the conditions previously described. After synthesis, in order to remove TBA, the polymer was first dialysed against a NaCl solution (0.2 molL$^{-1}$) using a dialysis membrane with a MWCO of 1,000 gmol$^{-1}$ for two days and subsequently against deionized water for a further three days. The product solution was then freeze dried and stored under argon. Yield: 79 % wt. Conversion: 93.5 % mol (from $^1$H NMR: PEG methoxy group vs. resonance at 3.3 ppm).

$^1$H NMR ($D_2O$)**: mPEG-PEA:** δ = 3.3 (t, 2H, PO-$CH_2$-C**$H_2$**-NH), 4.1 (t, 2H, PO-C**$H_2$**-$CH_2$-NH), 3.4 (s, 3H, O-**$CH_3$**), 3.7 (m, O-C**$H_2$**-C**$H_2$**-O) ppm

ATR-IR (thin film): 3595-3182 (ν OH), 2947 ($\nu_{as}$ $CH_2$), 2885 ($\nu_s$ $CH_3$), 2864 ($\nu_s$ $CH_2$), 1712 (ν C=O), 1342 (ν P=O) 1095 ($\nu_{as}$ C-O-C) and 960 (ν P-O) $cm^{-1}$

### *3.2.4 Surface functionalization of nanoparticles*

All water solutions/dispersions were prepared adjusting the pH of deionized water to pH = 2 with the help of concentrated HCl.

**Spectrophometric analysis of catechol adsorption.** Variable amounts of a water solution at pH 2 of dopamine (2 M) or mPEG-DA (65 μM) were added to 50 µL of a 0.5 mg/mL water dispersion of anatase nanoparticles in each well of a 96-well plate to provide a final concentration of 0.1 – 2000 µmol of dopamine or 0.1-65 µmol of mPEG-DA per mg of $TiO_2$. The total volume of each well was brought up to 250 µl with water at pH = 2. Absorption spectra were recorded in the 300-700 nm spectral range using a Biotek, Synergy 2 plate reader; the scattering contribution to each spectrum was fitted with an exponential function and subtracted to provide the final absorbance readings. The nanoparticles were then purified *via* gel permeation chromatography (Sephadex G25 medium (GE life sciences)).

**$^1$H NMR analysis of phosphoryl ethanolamine and dopamine adsorption.** 1 mL of a 10 mg/mL solution containing either phosphorylethanol amine or dopamine was added to 1 mL of a 13 mg/mL nanoparticle dispersion (both at pH = 2), providing for a stock dispersion of nanoparticles coated with a similar surface grafting density for the two ligands (≈ 5 μmol of ligand per mg of $TiO_2$). Variable amounts of the stock dispersion and of the 10 mg/mL ligand solution were mixed in NMR tubes for a constant final volume of 400 μL; the resulting systems presented therefore a variable amount of titania and a constant overall amount of ligand. After overnight equilibration, an insert containing 10 mg/mL 3-(trimethylsilyl)-2,2',3,3'-tetradeuteropropionic acid in $D_2O$ as a standard was introduced in the tube and the $^1$H NMR spectra were acquired. The adsorption of the ligand on the nanoparticle surface was estimated by measuring the decrease in the ligand proton signals as a function of the nanoparticle concentration, in reference to the signal from the standard.

**Fluorescent labelling of nanoparticles.** This operation was performed immediately before the use of these particles in cell culture. The nanoparticles were first coated with mPEG-DA as described above (5 μmol per mg of $TiO_2$). Appropriate volumes of a 30 mM solution of dopamine (corresponding to 2.4 nmol per mg of $TiO_2$) was added to the dispersion and was left to stir for 1 hour, after which fluorescamine was added (1.6 nmol per mg of $TiO_2$) and stirring was continues for 3 hours. The dispersion was then dialysed (MWCO = 10,000 Da) and diluted to the desired concentrations in full Dulbecco's modified eagle's medium (DMEM).

### *3.2.5 Photo-oxidative activity of nanoparticles*

In all experiments, an Omnicure® S1000 was used as a light source, equipped with a 250-450 nm filter and an optical fibre with an internal diameter of 5 mm (Omnicure® liquid light guide); the output power at the end of the fibre was kept at 10 $mW/cm^2$ and constantly monitored. The end of the fibre was connected to a 10 cm glass condenser placed vertically on a 25 mL two-neck round bottomed flask and the entire assembly was covered with aluminium foil to avoid light dispersion. Through the second neck, the content of the flask was constantly sampled through a flow-through cuvette, allowing the constant monitoring of the absorbance at 665 nm (Perkin-Elmer Lambda 25 UV/vis spectrometer). In a general procedure, 5 mL of 8 μg/mL (0.025 mM) methylene blue aqueous solution containing nanoparticles at a concentration in a range 0.1 – 2.0 mg/mL were introduced into the flask. Measurements were performed at pH = 2 (directly after the adsorption of ligands on nanoparticles) or at pH = 7 (neutralising the adsorption environment via the addition of a bicarbonate buffer (10%v/v 0.1M sodium carbonate and 90% 0.1M sodium bicarbonate, pH = 8)).

For all experiments, the concentration of methylene blue was calculated from its extinction coefficient (17,088 $Lmol^{-1}cm^{-1}$) and its time evolution was fitted with a pseudo first order model ($lnC(t) = -k_{obs}t + lnC_0$; see Supplementary Information, Figure 3.6.2-SI-1).

Please note that in most experiments, the nanoparticles were used at a concentration of 0.2 mg/mL: it was observed that $k_{obs}$ increased (more or less) linearly with the nanoparticle concentration only up to less than 1 mg/mL, and then plateaus due to the increased scattering by nanoparticles (Figure 3.6.2-SI-2).

In selected experiments, the methylene blue photo-oxidation was performed in the presence of selective ROS quenchers, using nanoparticles containing 5 μmol of ligand per mg of $TiO_2$. Methanol (MeOH – scavenging positive holes), dimethyl sulfoxide (DMSO - hydroxyl radicals), *p*-benzoquinone (BQ – superoxide anion) and sodium azide ($NaN_3$ - singlet oxygen) were all used at a 0.025 M concentration (1000 times higher than that of methylene blue).

### *3.2.6 Biological investigations*

RAW 246.7 macrophages cultured on TCPS in standard conditions for cell culture (humidified atmosphere, 37°C, 5% $CO_2$) were detached with a cell scraper after reaching 70% confluency. The resulting cell suspension was centrifuged (1,000 rpm for 5 min, room temperature), the supernatant was discarded and the pellet resuspended in ice-cold phosphate buffered saline (PBS). The cells were further centrifuged under the same conditions, the supernatant was discarded and the cell pellet resuspended in 5 mL of full medium. The cells were then counted using a counting chamber (bright-line haemotocytometer, Hausser scientific, PA, USA) and seeded in slide-flasks (9 $cm^2$, Nunc) or in 96 well plates at 30,000 cells per $cm^2$ in full DMEM medium (10% fetal bovine serum (FBS), 1% L-glutamate, 1% Penstrep) for 24 h in standard conditions for cell culture. **Cytotoxicity.** The time/dose dependency of the viability of RAW 246.7 macrophages on the concentration of mPEG-DA coated nanoparticles (10, 50, 100 and 250 μg/mL; density of 5, 20 or 40 μmol of PEG per mg of titania) was assessed at 2, 4 and 24 hours. After seeding the cells in a 96 well plate and leaving them to attach for 24 hours the medium was carefully removed, the cells were washed with ice-cold PBS and the medium was replaced with coated nanoparticles at the desired concentration, leaving the cells in contact with the nanoparticles for 2, 4 or 24 hours. After removing the medium, the cells were washed with ice-cold PBS and new medium was added containing 5% MTS reagent. After 2 hours of incubation the absorbance of each well was read at λ

= 562 nm. The MTS containing buffer was then removed, again the cells were washed and then lysis buffer (100 µL, 0.5 %) was added to each well. The cells were incubated for 15 minutes at room temperature and the protein content of each well was ascertained using a standard bicinchoninic acid assay (BCA) kit following the suppliers instructions. The viability of the cells was assessed by normalising the MTS readings with the protein content of each well.

**Nanoparticle uptake.** A) The amount of uptaken mPEG-DA coated nanoparticles (5, 20 or 40 µmol of polymer per mg of titania) was assessed upon 24 h incubation of RAW macrophages using suspensions of fluorescently labelled nanoparticles (concentration of titania = 6, 12, 25 and 50 µg/mL). After careful removal of the medium, the cells were gently washed with ice-cold PBS and lysed with 0.5% Triton X-100 in PBS for 15 min at room temperature. The amount of internalized material was estimated on the basis of the fl-100 in PBS for 15 min at room temperature ($e_{exc}$ = 485 nm and $\lambda_{em}$ = 528 nm), using the fluorescence of the nanoparticles in cell lysates as a calibration. The fluorescence was then normalised against the protein content of each well *via* the BCA assay to attain the amount of uptaken nanoparticles (expressed in mg of titania) per mg of protein.

B) The intracellular localization of mPEG-DA coated nanoparticles was followed via confocal microscopy on cells cultured in slide-flasks. After culturing the cells with nanoparticles, as described in A, the medium was carefully removed from the slide flask and replaced with full medium containing mPEG-DA coated nanoparticles which were also labelled with fluorescamine as described previously. After 24 hours of incubation, the medium was carefully removed and the cells were washed with ice-cold PBS and fixed with 4% paraformaldehyde (PFA) in PBS for 30 min at room temperature. The cells were then incubated with DAPI (5 mg/mL) in PBS for 1 hour followed by washing and further incubation with LysoTracker Red (50 nM); when using all probes the cells and solutions were kept in the dark. The slides were then washed further and mounted with anti-fade mounting gel. Images were acquired on a Delta Vision RT (Applied Precision) restoration microscope.

## 3.3 Results and Discussion

### 3.3.1 *Nanoparticle surface functionalization*

The synthesis of the $TiO_2$ nanoparticles has been previously optimised to provide narrowly dispersed, ligand-free nanoparticles with a Z-average size of 10 nm or less. We have here used two different methods of surface functionalization to decorate the particles with PEG residues and other chemical functionalities, specifically focusing on potentially anionic (carboxylates) and cationic (primary amines) groups, which could be used as control systems in order to identify or exclude possible roles of the PEG structure in the modulation of the ROS photogeneration. The two functionalization methods are based on the use of catechols and phosph(on)ates as titania-binding ligands.

The catechol- and phosphate-terminated PEGylated ligands (mPEG-DA and mPEG-bDA) were synthesized by activating PEG ($\overline{M_n} \approx$ 2000 gmol) with *p*-nitrophenylcarbonate and reacting it with the primary amine groups of, respectively, dopamine and *O*-phosphorylethanolamine; the primary amine- and carboxylate-containing ligands (resp. DA and PEA, and CA and PPA) are commercially available. Please note that while PPA bears a phosphonate group, PEA and mPEG-PEA contain phosphate groups; we have been working under the hypothesis of a negligible difference between the adsorption of phosphates and phosphonates[21, 22].

For what attains to catechols, their adsorption behaviour on uncoated (“naked”) anatase nanoparticles has been already studied in considerable detail, although on larger and more agglomerated objects (average size of 35 nm)[23]. Typically, catechol adsorption is associated with the development of an intense absorption in the 400-500 nm region (Figure 3.3.1-1 A); the colour is associated to chelate complexes (both catechol hydroxyl groups interacting with the same titanium atom), which are formed together with bridged complexes (one catechol interacting with two metal atoms, colourless in the visible region).

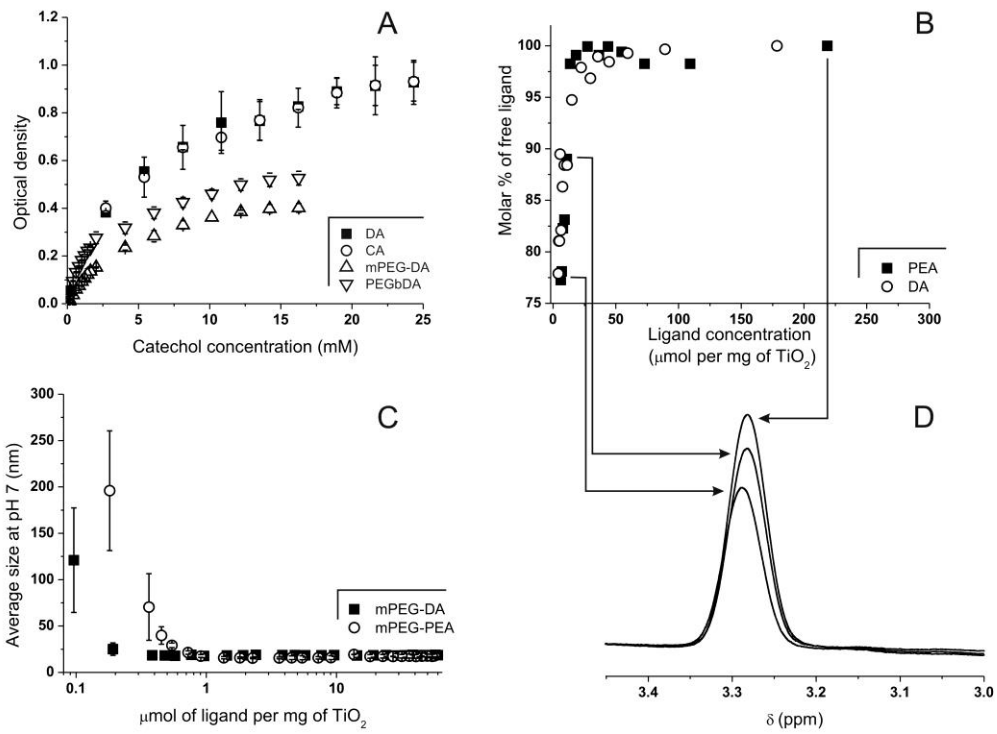

**Figure 3.3.1-1** *A*. Optical density as a function of ligand concentration for the four catechol-based systems. Nanoparticle concentration: 0.26 mg/mL, pH = 2. Please note that the contribution from nanoparticle scattering was removed from the optical density (an example of scattering-corrected spectra is provided in Supplementary Information, Figure 2SI). ***B***. Molar percentage of free ligand as a function of the ligand to titania ratio for DA and PEA; the experiments used a fixed concentration of ligand (10 mg/mL) s in $D_2O$ (pH =2), measuring the integral of NMR resonances as a function of the concentration of nanoparticles (see D). ***C***. Z-average size of nanoparticles in deionized water at pH = 7 upon coating with different amounts of PEGylated ligands; the ligand density below which the size increases is a measure of the colloidal stability of the system. ***D***. $^1$H NMR resonance of PEA ($\delta = 3.29$ ppm, $CH_2$ next to the primary amine; $\delta = 2.88$ ppm was used for DA) at a concentration of 10 mg/mL and in the presence of titania nanoparticles at three different concentrations.

The use of smaller (10 nm) nanoparticles did not appear to qualitatively modify the adsorption of these ligands; for example, the same trends were recorded in the comparison of the adsorption of dopamine, mPEG-DA and PEG-bDA (a double catechol-terminated PEG used here only as for comparison purposes): at “full” coverage, the relative occupancy of surface sites decreased, while the fraction of chelating catechols and the adsorption constant increased in the series (see Supplementary Information, section 1, Table 3.6.1-SI-1 and Figure 3.6.1-SI-1). It is also noteworthy that the chemical functionality did not appear to have much influence in the adsorption, since dopamine (primary amine) and 2,3-dihydrocinnamic acid (carboxylic acid) showed an identical adsorption behaviour. In terms of achievable ligand density, phosph(on)ates appear to behave rather similarly to catechols. Due to the absence of any significant spectra change, we have monitored their adsorption through the disappearance of peaks from the ligands' NMR spectra (sharp decrease in T2); this has showed virtually indistinguishable isotherms for catechols and phosph(on)ates (Figure 3.3.1-1 B and 3.3.1-1 D), which hint at a similar occupancy of surface sites. This is further confirmed by the similar amounts of PEGylated ligands necessary to achieve colloidal stability at pH = 7: > 0.2 μmol/mg of $TiO_2$ mPEG-DA and > 0.5 μmol/mg of $TiO_2$ for mPEG-PEA (Figure 3.3.1-1 C). The slight difference is probably to ascribe to a slightly lower surface density of the phosphates due to reciprocal electrostatic repulsion (they are anionic). It is noteworthy that all ligands were adsorbed in quantitative fashion at least up to a dose of 50 μmol/mg of $TiO_2$: in dispersions purified through gel filtration, the comparison between overall solid content obtained from freeze drying, and titania concentration estimated from scattering experiments (the scattering intensity at 632 nm is not affected by surface functionalization) provides ligand/titania ratios statistically indistinguishable from the theoretical ones.

The size of the nanoparticles (Figure 3.3.1-2, Table 3.3.1-1) showed a negligible increase when low molecular weight ligands were used, with a typical Z-average size of 10-12 nm; a moderate increase was recorded with PEGylated monofunctional ligands (mPEG-DA and mPEG-PEA) with a typical Z-average size 20 nm, which would suggest the presence of a 4-5 nm-thick hydrated PEG corona.

The substantial similarity between catechols and phosph(on)ates in terms of ligand surface density and stability was further confirmed by the virtually identical dependency of the ζ-potential of the correspondingly coated nanoparticles on pH (Figure 3.3.1-3, left): using either catechol or phosphate ligands PEGylated nanoparticles were substantially neutral and stable at any pH, while the presence of ionizable groups provided stability only when in a charged state. In particular, both primary amines (DA, PEA) provided an isoelectric point around pH = 5, above which aggregation occurred, hindering the preparation of stable nanoparticle dispersions at neutral pH. On the other hand, both ligands with carboxylic acid groups (CA, PPA) imparted an isoelectric point around pH = 2-2.5 that ensured good dispersibility at neutral pH but aggregation under acidic conditions (Figure 3.3.1-3, right).

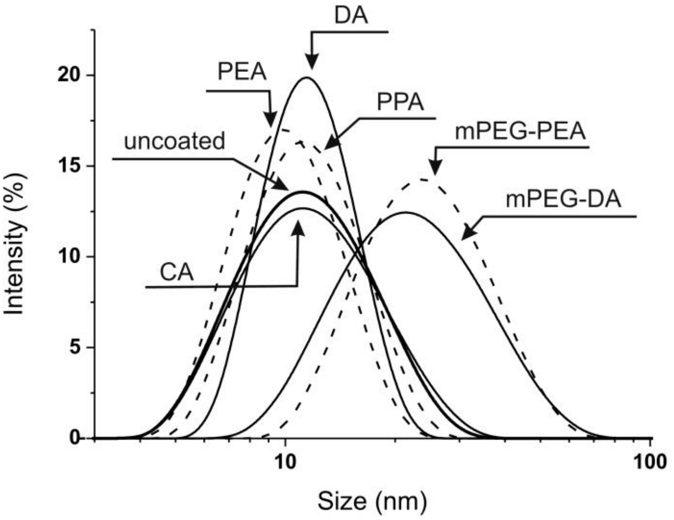

**Figure 3.3.1-2** Size distribution of titania nanoparticles before coating and after coating with various catechol (DA, mPEG-DA, CA) and phosph(on)ate ligands, which were used at a concentration of 5 μmol of ligand per mg of $TiO_2$. Nanoparticle concentration during DLS measurement: 0.2 mg/mL.

It is also noteworthy that the chemical functionality did not appear to have much influence in the adsorption, since dopamine (primary amine) and 2,3-dihydrocinnamic acid (carboxylic acid) showed an identical adsorption behaviour.

The final target of this phase was the optimisation of the surface coverage in view of maximizing the number of free sites available for photocatalysis, while also providing a sufficient density of groups to provide colloidal stability and “stealth” character, i.e. low cytotoxicity and low uptake by phagocytic cells. A dose of 5 μmol PEGylated ligand/mg of $TiO_2$ fully achieves the first point (colloidal stability, Figure 3.3.1-1 C), thus we have verified whether it would be sufficient to correctly address the second point too (“stealth” character), by studying dose- and time-dependent effects of nanoparticles coated with mPEG-DA at three ligand densities (5, 20 and 40 μmol ligand/mg of $TiO_2$). We assume mPEG-PEA to show a not significantly different behaviour.

**Table 3.3.1-1** Main physical characteristics of coated titania nanoparticles as a function of the structure of the coating ligand.

| Ligand | | ζ-potential (mV) [b] | | Isoelectric point [b] | Size (nm) |
|---|---|---|---|---|---|
| Acronym [a] | Nature | pH = 2 | pH = 7 | | |
| *Catechols* | | | | | |
| DA | Cationic | + 46 ± 6 | ≈ - 25 [c] | 5.2 | 12 (pH = 2) |
| CA | Anionic | ≈ + 5 [d] | - 39 ± 6 | 2.6 | 12 (pH = 7) |
| mPEG-DA | PEGylated | + 2 ± 2 | -4 ± 2 | 3.0 [e] | 19 (pH = 7) |
| PEG-bDA | PEGylated | + 3 ± 2 | -3 ± 2 | 2.8 [e] | 45 (pH = 7) |
| *Phosph(on)ates* | | | | | |
| PEA | Cationic | + 48 ± 5 | ≈ - 30 [c] | 5.0 | 10 (pH = 2) |
| PPA | Anionic | ≈ + 5 [d] | -36 ± 4 | 2.2 | 12 (pH = 7) |
| mPEG-PEA | PEGylated | +2 ± 3 | -13 ± 4 | 2.6 | 20 (pH = 7) |

[a] Summary of the acronyms: DA: dopamine. mPEG-DA: PEG2k monofunctionalized with dopamine. PEG-bDA: PEG2k funcionalized with dopamine at the two termini. CA: 3,4-dihydrohydroxycinnamic acid. PEA: *O*-phosphorylethanolamine. PPA: 3-phosphonopropionic acid.

[b] All measurements were performed at a surface coating of 5 μmol of ligand per mg of $TiO_2$. Please note that the ζ-potential of uncoated ("naked") nanoparticles

[c] Heavily and irreversibly aggregated samples; the ζ-potential values are not representative of the initial nanoparticle population.

[d] The nanoparticles formed gels at acidic pH (also upon adsorption of the ligands) but can be individually redispersed by bringing pH to neutrality.

[e] The ζ-potential of the nanoparticles coated mPEG-DA remained close to 0 mV for the full pH range analysed (pH 2-9), therefore the identification of a clear isoelectric point is difficult.

In terms of average cell viability (mitochondrial activity normalized against the protein content), PEGylated nanoparticles showed very low toxicity: the IC50 values at 2, 4 and 24 h exposure decreased with increasing degree of PEGylation and in any case were always > 3 mg/mL (see inserts in Figure 3.3.1-4 A-C), that is 1 – 2 orders of magnitude greater than the uncoated nanoparticles (Figure 3.3.1-4 D). However, the effects of the PEGylated nanoparticles on cell viability appeared to be essentially related to their titania content: the viability profile of the three particles appeared very similar when plotted against the amount of titanium dioxide in the dispersion. Therefore, we have concluded PEGylation to be a largely irrelevant factor and any effect on cell viability to essentially depend on the titania dosage. Last, it is noteworthy that the toxicity of these PEGylated nanoparticles is considerably higher than that previously recorded for larger titania particles decorated with the same ligand on another macrophage cell line (≈40 nm, mPEG-DA; IC50>25 mg/mL on J774.2 macrophages[23]); although cell-specific effects cannot be excluded, we are inclined to ascribe the higher toxicity of the smaller nanoparticles to their larger surface area that may provide also a larger number of sites that are capable of ROS production also in the dark[24].

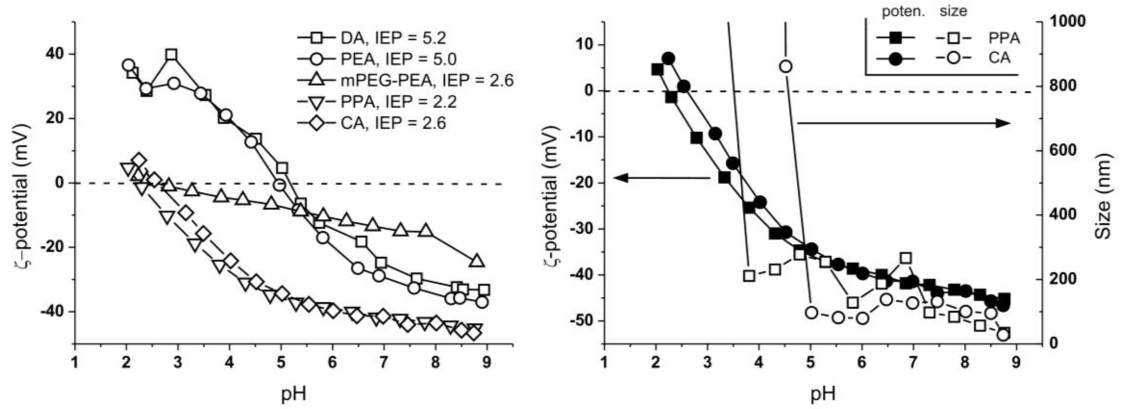

**Figure 3.3.1-3** ***Left:*** Plots of ζ-potential vs. pH for the variously coated nanoparticles; the behaviour of mPEG-DA (not shown for clarity) is almost identical to that of mPEG-PEA, but slightly more flat[23]. Ligand/titania ratio: 5μmol of ligand per mg of $TiO_2$. ***Right:*** a decrease in pH from neutrality to pH = 2 leads to the agglomeration of nanoparticles coated with carboxylate-bearing ligands. This is avoided during ligand adsorption by rapidly increasing pH immediately after the nanoparticle decoration (the process of ligand adsorption is considerably more rapid than that of particle agglomeration).

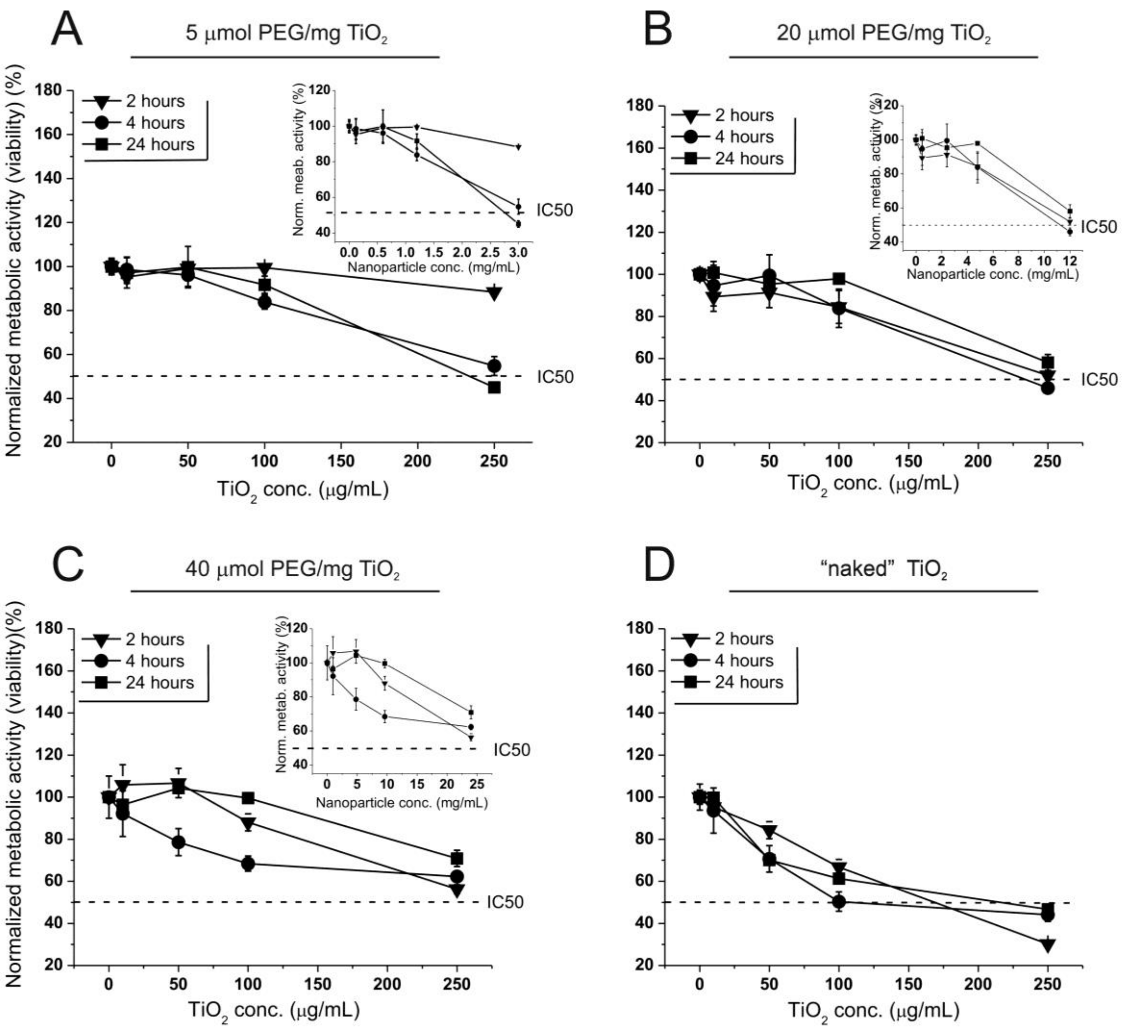

**Figure 3.3.1-4** Time and dose dependency studies of the effects of mPEG-DA decorated $TiO_2$ nanoparticles on the viability of RAW 246.7 macrophages, expressed as the mitochondrial reductase activity (MTS assay) normalized against the protein content (roughty proportional to the cell number; BCA assay). The panels present viability as a function of the concentration of titania in the samples, the inserts show the same data as a function of the overall nanoparticle concentration (= titania+PEGylated ligands). ***A***. Ligand density of 5 μmol of mPEG-DA per mg of titania. ***B***. Ligand density of 10 μmol of mPEG-DA per mg of titania. ***C***. Ligand density of 40 μmol of mPEG-DA per mg of titania. ***D***. Uncoated (“naked”) nanoparticles.

In terms of cell uptake, all PEGylated nanoparticles showed measurable uptake by macrophages, and their eventual localization in late endosomes/lysosomes indicates some form of endocytic uptake (Figure 3.3.1-5 A). The amount of internalized nanoparticles scaled linearly with concentration (Figure 3.3.1-5 B), which means that the same relative amount of nanoparticles was uptaken at any given concentration (Figure 3.3.1-5 C): this is typically observed in non-receptor mediated (macro)pinocytic processes, where the particles are uptaken through the endocytosis of volumes of fluid phases and hence of the internalized amount is linearly proportional to the concentration of the particles in the medium. Although these experiments cannot be used as a conclusive identification of the endocytosis mechanism, the linear dependency on concentration and the rather small uptake (5-8% wt.) at 24 hours can be used as a qualitative proof that, independently on the PEGylation degree, all the nanoparticles showed a reasonably "stealth" behaviour.

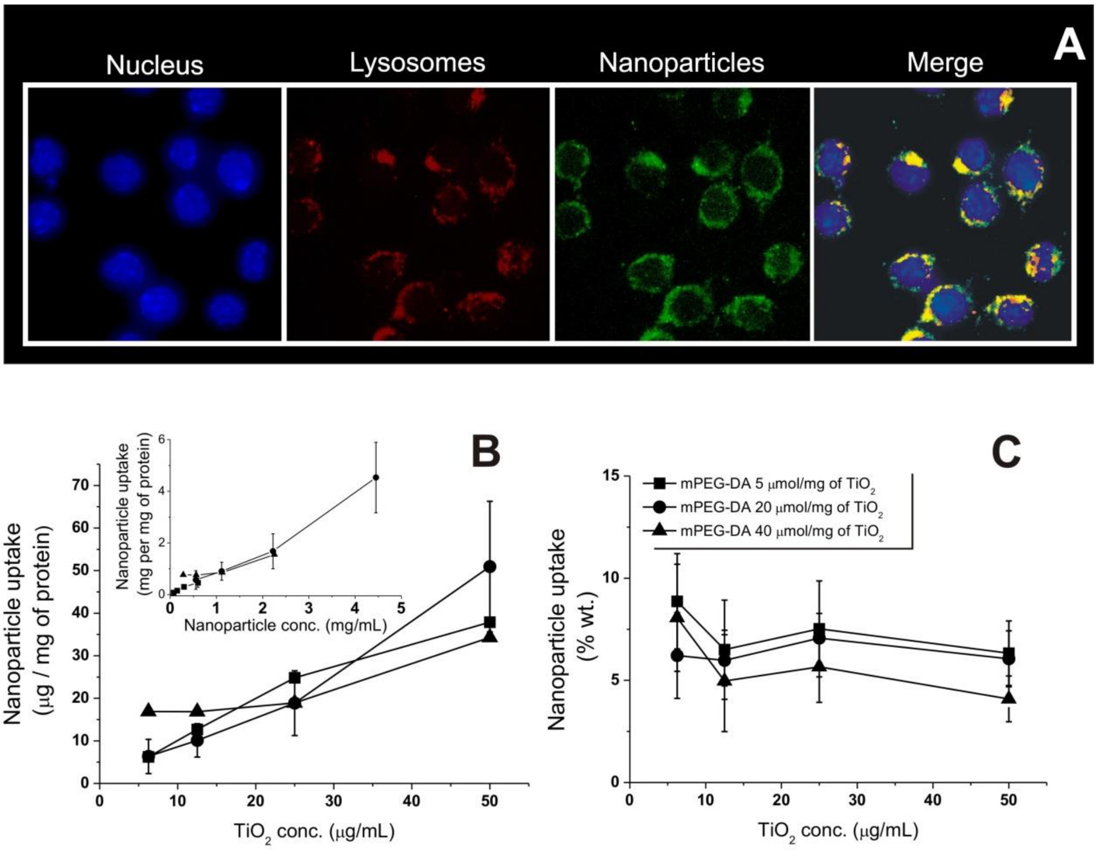

**Figure 3.3.1-5** ***A***. Confocal microscopy pictures of RAW macrophages after 24 h exposure to mPEG-DA coated nanoparticles (5 μmol ligand/mg of $TiO_2$, concentration: 50 μg/mL). ***B***. Uptake of mPEG-DA coated nanoparticles in RAW macrophages after 24 h exposure. The amount of nanoparticles was evaluated on cell lysates by measuring the emission intensity of fluorescein residues; the latter were introduced by adding small amounts of dopamine to the nanoparticles after their functionalization with mPEG-DA and then reacting the dopamine primary amines with fluorescamine (note: no fluorescence without reaction with amines). ***C***. The data of B are expressed as percentage in weight of the total amount of nanoparticles present in the medium.

### *3.3.2 Photoactivity of Nanoparticles*

The photo-oxidation activity of titania nanoparticles was assessed by studying the kinetics of methylene blue (MB) degradation, which is easily followed by monitoring the decrease in MB absorbance at 665 nm and typically shows a pseudo-first order kinetics[25].

**Catechol ligands:** we were unable to record any photocatalytic activity at any catechol surface density and for any ligand (DA and mPEG-DA at pH = 2, CA and mPEG-DA at pH = 7), using irradiation both using UV and also visible (400-500 nm) irradiation. This result may be seen as surprising, considering that dopamine-coated titanium oxide constructs have reportedly shown photocatalytic activity[26, 27]; on the contrary, several reports have previously shown the quenching effect of dopamine on the photooxidation[28] and electrogenerated luminescence[29] of titania nanostructures (but not e.g. on Degussa P-26, which is effectively composed of microparticles) as well as on the fluorescence[30] and photoelectrochemical properties[31] of quantum dots. Rajh *et. al.* have explained the catechol quenching effect as due to both the high stability of their surface-adsorbed species and their electron rich character that allows them to trap photogenerated holes, preventing them to create ROS or directly oxidize adsorbed species[32]. The free electrons created upon illumination would be trapped on local Ti centres eventually converting them to Ti(III) and therefore excluding recombination events.

This behaviour, however, is not necessarily detrimental, since the complete abrogation of ROS generation even at low catechol surface density can be advantageous in controlling the biocompatibility of titania *in vivo*.

**Phosph(on)ate ligands.** All particles coated with these ligands showed photooxidation activity. We have used nanoparticles uncoated or coated with relatively low ligand densities (1, 5 and 10 μmol of ligand per mg of titania), in order to avoid the complete saturation of titania surface sites; typically, photocatalyic activity plateaus at higher ligand densities (see Supplementary Information, Figure 3.6.2-SI-3), which parallels the asymptotes observed in ligand adsorption (Figure 3.3.1-1 B). At acidic pH (PEA- and mPEG-PEA-coated particles) we have observed that the presence of phosph(on)ate ligands considerably increased the MB degradation rate and thus likely also the efficiency of ROS generation, in comparison to uncoated nanoparticles (Figure 3.3.2-1, left); further, it appears that this effect depended on the density of the ligands and was significantly higher for the PEGylated ones.

At neutral pH (PPA and mPEG-PEA-coated particles) the MB degradation rate grew further, although similar trends were observed, i.e. increased rate with increasing ligand density and with PEGylation. We are inclined to attribute the dependency on ligand density to the chemical environment created by the surface functionalization, which may provide an increased stability to some ROS and also allow the pre-concentration of the substrate, rather than to the presence of fundamentally different photocatalytic centres.

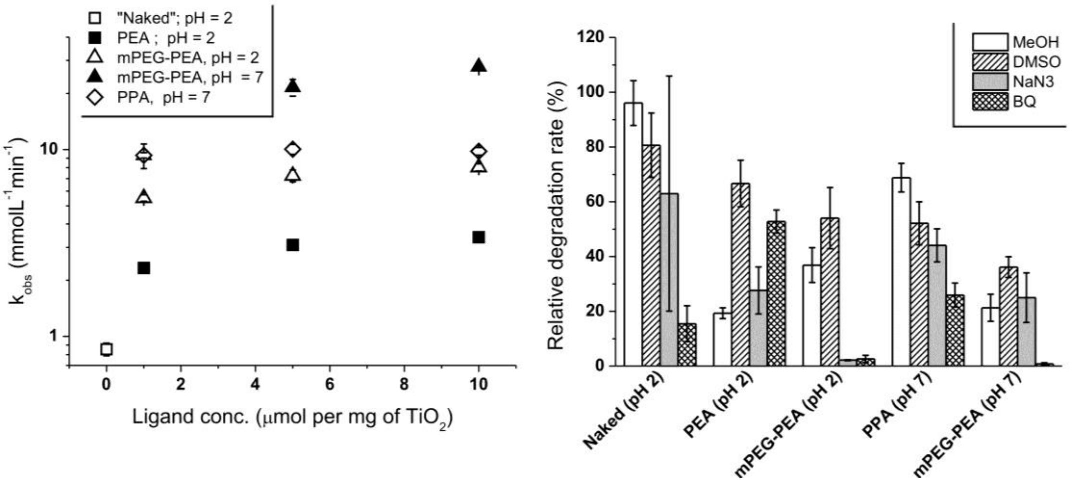

**Figure 3.3.2-1** ***Left.*** Photodegradation rate constants of methylene blue using photoactivated $TiO_2$ (0.2 mgmL$^{-1}$) with variable degree ligand density; pH = 2 in the absence of ligands and for PEA and mPEG-PEA; pH = 7 for PPA and mPEG-PEA. ***Right.*** Relative photodegradation rate constants for uncoated and phosph(on)ate-coated titania nanoparticles in the presence of ROS quenchers (nanoparticle concentration: 0.2 mg/mL; ligand density: 5 μmol of ligand per mg of $TiO_2$); the actual values of the constants are reported in Supplementary Information, Figure 5SI). MeOH: methanol; DMSO: dimethyl sulfoxide; $NaN_3$: sodium azide; BQ: benzoquinone.

In particular, we have considered two possible explanations of the differences between differently coated particles:

a) The MB degradation rate may be influenced by the charge of the nanoparticles. The highest ROS concentration is to be found in close proximity to the nanoparticle surfaces; however, due to the MB cationic charge, surfaces with highly positive ζ potential would repel it and therefore its degradation would be performed at a slower rate by more diluted ROS in the bulk of the solution. This could be an explanation for the more rapid degradation in the experiments conducted at pH = 7: both PPA and mPEG-DA coated particles are negatively charged at this pH value. On the other hand, such an explanation would not explain the higher efficiency of PEGylated surfaces, nor why higher ligand densities would boost MB degradation for PEA (cationic) and for PEG (neutral).

b) The presence of the ligands may influence the chemical composition of the cocktail of oxidants produced upon irradiation. For example, it is known that the presence of phosphate ($PO_4^{3-}$) groups enhances the production of OH radicals on macroscopic titania surfaces[20]. Using a constant density of 5 μmol of ligand per mg of $TiO_2$, we have performed experiments in the presence of several quenchers of ROS (Figure 3.3.2-1, right), i.e. methanol (scavenging positive holes, $h^+$ [33]), dimethyl sulfoxide (OH radicals [34]), sodium azide (singlet oxygen, $^1O_2$, [35], but also OH radicals[36] and benzoquinone (superoxide, $O_2^{\cdot-}$)[37]. It appears that the photocatalytic activity of uncoated nanoparticles was mostly based on the production of superoxide, since benzoquinone was the only scavenger capable to abrogate almost complete MB degradation. Superoxide seems to play a similarly important role for the PEGylated nanoparticles, both at pH = 2 and 7, but the major effects observed with other inhibitors and in particular with sodium azide indicate that other ROS are also heavily involved; the significant role of additional oxidants ROS may be the reason for the higher degradation rate in the order mPEG-PEA at pH = 7 > mPEG-PEA at pH = 2 > “naked” nanoparticles. PEA and PPA provided different pictures, with an apparent involvement of all the above ROS but a major role of positive holes for PEA at pH = 2 and of superoxide for PPA at pH = 7. This qualitative analysis does not allow to fully explain the dependency of the MB degradation rate on the ligand chemistry; however, it is clear that the latter influences the composition of the ROS cocktail and this is possibly a key parameter in the photocatalytic efficiency.

## 3.4 Conclusions

This study has provided a few significant findings. Firstly, both catechol- and phosph(on)ate ligands can be used to functionalize the surface of very small titania nanoparticles without causing any significant agglomeration. Secondly, PEGylated titania nanoparticles are not only dispersible throughout a broad range of pH, but are also characterized by low cytotoxicity even in a very sensitive cellular model (macrophages). Thirdly, and most importantly, the ligand chemistry was shown to dramatically influence titania photocatalytic activity, causing complete abrogation in the case of catechols and increased efficiency in the case of phosph(on)ates. It is also noteworthy that the chemical environment provided by the phosph(on)ate ligands markedly affected the production of ROS; very promisingly in view of biological applications, the best results were provided by PEGylated nanoparticles at pH = 7.

## 3.5 References

1. Oregan, B.; Gratzel, M., A low-cost, high-efficiency solar-cell based on dye-sensitized colloidal $TiO_2$ films. *Nature* **1991,** 353, (6346), 737-740.

2. Mills, A.; Davies, R. H.; Worsley, D., Water-purification by semiconductor photocatalysis. *Chem. Soc. Rev.* **1993,** 22, (6), 417-425.

3. Nohynek, G. J.; Lademann, J.; Ribaud, C.; Roberts, M. S., Grey goo on the skin? Nanotechnology, cosmetic and sunscreen safety. *Crit. Rev. Toxicol.* **2007,** 37, (3), 251-277.

4. Carp, O.; Huisman, C. L.; Reller, A., Photoinduced reactivity of titanium dioxide. *Prog. Solid State Ch.* **2004,** 32, (1-2), 33-177.

5. Zhang, Z. B.; Wang, C. C.; Zakaria, R.; Ying, J. Y., Role of particle size in nanocrystalline $TiO_2$-based photocatalysts. *J. Phys. Chem. B* **1998,** 102, (52), 10871-10878.

6. Serpone, N.; Lawless, D.; Khairutdinov, R., Size effects on the photophysical properties of colloidal anatase $TiO_2$ particles - size quantization or direct transitions in this indirect semiconductor. *J. Phys. Chem.* **1995,** 99, (45), 16646-16654.

7. Almquist, C. B.; Biswas, P., Role of synthesis method and particle size of nanostructured $TiO(_2)$ on its photoactivity. *J. Catal.* **2002,** 212, (2), 145-156.

8. Paz, Y.; Luo, Z.; Rabenberg, L.; Heller, A., Photooxidative self-cleaning transparent titanium-dioxide films on glass. *J. Mater. Res.* **1995,** 10, (11), 2842-2848.

9. Minabe, T.; Tryk, D. A.; Sawunyama, P.; Kikuchi, Y.; Hashimoto, K.; Fujishima, A., TiO2-mediated photodegradation of liquid and solid organic compounds. *J. Photoch. Photobio. A* **2000,** 137, (1), 53-62.

10. Yamaguchi, S.; Kobayashi, H.; Narita, T.; Kanehira, K.; Sonezaki, S.; Kubota, Y.; Terasaka, S.; Iwasaki, Y., Novel Photodynamic Therapy Using Water-dispersed $TiO_2$-Polyethylene Glycol Compound: Evaluation of Antitumor Effect on Glioma Cells and Spheroids In Vitro. *Photochem. Photobiol.* **2010,** 86, (4), 964-971.

11. Dougherty, T. J.; Gomer, C. J.; Henderson, B. W.; Jori, G.; Kessel, D.; Korbelik, M.; Moan, J.; Peng, Q., Photodynamic therapy. *J. Natl. Cancer Inst.* **1998,** 90, (12), 889-905.

12. Deng, Z. J.; Mortimer, G.; Schiller, T.; Musumeci, A.; Martin, D.; Minchin, R. F., Differential plasma protein binding to metal oxide nanoparticles. *Nanotechnology* **2009,** 20, (45).

13. Niidome, T.; Yamagata, M.; Okamoto, Y.; Akiyama, Y.; Takahashi, H.; Kawano, T.; Katayama, Y.; Niidome, Y., PEG-modified gold nanorods with a stealth character for in vivo applications. *J. Control. Release* **2006,** 114, (3), 343-347.

14. Araujo, P. Z.; Morando, P. J.; Blesa, M. A., Interaction of catechol and gallic acid with titanium dioxide in aqueous suspensions. 1. Equilibrium studies. *Langmuir* **2005,** 21, (8), 3470-3474.

15. Bae, E. Y.; Choi, W. Y.; Park, J. W.; Shin, H. S.; Kim, S. B.; Lee, J. S., Effects of surface anchoring groups (Carboxylate vs phosphonate) in ruthenium-complex-sensitized $TiO_2$ on visible light reactivity in aqueous suspensions. *J. Phys. Chem. B* **2004,** 108, (37), 14093-14101.

16. Zeller, A.; Musyanovych, A.; Kappl, M.; Ethirajan, A.; Dass, M.; Markova, D.; Klapper, M.; Landfester, K., Nanostructured Coatings by Adhesion of Phosphonated Polystyrene Particles onto Titanium Surface for Implant Material Applications. *ACS Appl. Mater. Interfaces* **2010,** 2, (8), 2421-2428.

17. Creutz, C.; Chou, M. H., Binding of catechols to mononuclear titanium(IV) and to 1-and 5-nm $TiO_2$ nanoparticles. *Inorg. Chem.* **2008,** 47, (9), 3509-3514.

18. Kar, P.; Verma, S.; Sen, A.; Das, A.; Ganguly, B.; Ghosh, H. N., Sensitization of Nanocrystalline $TiO_2$ Anchored with Pendant Catechol Functionality Using a New Tetracyanato Ruthenium(II) Polypyridyl Complex. *Inorg. Chem.* **2010,** 49, (9), 4167-4174.

19. Jing, L. Q.; Cao, Y.; Cui, H. Q.; Durrant, J. R.; Tang, J. W.; Liu, D. N.; Fu, H. G., Acceleration effects of phosphate modification on the decay dynamics of photo-generated electrons of $TiO_2$ and its photocatalytic activity. *Chem. Commun.* **2012,** 48, (87), 10775-10777.

20. Zhao, D.; Chen, C. C.; Wang, Y. F.; Ji, H. W.; Ma, W. H.; Zang, L.; Zhao, J. C., Surface modification of $TiO_2$ by phosphate: Effect on photocatalytic activity and mechanism implication. *J. Phys. Chem. C* **2008,** 112, (15), 5993-6001.

21. Randon, J.; Blanc, P.; Paterson, R., Modification of ceramic membrane surfaces using phosphoric-acid and alkyl phosphonic-acids and its effects on ultrafiltration of bsa protein. *J. Membr. Sci.* **1995,** 98, (1-2), 119-129.

22. Kanan, S. M.; Tripp, C. P., An infrared study of adsorbed organophosphonates on silica: A prefiltering strategy for the detection of nerve agents on metal oxide sensors. *Langmuir* **2001,** 17, (7), 2213-2218.

23. Kotsokechagia, T.; Zaki, N. M.; Syres, K.; de Leonardis, P.; Thomas, A.; Cellesi, F.; Tirelli, N., PEGylation of Nanosubstrates (Titania) with Multifunctional Reagents: At the Crossroads between Nanoparticles and Nanocomposites. *Langmuir* **2012,** 28, (31), 11490-11501.

24. Gurr, J. R.; Wang, A. S. S.; Chen, C. H.; Jan, K. Y., Ultrafine titanium dioxide particles in the absence of photoactivation can induce oxidative damage to human bronchial epithelial cells. *Toxicology* **2005,** 213, (1-2), 66-73.

25. Zhang, T. Y.; Oyama, T.; Aoshima, A.; Hidaka, H.; Zhao, J. C.; Serpone, N., Photooxidative N-demethylation of methylene blue in aqueous $TiO_2$ dispersions under UV irradiation. *J. Photochem. Photobio. A* **2001,** 140, (2), 163-172.

26. Dawson, G.; Liu, J. H.; Lu, L. H.; Chen, W., Dopamine-Modified Trititanate Nanotubes with UV- and Visible-Light Photocatalytic Activity: Coordinative Self-Assembly into a Recyclable Absorber. *ChemCatChem* **2012,** 4, (8), 1133-1138.

27. Tachikawa, T.; Asanoi, Y.; Kawai, K.; Tojo, S.; Sugimoto, A.; Fujitsuka, M.; Majima, T., Photocatalytic cleavage of single $TiO_2$/DNA nanoconjugates. *Chem.-Eur. J.* **2008,** 14, (5), 1492-1498.

28. Geiseler, B.; Miljevic, M.; Mueller, P.; Fruk, L., Phototriggered Production of Reactive Oxygen Species by TIO2 Nanospheres and Rods. *J. Nanomater.* **2012**.

29. Chen, L. F.; Lu, L. L.; Mo, Y.; Xu, Z. M.; Xie, S. P.; Yuan, H. Y.; Xiao, D.; Choi, M. M. F., Electrogenerated chemiluminescence of anatase TiO2 nanotubes film. *Talanta* **2011,** 85, (1), 56-62.

30. Clarke, S. J.; Hollmann, C. A.; Zhang, Z. J.; Suffern, D.; Bradforth, S. E.; Dimitrijevic, N. M.; Minarik, W. G.; Nadeau, J. L., Photophysics of dopamine-modified quantumdots and effects on biological systems. *Nat. Mater.* **2006,** 5, (5), 409-417.

31. Hao, Q.; Wang, P.; Ma, X. Y.; Su, M. Q.; Lei, J. P.; Ju, H. X., Charge recombination suppression-based photoelectrochemical strategy for detection of dopamine. *Electrochem. Commun.* **2012,** 21, 39-41.

32. Rajh, T.; Chen, L. X.; Lukas, K.; Liu, T.; Thurnauer, M. C.; Tiede, D. M., Surface restructuring of nanoparticles: An efficient route for ligand-metal oxide crosstalk. *J. Phys. Chem. B* **2002,** 106, (41), 10543-10552.

33. Tan, T.; Beydoun, D.; Amal, R., Effects of organic hole scavengers on the photocatalytic reduction of selenium anions. *J. Photochem. Photobio A* **2003,** 159, (3), 273-280.

34. Wang, X. P.; Tang, Y. X.; Chen, Z.; Lim, T. T., Highly stable heterostructured Ag-AgBr/$TiO_2$ composite: a bifunctional visible-light active photocatalyst for destruction of ibuprofen and bacteria. *J. Mater. Chem.* **2012,** 22, (43), 23149-23158.

35. Stylidi, M.; Kondarides, D. I.; Verykios, X. E., Visible light-induced photocatalytic degradation of Acid Orange 7 in aqueous $TiO_2$ suspensions. *Appl. Catal. B-Environ.* **2004,** 47, (3), 189-201.

36. Frati, E.; Khatib, A. M.; Front, P.; Panasyuk, A.; Aprile, F.; Mitrovic, D. R., Degradation of hyaluronic acid by photosensitized riboflavin in vitro. Modulation of the effect by transition metals, radical quenchers, and metal chelators. *Free Radical Bio. Med.* **1997,** 22, (7), 1139-1144.

37. Manring, L. E.; Kramer, M. K.; Foote, C. S., Interception of $O_2$- by benzoquinone in cyanoaromatic-sensitized photooxygenations. *Tetrahedron Lett.* **1984,** 25, (24), 2523-2526.

## 3.6 Supplementary Information

### *3.6.1 Adsorption of catechol ligands on titania nanoparticles*

Here we have employed the same analysis used in a recent publication[23].

In a first stage, we have ascribed the absorbance completely to chelated complexes of catechols, whose concentration is related to the total concentration of adsorbed catechols through a coefficient $k$ (fraction of chelating catechols). As a result the absorbance can be linked to the initial concentration of catechols ($[DA]_0$) and to the actual concentration of catechols in solution ($[DA]_{free}$):

$$A = \varepsilon_{chel}[TiDA]_{chel} = \varepsilon_{chel}k[DA]_{ads} = \varepsilon_{chel}k([DA]_0 - [DA]_{free})$$

In the initial stages of the adsorption isotherms (Figure 1SI, left), it is possible to neglect the last term; therefore the expression becomes $A \approx \varepsilon_{chel}k[DA]_0$, which allows to calculate the factor $\varepsilon_{chel}k$ from the slope of the curves and therefore also to compare the relative values of k for various systems.

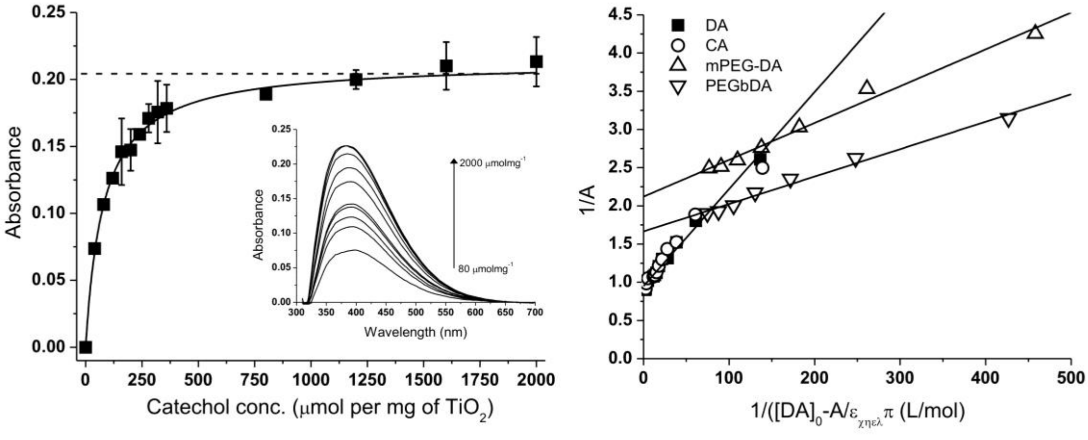

**Figure 3.6.1-SI-1** ***Left.*** Typical adsorption curve used to monitor the surface decoration of nanoparticles with catechol ligands (in this case dopamine, pH = 2, 10 nm titania nanoparticles at a concentration of 0.05 mg/mL). ***Right***. Linearized form of the adsorption curves for all catechol ligands; the lines represent the best fits obtained using a Langmuir adsorption model; nanoparticle concentration: 0.26 mg/mL; pH = 2.

Using high catechol concentration one saturates all available surface sites; their total concentration is expressed as $[Ti]_0$, and the number of available sites for a given catechol is $f[Ti]_0$ . Therefore, the absorbance can be expressed as $A = \varepsilon_{chel} k f [Ti]_0$. In the adsorption curves, at the crossing point between the initial slope and the absorbance asymptote $A_\infty$ (corresponding to a catechol concentration $[DA]_{cross}$) one will have $A_\infty = \varepsilon_{chel} k f [Ti]_0 \approx \varepsilon_{chel} k [DA]_{cross}$. From the comparison of the $[DA]_{cross}$ values, it is therefore possible to estimate the relative values of the occupancy of the surface sites.

Finally, using a Langmuir isotherm model where $K_L$ is an adsorption constant, it is possible to linearize the absorbance values in the form (Figure 1SI, right)

$$1/A = \frac{1}{\varepsilon_{chel} k f [Ti]_0} (1 + \frac{1}{K_L([DA]_0 - A/\varepsilon_{chel} k)}$$

and thus calculate the values of the adsorption constant.

In Table 1SI we report the values of the key parameters recorded in this study on 10 nm anatase nanoparticles and those previously recorded on larger (35 nm) and more aggregated nanoparticles, both prepared through a non-aqueous synthetic method. Please take into account that the concentration of 10 nm nanoparticles had to be lowered by about one order of magnitude in order to reach meaningful data of optical density: the smaller size correspondingly increases the number of surface sites.

Significant differences can be noticed between the two kinds of nanoparticles, which are to be ascribed to the differences in size, in morphology and in concentration; for example, the adsorption constants appear significantly lower because they also include a term related to the amount of available surface sites on the titania particles. However, the key parameters show a qualitative agreement: most importantly, a decrease in the relative occupancy and an increase in the fraction of chelating catechols and in the overall adsorption constant in the order dopamine - mPEG-DA – PEG-bDA.

**Table 3.6.1-SI-1** Comparison of adsorption parameters of catechol ligands for 10 nm titania nanoparticles at a concentration of 0.26 mg/mL (this study) and 35 nm ones at a concentration of 30 mg/mL (previous study[23]).

| | $[DA]_{cross}$ (mM) | | $A_\infty$ | | $\varepsilon_{chel}k$ (L/mol) | | $f_x/f_{DA}$ | | $k_x/k_{DA}$ | | $K_L$ (L/mol) | |
|---|---|---|---|---|---|---|---|---|---|---|---|---|
| | 10 | 35 nm | 10 | 35 nm | 10 | 35 nm | 10 | 35 nm | 10 | 35 nm | 10 | 35 nm |
| DA | 7.1 | 2.1 | 0.85 | 0.30 | 125 | 199 | 1 | 1 | 1 | 1 | 75 | 2280 |
| CA | 5.7 | | 0.84 | | 125 | | 1 | | 1 | | 84 | |
| mPEG-DA | 4.8 | 1.5 | 0.37 | 0.30 | 125 | 265 | 0.30 | 0.72 | 1 | 1.33 | 440 | 3120 |
| PEG-bDA | 3.5 | 0.9 | 0.51 | 0.69 | 185 | 980 | 0.18 | 0.43 | 1.5 | 4.9 | 460 | 5074 |

### 3.6.2 Degradation of methylene blue

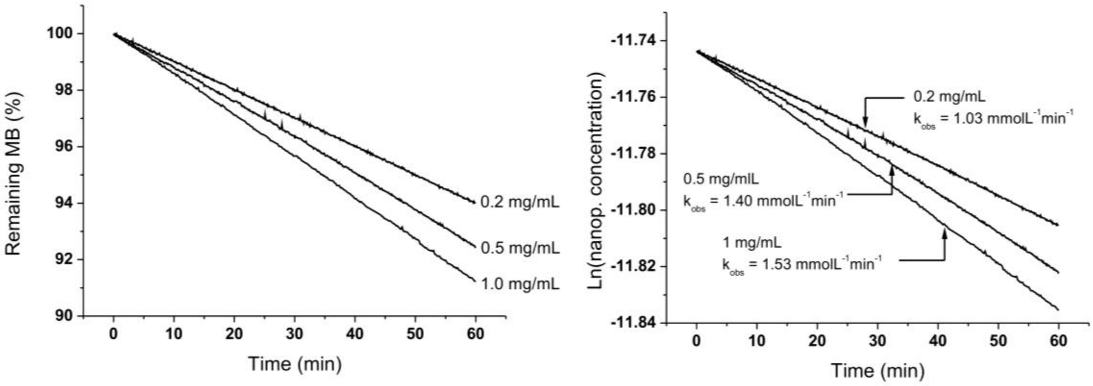

**Figure 3.6.2-SI-1** ***Left***. Degradation profile of MB under illumination in the presence of varying concentrations of uncoated nanoparticles (10 nm, pH =2). ***Right***. Plot of lnC against time, the slope of which provides the degradation rate of MB.

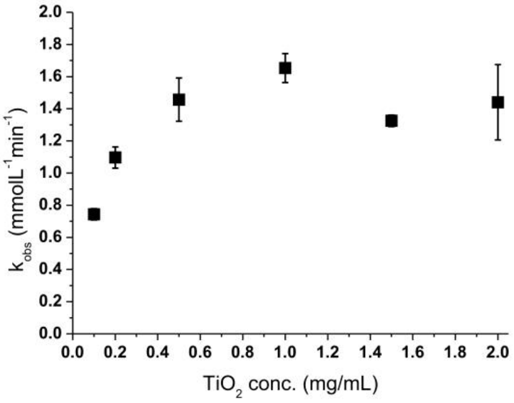

**Figure 3.6.2-SI-2** Degradation rate of MB as a function of the concentration of uncoated $TiO_2$ nanoparticles. The plateau in $k_{obs}$ is due to the increased scattering of light by nanoparticles, hindering the penetration of light in the bulk of the MB solution.

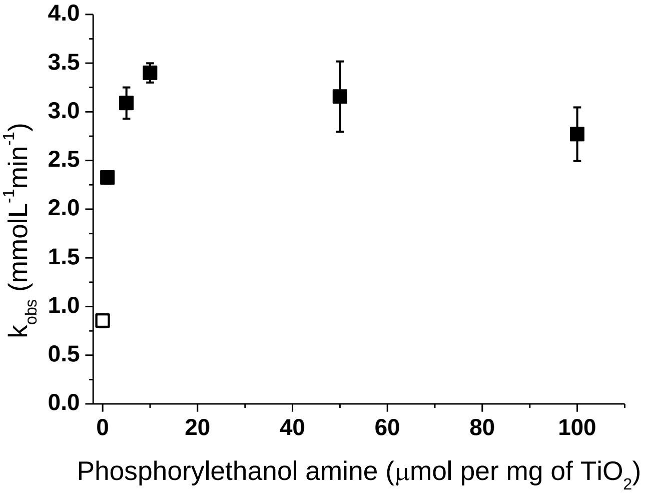

**Figure 3.6.2-SI-3** Photodegradation rate constants of methylene blue using photoactivated $TiO_2$ nanoparticles (0.2 mg/mL) with varying degrees of surface functionalisation with PEA**.**

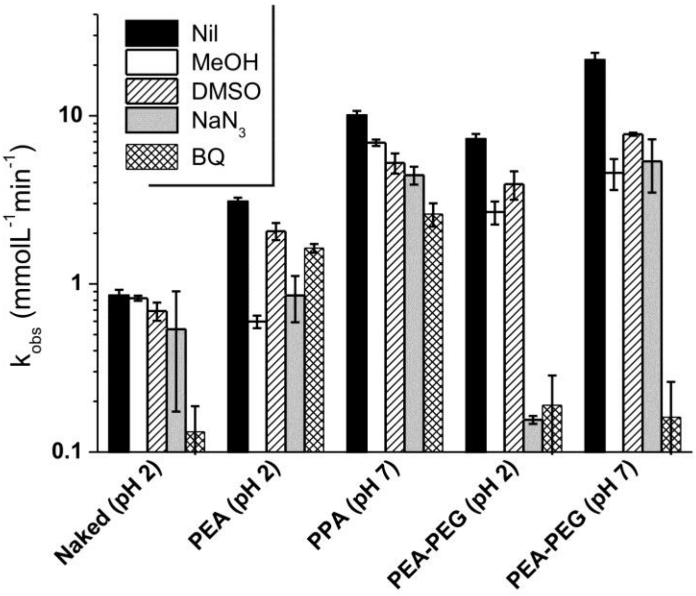

**Figure 3.6.2-SI-4** Photodegradation rate constants of methylene blue recorded with uncoated and phosph(on)ate-coated titania nanoparticles in the presence of ROS quenchers (nanoparticle concentration: 0.2 mg/mL; ligand density: 5 μmol of ligand per mg of $TiO_2$).

# 4 Titania-mediated UV-triggered release from multilayered polymer walled microspheres

Christopher J. Cadman[a], Ghislaine Robert-Nicoud[b], Qamar Hussain[c], Francesco Cellesi[a], Nicola Tirelli[b,c*]

[a] School of Pharmacy and Pharmaceutical Sciences, University of Manchester, Oxford Road, Manchester, M13 9PT, United Kingdom

[b] Institute of Inflammation and Repair, University of Manchester, Oxford Road, Manchester, M13 9PT, United Kingdom

[c] School of Materials, University of Manchester, Oxford Road, Manchester, M13 9PT, United Kingdom

to whom correspondence should be addressed:

Prof. Nicola Tirelli, Institute of Inflammation and Repair, University of Manchester, Oxford Road, Manchester, M13 9PT, United Kingdom

Tel: +44 161 275 18 02

Email: Nicola.tirelli@manchester.ac.uk

## Abstract

Herein we present the development of UV sensitive polyelectrolyte multilayer capsules whose response is based on anatase photo-oxidation behaviour. Hollow core microspheres were prepared using the layer by layer (LbL) addition of poly(sodium 4-styrene sulfonate) (PSS) and poly(allylamine) (PAH) around a $CaCO_3$ core, which could be subsequently removed by complexation with ethylenediaminetetraacetic acid (EDTA) . After preparation the porous walls allowed the diffusion of substances with a molecular weight between 5-10 kDa into the cores, however after heat treatment (65°C) the pores shrunk entrapping any contained molecules. By substituting a layer of the multilayer wall with titanium dioxide ($TiO_2$) nanoparticles, the microcapsules could be ruptured by the reactive oxygen species created by $TiO_2$ under UV illumination, thus releasing any entrapped substances.

We have shown that indeed the microcapsules can be loaded in a facile manner however, due to the nature of the model polymer used, the loading efficiency was much too high to be diffusion based alone. With this in mind the percentage of polymer released under UV illumination remained relatively low compared to that encapsulated, being no more than 2%. Nevertheless, when taking into account the concentrations of the model polymer in the surrounding media after illumination, it was clear that the levels present were well within, or even above, the therapeutic threshold of many drugs.

## 4.1 Introduction

In recent years there has been considerable attention directed at developing “smart” stimulus responsive drug delivery systems which, as the name suggests, are able to encapsulate bioactive agents and release them at targeted sites *in vivo*. The drive for developing drug carriers is twofold;

1) Around 40-70% of new drug candidates are immediately rejected for further research due to their limited solubility under physiological conditions[1].

2) Often drugs which pass clinical trials and enter the market come with a number of side effects which can lead to a substantial amount of physical and mental distress e.g. as with chemotherapeutic drugs. In fact, most anti-cancer drugs cannot be administered at dosages high enough to eradicate all cancer cells due to their high general toxicity[2].

Considering these points, when developing drug carriers there are a number of requirements that must be adhered to. Most importantly the carrier must protect the payload from degradation *in vivo* and it must also prevent unwanted leakage of the drug out of the system. Of course the carrier itself must be stable and non-toxic in *in vivo* conditions and it must have the ability to encapsulate a wide range of molecules, be they hydrophilic or hydrophobic. Lastly, the carrier must be able to release the payload “on command” and the method of drug release must preserve the activity of the drug[3-5]. Typically the stimulus for release usually falls into one of three categories being changes in pH[6] or temperature[7] or the external application of a magnetic field[8]. However, one other mode of stimulus that is gaining popularity is the use of light[9-11]. Historically using light as a stimulus has not attracted much attention as there are inevitable problems with penetration depth of the light into bodily tissues. However, recent advancements in micron sized endoscopes[12] and dual photon microscopy[13] have improved the penetration capabilities of light into bodily tissues many times over. In this study we present, for the first time, polyelectrolyte multilayer (PEM) microparticles which can be triggered to release their payload using UV light.

PEM capsules have been regarded in recent years as potential candidates for drug delivery applications[14-16]. PEM capsules can be created by layer by layer (LbL) addition of polymer chains around a solid core. For use *in vivo* the size of the microcapsule matters as typically administered objects need to be smaller than ~ 200 nm to avoid rapid filtration out of the bloodstream by the spleen[17]. The fabrication of nanoscale PEM capsules has been reported on a number of occasions[18-20] however, the field is relatively young and typically, for the moment, most reports relate to the fabrication of microcapsules due to the relative ease of characterisation and analysis compared to their nano counterparts.

The microcapsules used in this study are based on those previously reported by Carregal-Romero *et. al.* where alternating layers of poly(styrenesulfonate) (PSS) and poly(allylamine) (PAH), acting as the negative and positively charged moiety respectively, were added in an LbL fashion around a solid $CaCO_3$ microsized core[21]. During preparation one of the PSS inner layers was substituted for titanium dioxide ($TiO_2$) nanoparticles with a negative surface charge owing to the preadsorption of etidronic acid. After fabrication the $CaCO_3$ core was easily dissolved out of the microsphere by complexing with ethylenediaminetetraacetic acid (EDTA), leaving hollow core polymer walled microspheres behind. The microspheres were then post loaded with blue dextran and their UV triggered release capabilities were assessed.

## 4.2 Materials and Methods

### *4.2.1 Materials*

Poly(sodium 4-styrenesulfonate) (PSS, $\overline{M_w} \approx 70$ kDa), poly(allylamine hydrochloride) (PAH, $\overline{M_w} \approx 56$ kDa), calcium chloride dehydrate ($CaCl_2$), sodium carbonate ($Na_2CO_3$), ethylenediaminetetraacetic acid disodium salt dehydrate (EDTA disodium salt), dextran sulfate sodium salt (DEXS, $\overline{M_w} \approx 10$ kDa), Dextran from *Leuconostoc* spp. ($\overline{M_w} \approx 8$ kDa), etidronic acid (60% aqueous solution) and Reactive Blue 2 were purchased from Sigma-Aldrich (Gillingham, UK). 1M aqueous solutions of sodium hydroxide and hydrochloric acid were purchased from Fisher Scientific (Loughborough, UK). All chemicals were used as received without further purification. Water was pre-deionised and further purified by a Milli-Q system (Millipore, U.K.)

### *4.2.2 Physico-chemical characterization*

*Infrared Spectroscopy.* IR spectra were recorded in ATR mode on a Tensor 27 Bruker spectrometer on solid samples.

*Dynamic Light Scattering (DLS) and ζ potential analysis.* The measurements were performed using a Zetasizer Nano ZS instrument (Malvern Instrument Ltd., U.K.). Unless otherwise stated, quartz cuvettes with an optical path of 10 mm and disposable capillary flow cells were used respectively for DLS and zeta potential measurements.

*Gel permeation chromatography (GPC)* was performed on a PL-GPC 120 in dimethylacetamide (containing 0.5% $LiNO_3$) using a combination of two 10 μm (30 cm) different columns (PLgel 500Å and Mixed-B) at 50 °C and with a flow rate of 1.0 mL $min^{-1}$. The detection was performed with a differential refractometer using a series of narrowly distributed poly(ethylene glycol) standards for calibration.

*$^1$H NMR spectrometry.* Proton spectra were recorded with a 300 MHz Bruker spectrometer (Bruker UK Limited, UK); NMR samples were prepared in $D_2O$ at a concentration of 1 wt.%.

*UV-Vis Spectrophotometry.* Absorbance was routinely monitored in 96 well plates using a Biotek, Synergy 2 plate reader.

### *4.2.3 Synthesis of titanium dioxide nanoparticles*

$Ti(O^iPr)_4$ (9.12 mmol) was added to benzyl alcohol (20 mL) which contained water and hydrochloric acid in molar ratios to the titanium precursor of 4 and 1.17 respectively. The reaction was heated (80 °C) using a Radleys Carousel 12 plus Reaction Station (Radleys, UK) under nitrogen. The reaction was stopped when the average diameter of the nanoparticles reached 10 nm. The nanoparticles were then precipitated in diethyl ether (150 mL) and centrifuged (3,500 rpm, 5 mins). The supernatant was decanted and the resulting white solid was washed twice with diethyl ether (50 mL). The precipitate was then re-dispersed in a water-ethanol solution (20 mL, 50:50 w/w) at pH = 2 (pH buffered with 0.1 N HCl). The resulting dispersion was dialysed against purified water at pH = 2 using a dialysis membrane with a MWCO of 10,000 g/mol. The final concentration of the nanoparticle suspension (typically 5 mg/mL) was calculated by neutralising a 1 mL sample of the solution using 1 N $Na_2CO_3$, inducing precipitation, followed by centrifugation (3500 rpm, 5 mins) and decantation. The sample was washed with water and centrifuged again. Water (10 mL) was added to the precipitate and the resulting suspension was freeze dried. The final nanoparticles were monodisperse and had an average size of 10 nm by dynamic light scattering (DLS). To prepare UV light triggered microparticles, titanium dioxide ($TiO_2$) nanoparticles were first coated with etidronic acid to give a grafting density of 10 μmol per mg of $TiO_2$. The resulting nanoparticles possessed a negative surface charge having a ζ potential of – 42.3 mV.

### *4.2.4 Preparation of hollow core microspheres*

$CaCO_3$ microparticles were prepared by mixing equal volumes (615 μl) of aqueous $CaCl_2$ (0.33 M) and $Na_2CO_3$ (0.33 M) along with 750 μl of aqueous dextran ($\overline{M_w}$ = 10 kDa, 1 mgmL$^{-1}$). The solution was vigorously mixed on a magnetic stirrer (1000 rpm, 30 secs) and subsequently left standing at room temperature for 3 minutes. The resulting microparticles were then washed three times by centrifuging the suspension (2,500 rpm, 5 minutes) and replacing the supernatant with water (2 mL). A polymer shell was then grown around the microsphere cores using the layer by layer (LbL) technique. The microparticles were dispersed in 2 mL of a PSS solution (2 mg/mL, 0.5 M NaCl, pH 6.5), sonicated for 2 minutes and then vigorously shaken for 10 minutes. The microparticles were then washed three times with water and redispersed in 2 mL of a solution containing the polycationic polymer PAH (2 mg/mL, 0.5 M NaCl, pH 6.5) and the second layer of polymer was left to adsorb as previously described. In total 8 layers of polymer were coated onto the surface of the microparticles with the final layer being positively charged PAH. After synthesis the

$CaCO_3$ core was dissolved out of the microparticles by mixing them with EDTA (1 mL, 0.2 M, pH 5.5) and shaking for 2 minutes. The microparticles were then washed four times as previously described and the resulting microspheres redispersed in 1 mL of water.

The above method describes how to prepare the template for the hollow core microspheres and these were used for all controls. The nanoparticles (2 mg/mL, 0.5 M NaCL, pH 6.5) were then substituted for PSS in the 5th layer of the microparticle shell and adsorbed as previously described. After preparation the microparticles were counted using a haemocytometer and the number of microparticles prepared per batch was found to be $\approx 3 \times 10^9$.

### 4.2.5 Synthesis of blue dextran

Dextran (1 g, ~ 5.6 mmol of glucose units) was dissolved in an aqueous solution of sodium hydroxide (0.2 M, 10 mL) and stirred for 1 hour at room temperature. Reactive Blue 2 (400 mg, 0.48 mmol) was added and the solution was stirred at 60°C overnight. The solution was then neutralised using aqueous hydrochloric acid (1 M) and the product was purified through dialysis against deionised water using SpectraPor regenerated cellulose membranes, with a 8,000-10,000 g/mol molecular weight cut-off. A blue solid was obtained after freeze-drying (58-65% yield). Functionalization = 0.9 %wt. via UV spectroscopy $\frac{A}{\varepsilon_{RB}} \times \frac{M_r}{C}$ (where A is the absorbance of the dye conjugated polymer, $\varepsilon_{RB}$ is the molar extinction coefficient of reactive blue, $M_r$ is the molecular weight of reactive blue and C is the concentration of polymer in $gL^{-1}$). GPC: $\overline{M_w}$ = 10 kDa and $\overline{M_w}/\overline{M_n}$ = 1.3 (the increase in $\overline{M_w}$ is due to the MWCO of the dialysis membrane used which was very close to the original dextran $\overline{M_w}$, therefore some low molecular weight polymer was lost through purification).

$^1H$ NMR ($D_2O$): $\delta$ = 3.5-4 (multiple peaks from dextran), 4.95 (d, 2H, dextran anomeric protons), 6.4-8.2 (multiple peaks from reactive blue, too low intensities for reliable integration or multiplicity determination) ppm.

FT-IR (film on ATR crystal): 3660-3035 (ν OH), 2927 (broad signal, ν CH), 1749 (ν C=O), 1570 (ω, triazine ring stretching) 1421 (δ $CH_2$), 1348 (ω $CH_2$), 1269, 1149, 1011 ($\nu_{as}$ C-O-C), 916 ($\nu_s$ C-O-C), 848, 763, 700 (aromatic $\gamma_{oop}$ CH) $cm^{-1}$.

### 4.2.6 Loading of hollow spheres with dye-conjugated polymers

To load the microcapsules, a highly concentrated microcapsule dispersion ($\approx 7 \times 10^8$ microcapsules/mL) were dispersed in a solution of blue dextran (1 mg/mL) for 1 hour. The microcapsule dispersion was then heated to 65 °C for 2 hours after which it was centrifuged (2500 rpm, 8 min) and washed with deionised water 3 times. The encapsulation efficiency (*ee*) was determined by calculating the remaining concentration of blue dextran in the supernatant, collected after loading and washings, by UV-Vis spectrophotometry against a calibration curve using the following equation: ee (%) = $(\text{mass}_{\text{starting material}} - \text{mass}_{\text{unloaded material}})/ \text{mass}_{\text{starting material}} \times 100$.

### 4.2.7 Photochemical experiments

An Omnicure® S1000 fitted with a 250-450 nm filter as the light source was used with the output power being 10 $mW/cm^2$ at the end of an optical fibre (Omnicure® liquid light guide). The optical fibre was inserted through a condenser placed on the top neck of a 25 mL two necked flask in order to tightly hold the fibre in position above the solution contained in the flask. 5 mL of a $\approx 2*10^6$ microparticles/mL solution, either containing titania nanoparticles or not, were placed into the two necked flask and illuminated for variable periods of time (5, 10 or 90 minutes) under magnetic stirring (1,000 rpm) with the entire apparatus being covered with aluminium foil. The solution was then further stirred in the dark for respectively 175, 170 and 90 min (in order for each experiment to have a final duration of 180 min). The total dye released was then calculated by filtering the microcapsules out of the solution using a syringe filter (PVDF, 0.45 μm), freeze-drying the remaining solution and obtaining a UV-Vis spectrum after redispersion of the product in 0.5 mL. The amount of dextran blue released was calculated by comparing to a calibration curve of the dye conjugated polymer.

## 4.3 Results and Discussion

### *4.3.1 Microparticle synthesis*

The microparticles were preapared as previously described[21]. Briefly, $CaCO_3$ cores (with a ζ-potential of + 4.6 mV at pH 6.5) were coated via a layer by layer (LbL) approach at pH 6.5 using PSS and PAH as the negatively and positively charged polyelectrolytes, respectively. In total 4 bilayers were added with subsequent dissolution of the cores with EDTA. For the preparation of UV light triggered microcapsules, the PSS in the 3rd bilayer was substituted for negatively charged $TiO_2$ nanoparticles) Such $TiO_2$ nanoparticles were obtained by coating the anatase particles with etidronic acid at a relatively low surface grafting density: 10 μmol etidronic acid per mg of $TiO_2$, corresponding to a ζ-potential of -42.3 mV. In the degradation of methylene blue etidronic acid-coated nanoparticles showed a comparable photoactivity to uncoated $TiO_2$ nanoparticles, respectively 3.24 $mmolL^{-1}min^{-1}$ vs. 1.03 $mmolL^{-1}min^{-1}$ (Figure 4.6-SI-1, 0.2 mg/mL nanoparticles, $8x10^{-3}$ mg/mL methylene blue, $\lambda = 250\text{-}450$ nm, 10 $mW/cm^2$). Therefore, it is assumed the etidronic acid coating did not significantly affect the photo-oxidative capacities of the nanoparticles.

Both nanoparticle-loaded and unloaded microparticles had a spherical shape with a diameter of 3-4.5 μm (Figure 4.3.1-1 A). It is hypothesised that here the ROS produced by the $TiO_2$ nanoparticles under UV illumination will irreversibly damage the polymer walls of the microparticles resulting in the release of any encapsulated species.

After illumination, it was evident that the morphology of the microparticles had changed dramatically with many of them collapsing and others breaking apart completely (Figure 4.3.1-1 B). A large amount of particles clusters was also formed in the illuminated solution, suggesting that oppositely charged patches are exposed during illumination, causing the capsules to aggregate. By illuminating microparticles without $TiO_2$ nanoparticles, no significant change in morphology was observed.

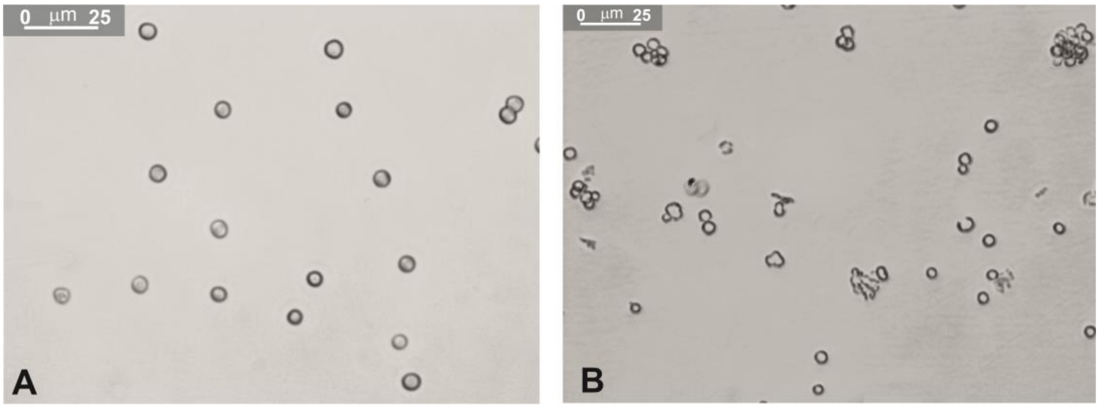

**Figure 4.3.1-1** *A)* Microscopy images of hollow core microspheres after preparation prior to any further treatment. This image is indicative of the entire sample. *B)* Microscopy images of hollow core microspheres after illumination showing that the walls of the microspheres have ruptured causing the microspheres to break apart and/or aggregate.

### *4.3.2 Loading and release of dye conjugated polymers*

One of the purposes of such hollow core microspheres is the encapsulation of active agents and their light-activated delivery in a cellular environment. After preparation the walls of the microspheres are porous with a mesh size of ~ 13 nm and it has been shown that subsequent heating to 65°C (above the glass transition temperature of the polymers) causes the polymer chains to rearrange and the capsules to shrink slightly. Upon rearrangement the mesh size of the pores in the polymer wall decreases to ~ 5 nm thus trapping any contained macromolecules inside the microcapsules (Scheme 4.3.2-1)[22].

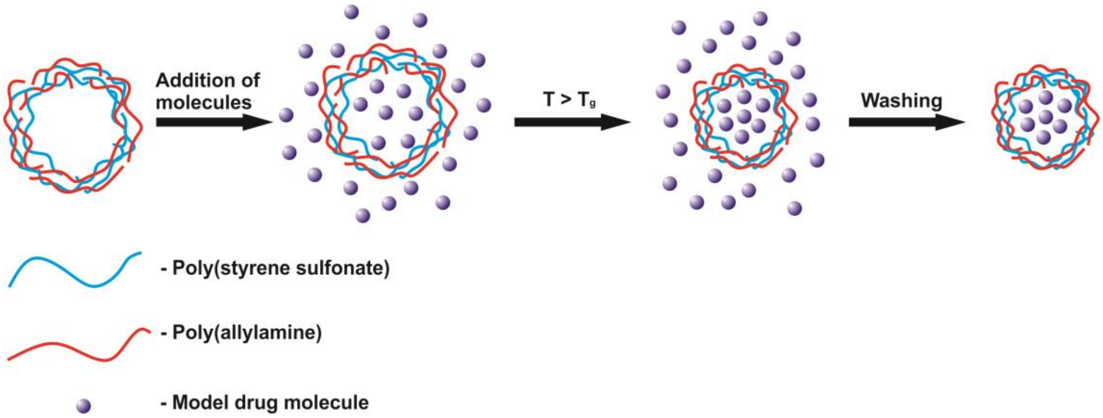

**Scheme 4.3.2-1** After preparation the PEM's are porous allowing small model molecules to penetrate the walls and localise in the hollow core. Upon heating the microcapsules shrink causing a decrease in pore size trapping any internalised molecules. The microcapsules are then washed removing any free molecules. Reproduced from ref. 22.

Previous studies performed by Köhler *et. al.* have shown that polymers with a molecular weight ~ 5-10 kDa are able to penetrate the initial capsule walls but do not leak from the capsules after heat treatment[22]. In this study we have conjugated Reactive Blue to dextran ($\overline{M_w}$ = 8 kDa) as a model polymer for studying the encapsulation and release characteristics of the microcapsules. After conjugation of dextran with Reactive Blue, and subsequent purification, the polymer showed a significant increase in absorbance at 590 nm (Figure 4.6-SI-2) with a molar extinction coefficient (ε) of 880 $\text{molL}^{-1}\text{cm}^{-1}$ (Figure 4.6-SI-3). Infrared spectroscopy clearly shows the appearance of bands at 1749 and 1570 $\text{cm}^{-1}$ (Figure 4.3.2-1) after conjugation of the polymer with reactive blue, which can be attributed to C=O stretching and triazine ring stretching respectively.

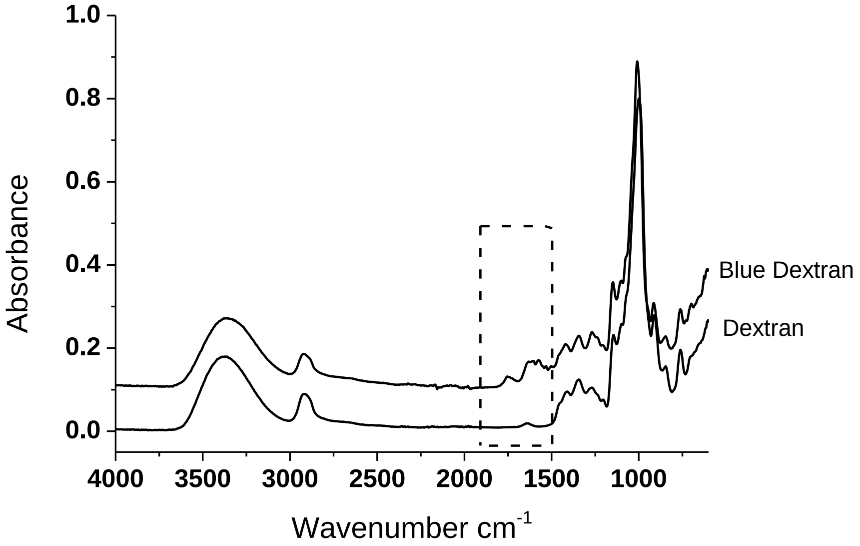

**Figure 4.3.2-1** IR spectra of dextran (*bottom*) and reactive blue conjugated dextran (*top*). The charactersitic peaks of dextran 3660-3035 (ν OH), 2927 ($\nu_{as}$ $CH_2$) and 1011 ($\nu_{as}$ C-O-C) $\text{cm}^{-1}$ are present in both spectra. Upon conjugation with reactive blue two main new peaks appear which are highlighted by the dashed box. These new peaks can be found at 1749 and 1570 $\text{cm}^{-1}$ and can be repsectively attributed to C=O stretching and triazine ring stretching frequencies given by the reactive blue.

Loading the microcapsules was achieved by dispersing them in a solution of the dye conjugated polymer for 30 minutes, allowing the diffusion of the polymer into the cores to reach equilibrium. Subsequently the microcapsule solution was heated for 2 hours and then the microcapsules were washed. After heating the microcapsules were centrifuged out of the solution and the UV-Vis spectrum of the supernatant was obtained. This allowed the calculation of the remaining polymer in solution (using its extinction coefficients) thus directly indicating the mass of polymer encapsulated. The encapsulation efficiency was calculated to be 83 % which is suspiciously high for a diffusion based process. Indeed, while dextran itself is neutral, Reactive Blue carries six negatively charged sulfonate groups, which enhance its solubility in water. It seems here that, even though there are a relatively low number of reactive blue molecules per polymer chain (< 1 mol%), the polymer may be adsorbing onto the positively charged layers of the microcapsule walls thus artificially increasing the amount of loaded polymer. On the other hand, the amount of releaseable polymer is probably considerably lower than that.

The loaded microcapsules were then redispersed in deionised water (5 mL) and stirred for 3 hours in the dark. Subsequently the microcapsules were centrifuged out of the solution and the supernatant was collected. Due to the low ε and broad absorbance of the polymer even relatively high concentrations were difficult to separate from noise using UV-Vis spectrophotometry, therefore, to increase the signal to noise ratio the supernatant was freeze dried and any polymer was redissolved in 500 μL of deionised water and observed through UV-Vis spectrophotometry. After 3 hours of stirring the microcapsules in the dark it was seen that there was a very low release of the dye contributing to around 0.36% of that encapsulated. It is difficult to say whether the polymer was actually released or whether it rather desorbed from the microcapsule wall. When the microcapsule solution was illuminated under UV light for 5, 10 and 90 minutes the amount of free polymer in the solution increased over time, ending at a total of around 1.65% of that encapsulated (see Figure 4.3.2-2). The release over time of the microcapsules, in terms of percentage, is not very high; however, this is due to the extremely high ee observed when loading the microcapsules. Figure 4 also shows the amount of polymer released in terms of concentration and these results are much more promising. The therapeutic level of many common drugs is on a ng/mL to μg/mL level, and already at 10 minutes of illumination the level of microcapsule release is already at 0.6 μg/mL and culminates in a concentration of 1.3 μg/mL after 90 minutes[23-25].

From this it is evident that under UV illumination there is an improved release of the encapsulated polymer due to the destructive effect of the ROS produced. However, most of the polymer loaded in/on the microcapsules was not released upon illumination. Since microscopy has shown that the capsule walls integrity was lost under illumination conditions (Figure 4.3.1-1), the limited release efficiency is most likely indicating that the polymer was not originally encapsulated in the capsules but rather adsorbed on the capsules walls. Similar conclusions were achieved by other groups using microcapsules and Carregal-Romero *et. al.* stated “it is difficult to quantify the amount of released cargo and most of the recent publications in this field are focusing on observing a cell response mediated by the cargo instead”[21]. A different model payload which does not adsorb on the capsule walls would need to be used for further release studies. A more sensitive method also needs to be found in which the release can be monitored over time, with the best option being using a fluorescent marker as fluorescence is much more sensitive than UV-Vis spectroscopy. Using a fluorescent marker is not without problems as they are typically highly vulnerable to photo-bleaching, therefore the choice of marker is crucial for the continuation of this study.

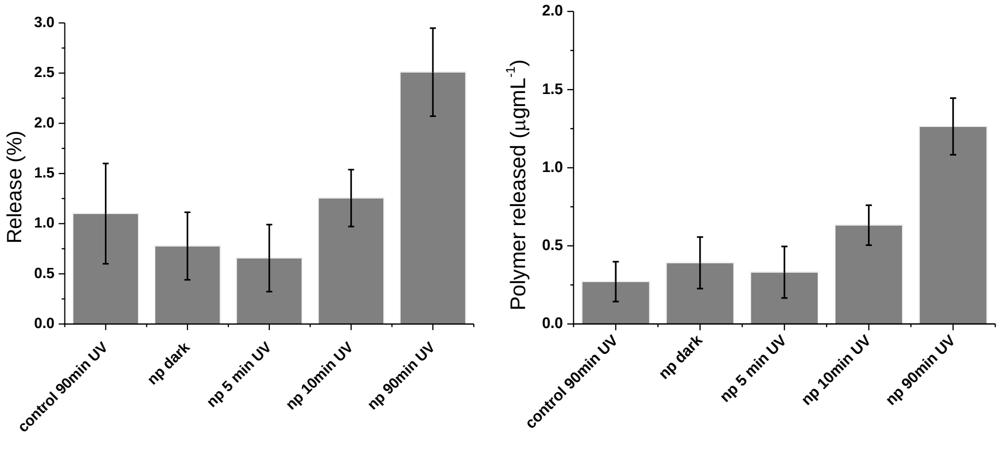

**Figure 4.3.2-2** (***left***) Percentage release of dye conjugated polymer by microcapsules under varying conditions. (***right***) Absolute mass of polymer released by microcapsules under varying conditions. Note : np = microcapsules with $TiO_2$ nanoparticles embedded in their walls, the control microcapsules have no $TiO_2$ layer.

## 4.4 Conclusion

In this study we have demonstrated the ability of creating UV triggered PEM microcapsules as drug delivery vehicles. After preparation the microcapsules could be loaded with model polymers which, after heat treatment, were trapped inside the capsules. By incorporating $TiO_2$ nanoparticles into the walls of the microcapsules the entrapped polymer could be released under UV illumination; this is achieved due to the ROS produced by the $TiO_2$ irreversibly damaging and rupturing the walls of the microcapsules.

As a preliminary study the results show promise for the development of a new breed of smart delivery vehicles. However, the charge present on the model polymer resulted in an “overloading” in the microcapsules, most likely due to the polymer adsorbing onto the microsphere shell as well as loading into the hollow core. The resulting release studies were therefore somewhat skewed in terms of percentage release. However, the total mass of polymer released under illumination resulted in local concentrations higher, or on par with, therapeutic concentrations of many commonly used drugs. To further this study a more sensitive method of analysing the release is needed, either by using fluorescent models or high performance liquid chromatography (HPLC) to screen the solutions after illumination.

## 4.5 References

1. Ma, D.; Hettiarachchi, G.; Nguyen, D.; Zhang, B.; Wittenberg, J. B.; Zavalij, P. Y.; Briken, V.; Isaacs, L., Acyclic cucurbit n uril molecular containers enhance the solubility and bioactivity of poorly soluble pharmaceuticals. *Nat. Chem.* **2012,** 4, (6), 503-510.

2. Pabla, N.; Dong, Z., Curtailing side effects in chemotherapy: a tale of PKC delta in cisplatin treatment. *Oncotarget* **2012,** 3, (1), 107-111.

3. Christie, R. J.; Grainger, D. W., Design strategies to improve soluble macromolecular delivery constructs. *Adv. Drug Deliv. Rev.* **2003,** 55, (3), 421-437.

4. Brannon-Peppas, L.; Blanchette, J. O., Nanoparticle and targeted systems for cancer therapy. *Adv. Drug Deliv. Rev.* **2004,** 56, (11), 1649-1659.

5. Na, K.; Lee, K. H.; Lee, D. H.; Bae, Y. H., Biodegradable thermo-sensitive nanoparticles from poly(L-lactic acid)/poly(ethylene glycol) alternating multi-block copolymer for potential anti-cancer drug carrier. *Eur. J. Pharm. Sci.* **2006,** 27, (2-3), 115-122.

6. Etrych, T.; Jelinkova, M.; Rihova, B.; Ulbrich, K., New HPMA copolymers containing doxorubicin bound via pH-sensitive linkage: synthesis and preliminary in vitro and in vivo biological properties. *J. Control. Release* **2001,** 73, (1), 89-102.

7. Eeckman, F.; Moes, A. J.; Amighi, K., Evaluation of a new controlled-drug delivery concept based on the use of thermoresponsive polymers. *Int. J. Pharm.* **2002,** 241, (1), 113-125.

8. Giri, S.; Trewyn, B. G.; Stellmaker, M. P.; Lin, V. S. Y., Stimuli-responsive controlled-release delivery system based on mesoporous silica nanorods capped with magnetic nanoparticles. *Angew. Chem.-Int. Edit.* **2005,** 44, (32), 5038-5044.

9. Sershen, S. R.; Westcott, S. L.; Halas, N. J.; West, J. L., Temperature-sensitive polymer-nanoshell composites for photothermally modulated drug delivery. *J. Biomed. Mater. Res.* **2000,** 51, (3), 293-298.

10. Mal, N. K.; Fujiwara, M.; Tanaka, Y., Photocontrolled reversible release of guest molecules from coumarin-modified mesoporous silica. *Nature* **2003,** 421, (6921), 350-353.

11. Skirtach, A. G.; Javier, A. M.; Kreft, O.; Kohler, K.; Alberola, A. P.; Mohwald, H.; Parak, W. J.; Sukhorukov, G. B., Laser-induced release of encapsulated materials inside living cells. *Angew. Chem.-Int. Edit.* **2006,** 45, (28), 4612-4617.

12. Mahalati, R. N.; Gu, R. Y.; Kahn, J. M., Resolution limits for imaging through multi-mode fiber. *Optics Express* **2013,** 21, (2), 1656-1668.

13. Helmchen, F.; Denk, W., Deep tissue two-photon microscopy. *Nat. Methods* **2005,** 2, (12), 932-940.

14. Qiu, X. P.; Leporatti, S.; Donath, E.; Mohwald, H., Studies on the drug release properties of polysaccharide multilayers encapsulated ibuprofen microparticles. *Langmuir* **2001,** 17, (17), 5375-5380.

15. Voigt, A.; Buske, N.; Sukhorukov, G. B.; Antipov, A. A.; Leporatti, S.; Lichtenfeld, H.; Baumler, H.; Donath, E.; Mohwald, H., Novel polyelectrolyte multilayer micro- and nanocapsules as magnetic carriers. *J. Magn. Magn. Mater.* **2001,** 225, (1-2), 59-66.

16. Zhu, C. L.; Song, X. Y.; Zhou, W. H.; Yang, H. H.; Wen, Y. H.; Wang, X. R., An efficient cell-targeting and intracellular controlled-release drug delivery

system based on MSN-PEM-aptamer conjugates. *J. Mater. Chem.* **2009,** 19, (41), 7765-7770.

17. Albanese, A.; Tang, P. S.; Chan, W. C. W., The Effect of Nanoparticle Size, Shape, and Surface Chemistry on Biological Systems. *Annu. Rev. Biomed. Eng, Vol 14*, Yarmush, M. L.; Duncan, J. S.; Gray, M. L., Eds. Annual Reviews: Palo Alto, 2012; Vol. 14, pp 1-16.

18. Zhou, J.; Romero, G.; Rojas, E.; Ma, L.; Moya, S.; Gao, C. Y., Layer by layer chitosan/alginate coatings on poly(lactide-co-glycolide) nanoparticles for antifouling protection and Folic acid binding to achieve selective cell targeting. *J. Colloid Interface Sci.* **2010,** 345, (2), 241-247.

19. Cui, J. W.; Fan, D. W.; Hao, J. C., Magnetic {Mo72Fe30}-embedded hybrid nanocapsules. *J. Colloid Interface Sci.* **2009,** 330, (2), 488-492.

20. Shutava, T. G.; Pattekari, P. P.; Arapov, K. A.; Torchilin, V. P.; Lvov, Y. M., Architectural layer-by-layer assembly of drug nanocapsules with PEGylated polyelectrolytes. *Soft Matter* **2012,** 8, (36), 9418-9427.

21. Carregal-Romero, S.; Ochs, M.; Rivera-Gil, P.; Ganas, C.; Pavlov, A. M.; Sukhorukov, G. B.; Parak, W. J., NIR-light triggered delivery of macromolecules into the cytosol. *J. Control. Release* **2012,** 159, (1), 120-127.

22. Kohler, K.; Sukhorukov, G. B., Heat treatment of polyelectrolyte multilayer capsules: A versatile method for encapsulation. *Adv. Funct. Mater.* **2007,** 17, (13), 2053-2061.

23. Takahashi, N.; Miura, M., Therapeutic Drug Monitoring of Imatinib for Chronic Myeloid Leukemia Patients in the Chronic Phase. *Pharmacology* **2011,** 87, (5-6), 241-248.

24. de Jonge, M. E.; Huitema, A. D. R.; Schellens, J. H. M.; Rodenhuis, S.; Beijnen, J. H., Individualised cancer chemotherapy: Strategies and performance of prospective studies on therapeutic drug monitoring with dose adaptation - A review. *Clin. Pharmacokinet.* **2005,** 44, (2), 147-173.

25. Carter, N. J.; Keam, S. J., Trabectedin- A review of its use in the management of soft tissue sarcoma and ovarian cancer. *Drugs* **2007,** 67, (15), 2257-2276.

## 4.6 Supplementary Information

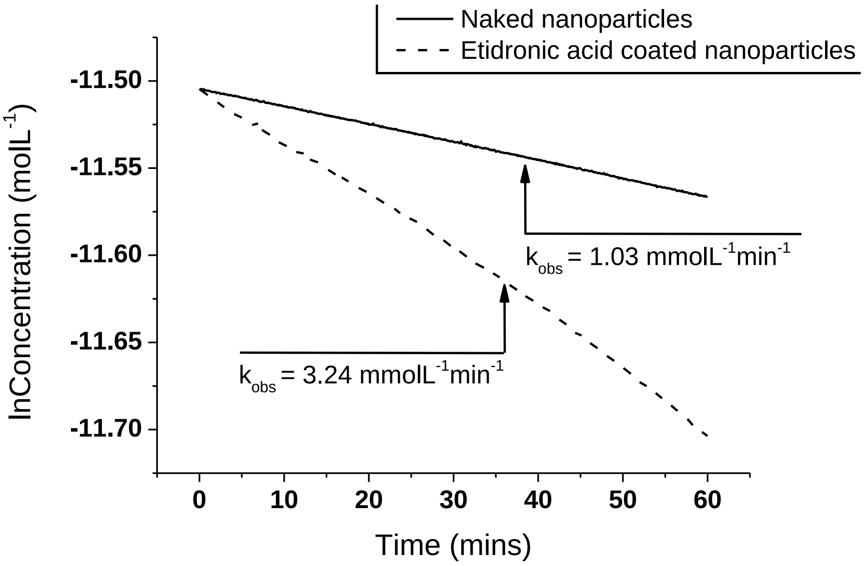

**Figure 4.6-SI-1** The photodegradation reaction of methylene blue by $TiO_2$ nanoparticles follows pseudo first order kinetics. The rate is determined from the slope of the ln of the concentration vs. the time of reaction according to $\ln C = -k_{obs}t + \ln C_o$ where C is the concentration of remaining methylene blue, t is time and $C_o$ is the initial concentration of methylene blue.

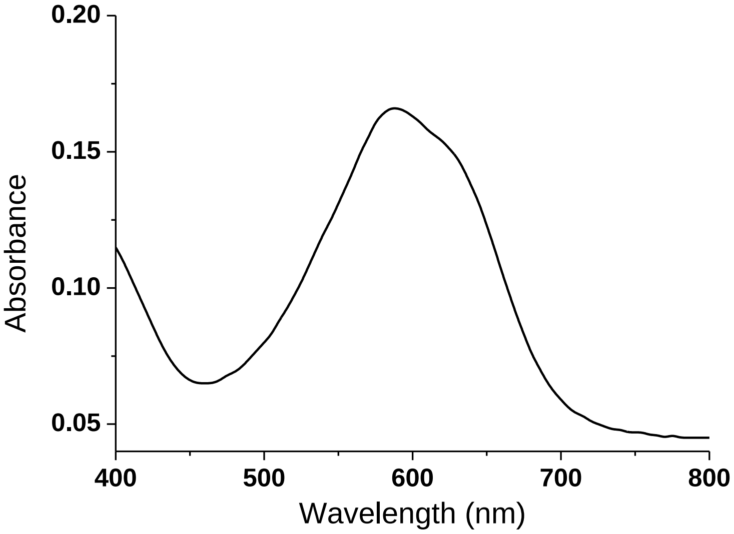

**Figure 4.6-SI-2** UV-Vis spectrum of reactive blue conjugated to dextran.

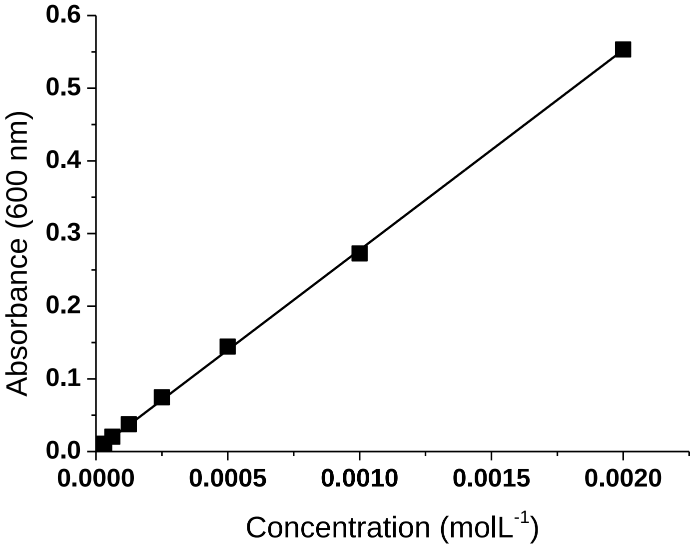

**Figure 4.6-SI-3** Calibration curve of reactive blue conjugated dextran with ε = 880 molL$^{-1}$cm$^{-1}$

# 5 Conclusions and outlook

During the last few decades a lot of research has been directed towards the use of titanium dioxide ($TiO_2$) in a wide variety of applications, from dye-sensitized solar cells to water purification. Recently there has been a great deal of interest in using $TiO_2$, specifically in a nanoparticulate form, for biomedical applications. As well as being photoactive, $TiO_2$ is highly biocompatible, under dark conditions, therefore a lot of research is based on the use of $TiO_2$ nanoparticles as transport agents for drugs or MRI contrast agents etc. However, there is growing interest in using the photoactive capability of $TiO_2$ for *in vivo* applications. The interest lies with the fact that with the nanoparticles being relatively non-toxic they are free to distribute throughout the body without causing any adverse effects. However, upon illumination with near UV light they are able to produce reactive oxygen species (ROS). These ROS have the capability to diffuse away from the nanoparticles and induce apoptosis and death in neighbouring cells, this treatment is commonly known as photodynamic therapy (PDT) and it allows the possibility of targeting diseased areas of the body, such as tumours, whilst leaving healthy tissue unharmed. There are a number of advantages for using $TiO_2$ for PDT rather than the currently used porphyrin derivatives:

1) The synthetic methods for the production of $TiO_2$ are highly reproducible allowing fine control over the resulting size and characteristics of the nanoparticles. As the photoactivity of $TiO_2$ is directly linked to the number of surface sites there should therefore be a dramatic increase in photoactive capability in the nano regime.
2) It is relatively easy to modify the surface of $TiO_2$ allowing the possibility to label the nanoparticles with antibodies or markers in order to target specific cells *in vivo*.
3) The production costs of nanoparticulate $TiO_2$ are extremely low. In recent years $TiO_2$ costs have risen by more than 70% and now costs over \$3.70 per kilo[1]. However, despite this increase the price remains rather low and the benefits of using $TiO_2$ for PDT compared to more labour intensive organic molecules are still high.

**Chapter 2** presented the results into the controlled synthesis of $TiO_2$ nanoparticles through a water mediated sol-gel synthetic method. In brief the synthesis involved the addition of either $Ti(O\textit{n}Pr)_4$, $Ti(O\textit{n}Bu)_4$ or $Ti(O^iPr)_4$ into benzyl alcohol which contained molar equivalents of water. It was seen that primary nanoparticles, ~ 3nm in diameter, were formed instantly upon adding the metal alkoxide precursor to the reaction medium. Typically it is believed that in a sol-gel reaction nanoparticles are formed by the atom wise addition of metal precursors onto the surface of a growing nanoparticle. However, here we have shown that the nanoparticles grow through the agglomeration of the primary nanoparticles formed at the beginning of the synthesis.

After synthesis the nanoparticles had the ability to be redispersed in an aqueous solution, at pH2, after precipitation out of benzyl alcohol by the addition of diethyl ether. The resulting size of the nanoparticles after redispersion depended on the nature of the parent alkoxide used for the reaction. Nanoparticles synthesized from $Ti(O^iPr)_4$ showed no apparent increase in size upon redispersion in an aqueous solution. The decrease in aggregation upon redispersion, compared to the butoxide and propoxide derivatives which showed mild, but significant, amounts of agglomeration, can be attributed to isopropoxide being the most hydrophobic alkoxide of the three used. The agglomeration of the nanoparticles upon redispersion appeared to depend on the rate of hydrolysis of any alkoxides present on the surface of the nanoparticles. As the rate of hydrolysis of the isopropoxide was the slowest this resulted in a very low, practically indistinguishable, amount of post synthesis agglomeration to occur.

After synthesis it was necessary to keep the nanoparticles in an aqueous solution at acidic pH, this protonated the surface of the nanoparticles and, through electrostatic repulsion, stabilized them against any further agglomeration. However, in order to use the nanoparticles *in vivo* it was necessary to coat them with suitable ligands in order to allow their dispersion at neutral pH without significant change in dimensions. **Chapter 3** discusses the ability of grafting PEG, which was pre-conjugated to either catechols (mPEG-DA) or phosphates (mPEG-PEA) as ligands, to the surface of the nanoparticles.

It was seen that the amount of polymer present on the surface of the nanoparticles was vital to their stability at neutral pH. For both species of PEG at least 1 μmol of ligand per mg of $TiO_2$ was needed to stabilize the nanoparticles at neutral pH. Stability was afforded to the nanoparticles through steric interference between the PEG chains, which obstructed the surface of the nanoparticles from coming into contact with one another. A second advantage of using PEG to coat the nanoparticles was to provide them with a "stealth" character. The "stealth" character and biocompatibility of mPEG-DA coated nanoparticles was shown in this chapter and currently similar studies are being undertaken with mPEG-PEA coated nanoparticles. Along with observing their biocompatibility, studies are currently being conducted into the cytotoxic profile of the mPEG-PEA coated nanoparticles under UV illumination.

The second part of this chapter assessed the photoactivity of coated nanoparticles in relation to their naked counterparts. In essence, as the photoactivity of the nanoparticles is related to the number of surface sites, the aim was to produce coated nanoparticles which were stable at neutral pH but that still had enough free surface sites to exhibit a high photoactive capability. The photoactivity of the nanoparticles was studied through the degradation of an oxidation responsive dye, methylene blue, in solution. It was seen that at pH 2 the naked nanoparticles were showed a reasonable photoactive behaviour, however, upon coating the nanoparticles with the minimum amount of mPEG-DA to provide stability, all photo-oxidative capability of the nanoparticles was lost. Indeed, regardless of the catechol species they all killed the photoactivity of the nanoparticles upon adsorption. Through comparing our results with those in the literature it was concluded coating the surface of $TiO_2$ with aromatic moieties prevented the migration of photogenerated holes and electrons to the surface of the metal oxide to produce ROS. Instead the positive holes localized in the electron rich catechol centre whereas the free electron was trapped on a single Ti(IV) centre eventually converting it to Ti(III).

However, when using phosph(on)ate ligands the photoactivity of the nanoparticles is preserved, or even enhanced, in some cases. The enhancement in photoactivity seems to be dependent on two factors:

1) The surface charge of the nanoparticles, where those with higher ζ potentials repel the cationic dye thus decreasing the likelihood of the dye coming into contact with the photogenerated ROS.
2) Upon surface modification the cocktail of ROS produced is changed. Naked nanoparticles mainly produce superoxide upon irradiation as the addition of benzoquinone as a quencher drastically reduces the degradation rate. Superoxide seems to also play a substantial role in methylene blue degradation using PEA PEGylated nanoparticles, however with other quenchers such as sodium azide, which quenches singlet oxygen, seeming to decrease the degradation rate this points to a larger variety of ROS being produced upon surface modification.

The majority of near future work will be continued from this chapter into furthering our understanding into the photoactivity of coated nanoparticles. As mentioned the first step is to conduct cytotoxicity experiments of mPEG-PEA coated nanoparticles on macrophages both under dark and illuminated conditions. The photoactivity of coated nanoparticles in solution with a negatively charged dye, such as indigo carmine, will also be undertaken to further explain the apparent increase in photoactivity of the nanoparticles when coated with phosph(on)ates.

Finally, the original aim to coat nanoparticles with catechols was to shift the $\lambda_{max}$ of the system into the visible region thus increasing the penetration depth of light through tissue. Another way to accomplish this would be to dope the nanoparticles with inorganic or organic elements. There have been a number of studies reporting the activation of $TiO_2$ with visible light when doped with carbon[2], sulfur[3], platinum[4] etc. However it is apparent from the literature that doping with nitrogen shifts the activation wavelength of $TiO_2$ the most up to 550 nm[5] therefore perhaps for this project synthesizing $TiO_2$ nanoparticles doped with nitrogen would be an interesting strategy to adopt in order to improve the efficacy of the nanoparticles *in vivo*.

**Chapter 4** reports the findings into a preliminary study where $TiO_2$ nanoparticles were incorporated into the walls of polyelectrolyte multilayer microcapsules. The microcapsules were created by the layer by layer (LbL) addition of alternating poly(styrene sulfonate) (PSS) and poly(allyl amine) layers around a $CaCO_3$ core.

One of the PSS layers was substituted for etidronic acid coated $TiO_2$ nanoparticles, an etidronic acid coating was chosen as it provided the nanoparticles with a highly negative ζ-potential whilst preserving their photoactivity. After preparation of the microcapsules, the $CaCO_3$ core was dissolved out *via* complexation with ethylenediaminetetraacetic acid (EDTA).

The resulting hollow core was then post loaded with dextran blue as a model in order to study the release of the polymer from the microcapsules under near UV illumination. It was theorised that under illumination the ROS created by the $TiO_2$ would rupture the walls of the microparticles causing the encapsulated polymer to be released. Microscopy images showed that after synthesis the microparticles where spherical with an average size of 3-4.5 μm. After illumination the morphology of the microparticles changed dramatically with many of them clearly collapsing or breaking apart. Also when compared to the control there was a substantial release of the polymer observed, however due to a large amount of polymer adsorbing on the polymer wall of the microspheres through electrostatic interactions, the percentage of the polymer “released” compared to that adsorbed/encapsulated was extremely low.

Studies are currently on going into studying the release of encapsulated macromolecules by HPLC. However, instead of post loading the microparticles they are loaded by coprecipitating the model macromolecule (which in this case is bovine serum albumin) with the $CaCO_3$ core prior to the LbL step. This way we make sure that no model compound is adsorbed onto the polymer wall and that any release observed comes from the hollow core alone.

## 5.1 References

1. Smith, A., Reducing the cost of white opacity optimized use of titanium dioxide. *JCT Coatingstech* **2012,** *9* (3), 52-53.

2. Sakthivel, S.; Kisch, H., Daylight photocatalysis by carbon-modified titanium dioxide. *Angew. Chem.-Int. Edit.* **2003,** *42* (40), 4908-4911.

3. Umebayashi, T.; Yamaki, T.; Itoh, H.; Asai, K., Band gap narrowing of titanium dioxide by sulfur doping. *Appl. Phys. Lett.* **2002,** *81* (3), 454-456.

4. Choi, J.; Park, H.; Hoffmann, M. R., Effects of single metal-ion doping on the visible-light photoreactivity of $TiO_2$. *J. Phys. Chem. C* **2010,** *114* (2), 783-792.

5. Ihara, T.; Miyoshi, M.; Iriyama, Y.; Matsumoto, O.; Sugihara, S., Visible-light-active titanium oxide photocatalyst realized by an oxygen-deficient structure and by nitrogen doping. *Appl. Catal. B-Environ.* **2003,** *42* (4), 403-409.